LUND UNIVERSITY

Modelling the development of phyllotactic patterns at the shoot apical meristem of Arabidopsis thaliana

Sahlin, Patrik

2010

Link to publication

Citation for published version (APA):
Sahlin, P. (2010). *Modelling the development of phyllotactic patterns at the shoot apical meristem of Arabidopsis thaliana*. [Doctoral Thesis (compilation), Computational Biology and Biological Physics - Has been reorganised].

Total number of authors:
1

General rights
Unless other specific re-use rights are stated the following general rights apply:
Copyright and moral rights for the publications made accessible in the public portal are retained by the authors and/or other copyright owners and it is a condition of accessing publications that users recognise and abide by the legal requirements associated with these rights.
• Users may download and print one copy of any publication from the public portal for the purpose of private study or research.
• You may not further distribute the material or use it for any profit-making activity or commercial gain
• You may freely distribute the URL identifying the publication in the public portal

Read more about Creative commons licenses: https://creativecommons.org/licenses/

Take down policy
If you believe that this document breaches copyright please contact us providing details, and we will remove access to the work immediately and investigate your claim.

LUND UNIVERSITY

PO Box 117
221 00 Lund
+46 46-222 00 00

Modelling the development of phyllotactic patterns at the shoot apical meristem of *Arabidopsis thaliana*

Patrik Sahlin

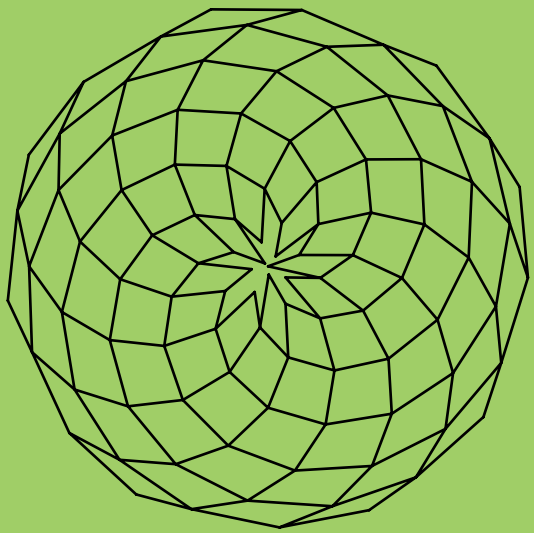

Computational Biology & Biological Physics
Department of Astronomy and Theoretical Physics
Lund University, Sweden

Patrik Sahlin

Modelling the development of phyllotactic patterns at the shoot apical meristem of *Arabidopsis thaliana*

ISBN: 978-91-628-8063-7

Modelling the development of phyllotactic patterns at the shoot apical meristem of *Arabidopsis thaliana*

Patrik Sahlin

Lund University

Computational Biology & Biological Physics
Department of Astronomy and Theoretical Physics
Lund University, Sweden

Thesis for the degree of Doctor of Philosophy

Advisor: Henrik Jönsson

Faculty opponent: Nick Monk
University of Nottingham, UK

To be presented, with the permission of the Faculty of Science of Lund University, for public criticism in Lundmarksalen in the astronomy building, the 30th of April 2010, at 10.15 a.m.

Organization	Document name
LUND UNIVERSITY Department of Astronomy and Theoretical Physics Sölvegatan 14A SE–223 62 LUND Sweden	DOCTORAL DISSERTATION
	Date of issue April 2010
	Sponsoring organization
Author(s) Patrik Sahlin	

Title and subtitle

Modelling the development of phyllotactic patterns at the shoot apical meristem of *Arabidopsis thaliana*

Abstract

The study of phyllotactic patterns have a long history, but the bulk of our detailed understanding of developmental processes in plants comes from research conducted in the last thirty or forty years. New modern techniques have made it possible to study plants in ways that previously was not possible. Using confocal microscopy it is possible to generate three-dimensional stacks of images of a plant, and series of stacks makes it possible to follow the development in time. In combination with biological markers, gene and protein expression patterns can be followed both in time and space. This new type of data plays an important role in the modern development of mathematical and computational models of developmental processes in plants.

In this thesis we study different aspects of the development of phyllotactic patterns at the shoot apical meristem of *Arabidopsis thaliana*; the self-regulating feedback network of the *WUSCHEL* and *CLAVATA* genes, anisotropic growth of plant cells, cell division in the epidermal layer of the meristem, and intercellular transport of the plant hormone auxin. A systems biology approach is taken to make models from experimental data. All models are represented mathematically by ordinary differential equations and a toolbox of both analytical, numerical, and statistical methods is used to analyse the models. Using computer simulations and the subsequent data analysis we provide predictions that can be tested in experiments.

Key words:

phyllotaxis, *Arabidopsis*, shoot apical meristem, plant stem cells, cell division, systems biology

Classification system and/or index terms (if any):

Supplementary bibliographical information:		Language English
ISSN and key title:		ISBN ISBN 978-91-628-8063-7
Recipient's notes	Number of pages 112	Price
	Security classification	

Distributor

Patrik Sahlin, Department of Astronomy and Theoretical Physics, Sölvegatan 14A, SE–223 62 Lund, Sweden

I, the undersigned, being the copyright owner of the abstract of the above-mentioned dissertation, hereby grant to all reference sources the permission to publish and disseminate the abstract of the above-mentioned dissertation.

Signature Paul Sahlin Date 2010-03-18

DOKUMENTDATABLAD enl SIS 61 41 21

Summary in Swedish

Fyllotaxi är läran om blad, löv, och andra växtorgans placering. Ordet fyllotaxi har sitt ursprung i de grekiska orden för 'blad' och 'organisation', och mönsterbildning i växter har studerats sedan antiken. Mönster i naturen har alltid intresserat människan och fantasieggande kopplingar till matematiken gör sig ständigt till känna. I många växter bildar växtorgan mönster av spiraler som är nära sammankopplade med den så kallade Fibonacci-serien. Fibonacci-serien är en serie av heltal där varje tal i serien är summan av de två föregående talen (1, 1, 2, 3, 5, 8, 13, 21, o.s.v.). Kvoten mellan två efterföljande tal i serien går mot vad som brukar kallas för det gyllene snittet. När ett nytt växtorgan skapas bildar det tillsammans med det föregående organet en vinkel. Vinkeln är ofta lika med 137,5° – kallad den gyllene vinkeln – vilken är nära besläktad med det gyllene snittet. När växten skapar nya organ skapas en spiral, men det mänskliga ögat uppfattar även att organen bildar ett antal spiraler i både mot- och medurs riktning. Räknar man antalet spiraler i vardera riktning är dessa två tal – för många växter – lika med två efterföljande tal i Fibonacci-serien.

Trots att människan har studerat mönsterbildning i växter i flera tusen år kommer den större delen av vår förståelse för de underliggande biologiska processerna från forskning utförd under de senaste tre-fyra decennierna. Ny teknik har skapat möjligheter att undersöka utvecklingen från frö till fullvuxen växt. Konfokalmikroskopi har gjort det möjligt att skapa tredimensionella modeller av växter som kan studeras och användas vid modellering och datorsimuleringar. Med hjälp av biologiska markörer är det även möjligt att följa geners och proteiners uttryck i tid och rum.

I den här avhandlingen använder vi modeller för att studera olika aspekter av mönsterbildning i skottet av växten *Arabidopsis thaliana* – eller backtrav som är växtens svenska namn. I de fem artiklar som ingår i avhandlingen tittar vi närmare på ett självreglerande gennätverk i skottet, anisotropisk tillväxt av celler, celldelning, samt intercellulär transport av växthormonet auxin. I nära samarbete med biologer utvecklar vi matematiska modeller som uttrycks i form av ordinära differentialekvationer. Vi använder sedan analytiska, numeriska, och statistiska metoder för att analysera modellerna. Analyserna leder till förutsägelser som kan testas i nya experiment.

I avhandlingen står *Arabidopsis thaliana* i fokus. *Arabidopsis* är på grund av sin korta livscykel och modesta storlek en av de mest studerade modelorganismerna. Även vi väljer att studera *Arabidopsis*, men resultaten som presenteras i den här avhandlingen är även applicerbara på andra växter. Än är våra studier begränsade till grundforskning, men förhoppningar finns att forskningen ska leda till praktiska tillämpningar inom jordbruket och – den för Sverige viktiga – skogsindustrin.

This thesis is based on the following papers:

I **Patrik Sahlin**, Pontus Melke, and Henrik Jönsson. *Models of sequestration and receptor cross-talk for explaining multiple mutants in plant stem cell regulation.* LU-TP 10-02 (submitted). (2010).

II Olivier Hamant, Marcus G. Heisler, Henrik Jönsson, Pawel Krupinski, Magalie Uyttewaal, Plamen Bokov, Francis Corson, **Patrik Sahlin**, Arezki Boudaoud, Elliot M. Meyerowitz, Yves Couder, and Jan Traas. *Developmental Patterning by Mechanical Signals in Arabidopsis.* Science 322: 1650–1655. (2008).

III **Patrik Sahlin**, Olivier Hamant, and Henrik Jönsson. *Statistical Properties of Cell Topology and Geometry in a Tissue-Growth Model.* Complex Sciences 971–979. (2009).

IV **Patrik Sahlin** and Henrik Jönsson. *A modeling study on how cell division affects properties of epithelial tissues.* LU-TP 10-05 (submitted). (2010)

V **Patrik Sahlin**, Bo Söderberg, and Henrik Jönsson. *Regulated transport as a mechanism for pattern generation: Capabilities for phyllotaxis and beyond*. Journal of Theoretical Biology 258: 60–70. (2009).

I have also contributed to the following papers:

Pontus Melke, **Patrik Sahlin**, Andre Levchenko, and Henrik Jönsson. *A cell-based model for quorum sensing in heterogeneous colonies.* LU-TP 10-01 (submitted). (2010).

Bruce E. Shapiro, Henrik Jönsson, **Patrik Sahlin**, Marcus G. Heisler, Adrienne Roeder, Michael C. Burl, Elliot M. Meyerowitz, and Eric D. Mjolsness. *Tessellations and Pattern Formation in Plant Growth and Development.* To appear in *Tessellations in the Sciences; Virtues, Techniques and Applications of Geometric Tilings*, Springer Verlag. (2010).

Pawel Krupinski, Michael Green, Pontus Melke, **Patrik Sahlin**, and Henrik Jönsson. *Costanza: a segmentation and analyzing tool for three-dimensional microscopy data.* LU-TP 08-09.

Contents

Introduction **1**
The shoot apical meristem 2
Plant cells 6
Auxin and intercellular transport 8

Methodology **11**
Modelling chemical reactions 11
Modelling mechanics: The spring model 13
Analytical methods 14
Numerical methods 16

Summary of publications **21**

Acknowledgement **25**

Bibliography **26**

Introduction

The study of patterns in plants is a fascinating field as series, patterns, and relations known from physics and mathematics are found in plants. Therefore the field has attracted – and still attracts – researchers from various disciplines including, but not limited to plant biology. The study of patterns in plants has a long history and dates back to classical antiquity. Still, a bulk of the understanding about the development of patterns in plants comes from scientific work done in the last thirty or forty years, where modern experimental techniques have made it possible to study the development of plants in new ways. Confocal microscopy can generate three-dimensional stacks of images of plants and series of stacks make it possible to follow the development in time. In combination with biological markers it is now also possible to track gene and protein expression patterns during development.

This thesis is part of a field that is often referred to as systems biology. Systems biology is an interdisciplinary field with focus on complex dynamics in biological systems. With a systems approach low-level details are of less interest, instead effort is made to understand system-wide dynamics of interactions between different parts of the system. A complete list of all genes present in the genome of a plant – even together with the knowledge of all interactions between genes – is not sufficient for a full understanding of the development from a seedling to an adult plant. With a systems approach experiments are used to identify key components of the system and the interactions between them. This information is used to build models, which are capable of making predictions that can be tested in experiments. This thesis includes several examples of this process.

The thale cress *Arabidopsis thaliana* is the *Drosophila melanogaster* or *Escherichia coli* of plant biology and was the first plant species to have its full genome sequenced. The adult plant is about 20-25 cm tall and can complete its life cycle in six weeks. These properties make this plant a suitable model organism although there is little agricultural use for the plant itself. The focus of this thesis is the spiral patterns of *Arabidopsis thaliana* that are initiated at the shoot apical meristem. Still, the discussion is not limited to the study of the patterns of *Arabidopsis*. What is presented in this thesis is most likely to be true for other plants and the tools used are generally useful for studying other biological or non-biological systems.

Plant phyllotaxis and the Fibonacci series. Plant phyllotaxis is the arrangement of leaves, flowers, and other plant organs. The most famous type of phyllotactic patterns is Fibonacci phyllotaxis. In the Fibonacci series each element is the sum of the two previous elements (1, 1, 2, 3, 5, 8, 13, 21, and so on). The ratio between two consecutive elements converges and the limit is called the golden ratio. New plant organs are initiated at the tip of the plant shoot and are initiated with a fairly constant angle between consecutive organs. What is interesting is that this angle is in many cases close to the golden angle, closely related to the golden ratio.

As new organs are initiated a spiral known as the genetic spiral is created. Although consecutively initiated organs are located rather far away from each other, every organ is located close to two organs above and two organs below itself. The human eye tends to follow these neighbouring organs in spirals going clockwise and anti-clockwise around the stem. These spirals are called *parastichies*. If the number of clockwise and anti-clockwise parastichies are counted then these numbers are for many plants two consecutive elements in the Fibonacci series. See Figure 1 for a computer-generated example of Fibonacci phyllotaxis.

A fundamental question is what gives rise to Fibonacci phyllotaxis in plants. It has been shown that the combination of a growing apex and a spacing mechanism for new primordia is sufficient for Fibonacci phyllotaxis (Mitchison 1977). Douady and Couder illustrated this with an elegant experiment (Douady and Couder 1992). Charged oil-drops were placed in a magnetic field on a horizontal dish. The magnetic field made the oil-drops move radially outwards, which would correspond to a growing apex in a plant. The oil-drops also repelled each other, corresponding to a spacing mechanism of new plant organs. By tuning the strength of the magnetic field and the periodicity of adding new oil-drops Douady and Couder were able to produce patterns equivalent to Fibonacci phyllotaxis.

Motivation. As stated above, two "ingredients" – a growing apex and a spacing mechanism for new primordia – have been identified and in combination they result in proper phyllotactic patterns. The five papers of this thesis all study different aspects of these two ingredients. Paper I is about stem cells, which are tied to both tissue growth and initiation of new primordia. Paper II, Paper III, and Paper IV are all studies of the growth of the epidermal layer of the shoot apical meristem. Paper V is mainly related to a mechanism for initiating new primordia, but the results also have implications for the growth of the tissue. See Figure 2 for a diagram showing how the different projects are related to phyllotactic patterns.

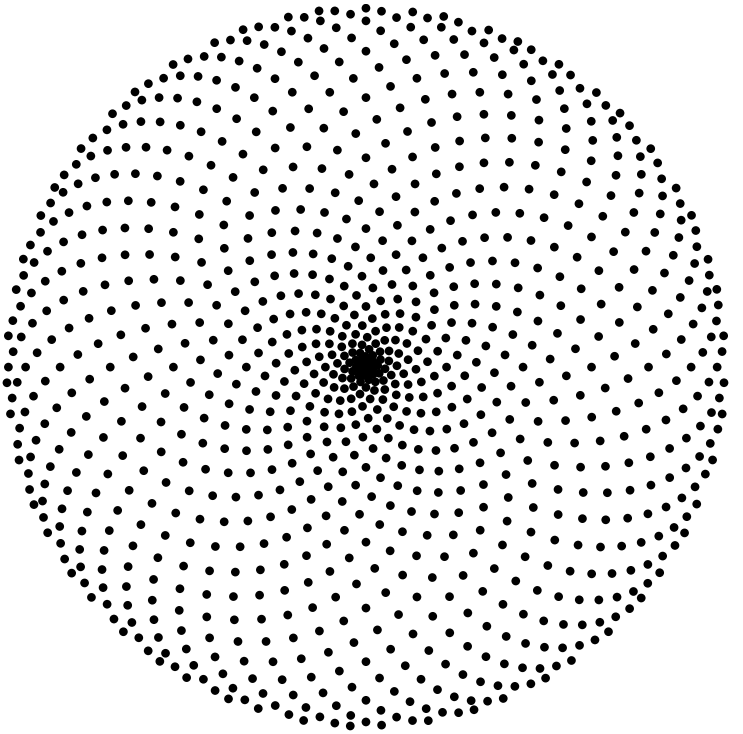

Figure 1: Computer-generated example of Fibonacci phyllotaxis. There are 34 clockwise and 55 anti-clockwise spirals in the pattern. These two numbers are consecutive elements in the Fibonacci series.

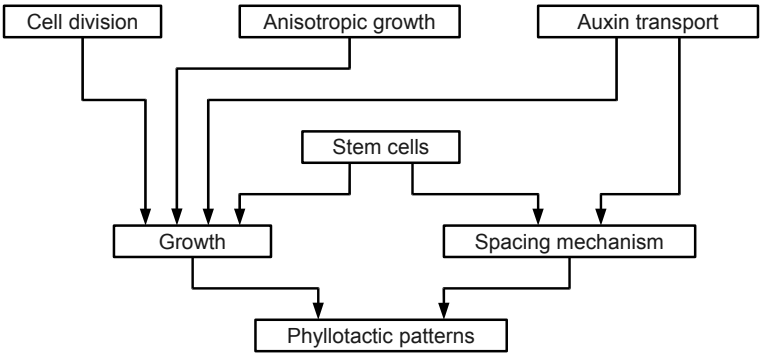

Figure 2: Diagram showing how the projects presented in this thesis are related to phyllotactic patterns in *Arabidopsis thaliana*.

The shoot apical meristem

Arabidopsis thaliana has two primary meristems; the primary shoot apical meristem, which is the source of all above-ground tissue and organs, and the primary root meristem, which is the source of the below-ground root system. In addition there are secondary meristems originating from the primary meristems; lateral root meristems from the primary root meristem, and shoot and floral meristems from the primary shoot meristem (Weigel and Jürgens 2002).

Meristems and plant stem cells. The main function of the meristems is to harbour stem cells. Most cells proliferate to produce new cells of the same cell type, but stem cells also have the ability to differentiate into more specialised cell types. Stem cells that can differentiate into multiple different cell types are *pluripotent* and cells that can differentiate into all different cell types are *totipotent*. While animal stem cells are mostly pluripotent many plant cells stay totipotent.

The shoot apical meristem can be divided into several regions of different functions, see Figure 3. The central zone is located at the tip of the meristem where stem cells reside. The stem cells at the central zone are slowly dividing and their descendants are displaced to the peripheral zone. The peripheral zone is the area adjacent to and surrounding the central zone. Cells at the peripheral zone divide at higher rates and differentiate to specialised cell types. The rib meristem is located underneath the central zone and cells in this region also divide at higher rates. Lateral organs are initiated at the peripheral zone and cell fate is mainly decided by a cell's spatial location (Bowman and Eshed 2000; Weigel and Jürgens 2002).

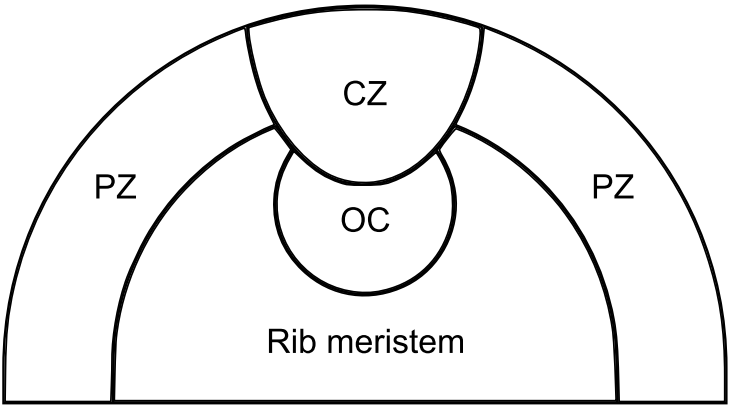

Figure 3: Schematic drawing of the organisation of the shoot apical meristem. Central zone (CZ), peripheral zone (PZ), organisation centre (OC), and rib meristem.

The cells of the shoot meristem are organised into three clonally distinct layers. The outermost epidermal layer, L1, is the source for the epidermis. Underneath the epidermal layer is the subepidermal layer L2 and the corpus, or L3, the latter also includes the remaining internal cells. The L2 and L3 are the sources of internal subepidermal tissue. This structure of clonally distinct layers are preserved in lateral organs and thus organ formation requires cooperation between all three layers (Meyerowitz 1997).

Humans can live for about a hundred years, and the oldest known animal was about 400 years old, but some plants can have lifetimes of several thousands years. Although cells divide and move in and out between the different zones the structure of the meristem is maintained during the lifetime of the plant. An extra cell division at the meristem every year would after only ten years result in a meristem a thousand times larger than a normal meristem. For a plant that is expected to live for hundreds or even thousands of years the need for a well-balanced meristem is crucial. The stability of the meristem during growth suggests an underlying feedback network that balances the proliferation and differentiation of cells of the meristem.

The *WUSCHEL* and CLAVATA genes. The *WUSCHEL* (*WUS*) and the CLAVATA (CLV) genes are present in the *Arabidopsis* genome and have been shown to be essential for the self-maintenance of the shoot apical meristem. The *CLV3* gene is expressed in the cells in the central zone and is often used as a stem cell identity marker (Fletcher et al. 1999). *WUS* is in postembryonic development expressed in a small group of cells referred to as the organising centre and located under the central zone (Mayer et al. 1998). *WUS* expression is necessary and sufficient for proper stem cell identity and *wus* mutants

fail to organise a primary shoot meristem in the embryo and shoot meristems terminate prematurely (Laux et al. 1996). It has also been shown that *WUS* expression induce *CLV3* expression in the central zone (Schoof et al. 2000). What has also been shown is that the CLAVATA genes act together in a pathway to repress *WUS* activity (Fletcher et al. 1999; Brand et al. 2000; Schoof et al. 2000). Therefore a self-regulating feedback loop between CLV3 and WUS has been proposed (Sharma et al. 2003; Brand et al. 2000).

Mutants of members of the CLAVATA gene family have similar phenotypes; *clv1*, *clv2*, and *clv3* mutants all have enlarged shoot meristems and enlarged floral meristems carrying an increased number of floral organs such as petals and carpels (Clark et al. 1993, 1995; Kayes and Clark 1998). The *CLV3* gene encodes a protein that functions as a mobile intercellular signal and the *CLV1* gene encodes a receptor kinase that has been shown to bind with the CLV3 protein (Lenhard and Laux 2003; Clark et al. 1997; Fletcher et al. 1999; Ogawa et al. 2008). The *CLV1* expression pattern partly overlaps the expression pattern of *CLV3*, but is also extended to a larger region including the organising centre (Clark et al. 1997; Fletcher et al. 1999). While activated the CLV1/CLV3 complex downregulates *WUS* expression. WUS in turn promotes – by an unknown mechanism – stem cell identity and *CLV3* expression in the central zone. This feedback loop guarantees that the number of stem cells in the shoot meristem is highly regulated. If too many stem cells are present the *CLV3* signal will be stronger and thus suppress *WUS* expression. As *WUS* expression decreases the stem cell inducing signal also decreases and fewer new stem cells are produced. If – on the other hand – there are too few stem cells in the meristem the signal that represses *WUS* will be weaker and the increased expression of *WUS* will promote production of new stem cells.

The CLAVATA2/CORYNE pathway. The *CLV2* gene encodes a receptor-like protein and it was once suggested that the CLV2 protein acts together as a complex with the CLV1 receptor to bind with the CLV3 protein (Jeong et al. 1999), but this hypothesis is inconsistent with data. Experiments with *clv2* and *clv1* single and double mutants show that CLV1 is significantly active even in absence of CLV2 (Kayes and Clark 1998). The *CORYNE* (*CRN*) gene encodes another receptor kinase and *crn* mutants have similar phenotypes as *clv* mutants. Experiments also show that it is likely that CLV2 acts together with CRN in a second pathway, a suggestion that would explain the inconsistency above (Müller et al. 2008).

Plant cells

Following is a brief and simplified description of the anatomy of plant cells – the building blocks of plants. For further reading see Alberts et al. (1994). Plant cells are together with animal cells so called *eukaryotes*; each cell has its own nucleus, containing most of the cell's genetic material – for example DNA

molecules – and encapsulated in a protecting membrane. A plasma membrane surrounds the interior of the cell and separates intracellular components from the extracellular environment. Everything inside the plasma membrane that is not organelles surrounded by membranes is referred to as the *cytosol* and the space outside the plasma membrane is called the *apoplast*. Various types of proteins are embedded in the plasma membrane. One important function of these membrane proteins is to transport specific molecules through the membrane between the interior and the exterior of the cell. The protecting plasma membrane together with these membrane proteins enable the plant cell to control its own intracellular environment. Plant cells – in contrast to animal cells – are also enclosed by cell walls. Cell walls provide plant cells with structural support and protection. They are rigid, but flexible; they can be bent, but have great tensile strength. Cell walls between neighbouring plant cells fuse together and are shared between pairs of cells.

Cell growth. Plant cells grow by an uptake of water from the apoplast (Schopfer 2006). An osmotic flow fuelled by a large difference between osmotic pressure in the apoplast and the cytoplasm drives water into the cytoplasm. This inflow of water results in a large internal *turgor pressure* in the cells. Turgor pressure is needed for a cell to keep its shape and rigidity. As the turgor pressure increases it counters the osmotic pressure difference and if the cell walls are kept static, equilibrium will be reached. But plant cells maintain a pressure difference by increasing the wall sizes; the turgor pressure puts cell walls under stress, and cell walls under stress are loosened by more material being added to the walls. Parallel to water inflow the cell is maintaining an uptake of solute to keep the osmotic pressure difference constant.

The growth of plant tissue is due to a delicate combination of isotropic and anisotropic growth, which results in the elongated structures of the stem and organs. Anisotropic growth of cells is a product of the arrangement of cell wall cellulose *microfibrils*. Microfibrils are thin fibres that are arranged in parallel strands around the cell and the orientation of the microfibrils follows microtubule cortical arrays (Paradez et al. 2006). *Microtubules* are part of the cytoskeleton and are involved in several developmental activities in cells. Microtubules can be depolymerised by application of oryzalin and lack of microtubules results in inhibition of cell division and affects cell growth rates (Corson et al. 2009).

Cell division. A plant cell will not grow indefinitely, instead it will after some time divide into two daughter cells. Cell division is a process of several phases. First the cell enters *mitosis*, the phase during which the chromosomes are duplicated into two identical sets in the cell nucleus. Subsequent to mitosis is *cytokinesis*, during which the plasma membrane, the nucleus, and the cytoplasm split into two daughter cells. In plant cells a new cell wall is also constructed between the two daughter nuclei during cytokinesis. The new cell

wall defines the division plane and it is still unknown how cells orient the division plane, but plant biologists have suggested that there is a correlation between the orientation of the division plane and cell shape. Hofmeister stated in 1863 that the division plane is perpendicular to the principal direction of growth of the cell, and in 1888 Errera formulated the rule that the division plane is the shortest path that divides the mother cell into two daughter cells of equal volume (Smith 2001, and references therein). Experiments with cells from tobacco plants showed that the division planes of spherical cells were oriented randomly while cells deformed by compression had their division planes perpendicular to the main axis, a result in accordance with both Hofmeister and Errera's statements (Lynch and Lintilhac 1997).

Studying cell division in plants is a relatively grateful task. As indicated above, it is possible to follow plant cell division even with – compared to modern equipment – a rather primitive microscope. Furthermore, cells in the epidermal layer of plant tissue divide anticlinal, which means that the division plane is perpendicular to adjacent cells. Therefore cell division can be studied and modelled by representing the epidermal layer as a two-dimensional surface.

As there is no sliding between neighbouring plant cells there is no possible way for plant cells to reorganise or migrate after cell division. And as the only means of signalling – neglecting apoplastic diffusion – is by local interactions between cells, the topology of the tissue is of outermost importance. This emphasises how important proper cell division is in plants as the topology of the tissue is determined by cell division.

Auxin and intercellular transport

Auxin is a family of plant hormones. In the context of this thesis the most important member is indole-3-acetic acid (IAA), which is commonly present in plants and plays an important role for plant development. Root gravitropism, cell division, and vascular patterning are all developmental processes that rely on functional auxin transport (Blancaflor and Masson 2003; Sieburth 1999; Campanoni and Nick 2005; Okada et al. 1991).

Auxin is also necessary and sufficient for initiation of new primordia at the shoot apical meristem (Reinhardt et al. 2000, 2003). Plants grown in the presence of auxin transport inhibitors lack lateral organs and take a pin-like form. However, new primordia are initiated if auxin is exogenously applied to such plants and the radial position of the applied auxin determines where the new primordia is initiated. Externally added auxin also disturbs the phyllotactic patterning at the meristem. In wild-type plants localised increase in concentration of auxin have been observed to preceed initiation of new primordia (Benková et al. 2003). These findings add together to the hypothesis that auxin is redistributed actively in the tissue and that peaks of auxin concentration determine where new primordia are to be initiated.

The chemiosmotic model. Most modern models for auxin transport are based on the chemiosmotic model (Rubery and Sheldrake 1974; Raven 1975). Auxin is present in two different forms, as a dissociated anion (IAA^-) and in an associated protonated (IAAH) form. The uncharged protonated form can freely pass the membranes between the compartments, while the anion cannot and must be actively transported across the membranes. The pH levels in wall compartments are lower than in cytosol compartments so without an active transport of the anion auxin will accumulate within the cytosol compartments predominately as the anion. An auxin efflux carrier allows the anion to move across the membrane and if the carrier is inhomogeneously distributed at the plasma membrane then it enables a mechanism for polarised auxin transport in the plant tissue.

PINFORMED1 and polarised auxin transport. The membrane protein PINFORMED1 (PIN1) is a putative auxin efflux mediator and is found mainly in the epidermal layer of cells. PIN1 mutants result in similar phenotypes as for wild-type plants cultured in auxin polar transport inhibitors. Phenotypes are inflorescence with no flowers or with a flower at the top, but without stamens and with petals of abnormal shapes (Okada et al. 1991).

PIN1 is polarised within cells and the localisation of the protein at the plasma membrane is a product of rapid cycling between cytosol and membrane compartments (Geldner et al. 2001). PIN1 has been observed to polarise towards new primordia and away from older ones (Heisler et al. 2005; Barbier de Reuille et al. 2006). The underlying mechanism is still unknown, but models for which PIN1-polarisation is dependent on auxin concentrations in neighbouring cells have been proposed (Jönsson et al. 2006; Smith et al. 2006). In the proposed models auxin concentrations in neighbouring cells attract PIN1 to the plasma membrane. The resulting polarisation of PIN1 generates a net flow of auxin towards cells with high concentrations of auxin leading to a positive feedback where localised high concentrations of auxin attract more auxin.

The models have in numerical simulations been able to generate regular patterns of peaks of auxin concentration separated with a wave-length determined by parameter values (Jönsson et al. 2006; Smith et al. 2006). With parameter values estimated from experiments the models generate peaks separated by a distance of about five to seven cells.

Auxin influx carriers. So far the discussion has been focused on auxin efflux, but the genome of *Arabidopsis* also holds four genes, *AUX1*, *LAX1*, *LAX2*, and *LAX3* that encodes putative auxin influx mediators (Parry et al. 2001). The product of the *AUX1* gene is a protein that is localised to the plasma membrane and acts as an auxin influx mediator (Swarup et al. 2004; Yang et al. 2006). Single mutants of AUX1 or members of the LAX gene family show no visible phenotype, but apices of *pin1 aux1* double mutants treated with applied auxin resulted in initiated organs much wider than for *pin1* single mutants (Reinhardt et al. 2003; Bainbridge et al. 2008). Organ initiation is

present in double, triple, and quadruple *aux1*, *lax1*, *lax2*, and *lax3* mutants, but the resulting phyllotactic pattern is highly disorganised (Bainbridge et al. 2008). These results suggest that AUX1 and the LAX genes are not required for organ initiation, but contribute to the arrangement and the size of primordia. Computer simulations have shown that AUX1 can help to stabilise phyllotactic patterns (Heisler and Jönsson 2006).

Auxin is colocalised with AUX1 in the epidermal layer (Smith et al. 2006). *aux1 lax1 lax2* triple mutants show a weak expression of auxin in subepidermal layers and a proposed function for AUX1 is to reduce the effect of diffusion of auxin into subepidermal layers to keep auxin in the epidermal layer of the meristem (Bainbridge et al. 2008). Another proposed function of AUX1 is to increase the uptake of apoplastic auxin to counter apoplastic diffusion.

Auxin flux models. There are additional models based on polarised auxin transport. Leaf vascular patterns of *Arabidopsis* plants in presence of auxin transport inhibitors are disturbed and *pin1* mutants display vascular defects (Mattsson et al. 1999, and references therein). Therefore it has been suggested that auxin and PIN1 are also key components in vascular pattern formation in – for example – the leaf. The models described above have been unsuccessful in reproducing vascular patterns of *Arabidopsis* leaves, instead another family of models also based on polarised auxin transport have been proposed. The canalisation hypothesis first presented by Sachs (1969) – which states that the permeability for auxin transport between cells increases by auxin flux – has been the foundation for several models of vascular pattern formation in plants (Mitchison 1981; Feugier et al. 2005; Fujita and Mochizuki 2006). In earlier models the permeability for auxin transport increased by auxin flux while in later models PIN1 is explicitly taken into consideration; in these models the polarisation of PIN1 is dependent on auxin flux instead of auxin concentrations in neighbouring cells.

The canalisation hypothesis in its different incarnations has been proven to be a good candidate as a mechanism for formation of veins in plant leaves. Still these models are limited as they are unable to spontaneously generate patterns. They rely heavily on boundary conditions; a common requirement is the presence of auxin sinks and/or sources.

Methodology

There are two types of dynamics that have been studied in this thesis. Paper I and Paper V are about chemical reactions while Paper II, Paper III, and Paper IV are about mechanical properties of plant cells. A number of different numerical and analytical methods have been used to study the different problems. The modelling approaches, analytical methods, and numerical methods of this thesis are described in this following chapter.

Modelling chemical reactions

Paper I and Paper V are about chemical reactions. The approach used in both these papers to deal with chemical reactions is to use the law of mass action. The law of mass action is a model by Guldberg and Waage and deals with both the relation between chemical reactants at equilibrium and reaction rates for systems not at equilibrium (Lund 1965, and references therein).

Consider a reaction among n chemical species

$$a_1\mathrm{X}_1 + \ldots + a_n\mathrm{X}_n \rightleftharpoons b_1\mathrm{X}_1 + \ldots + b_n\mathrm{X}_n. \tag{1}$$

The integers a_i and b_i are called the *stoichiometric* coefficients. The reaction is in equilibrium when the entropy is at a maximum. For an isolated system this requirement is equivalent to

$$\Delta G = \sum_{i=0}^{n} q_i \mu_i = 0, \quad \text{where} \quad q_i = b_i - a_i, \tag{2}$$

ΔG is the change of free energy, and μ_i is the chemical potential for species i, which can be written as

$$\mu_i = k_B T \ln(c_i/c_0) + \mu_i^0(T, c_0), \tag{3}$$

where k_B is Boltzmann's constant, T is the temperature, c_i is the concentration of reactant i, c_0 is a reference concentration, and μ^0 is the standard chemical potential for a given reference concentration and temperature. For a reference

concentration equal to one molar, Equation 2 can be rewritten to

$$\prod_{i=0}^{n} c_i^{q_i} = e^{-\Delta G^0/k_B T} = K_{\text{equilibrium}}, \tag{4}$$

where $K_{\text{equilibrium}}$ is the equilibrium constant and ΔG^0 is defined as

$$\Delta G^0 = \sum_{i=0}^{n} q_i \mu_i^0(T). \tag{5}$$

Equation 4 gives the relation between concentrations of reactants at equilibrium. The law of mass action states that if the system is not at equilibrium the rate of a reaction is proportional to the concentrations of the reactants involved in the reaction, *i.e.* the forward and backward rates of the reaction are

$$r_+ = k_+ \prod_{i=0}^{n} c_i^{a_i}, \quad \text{and} \quad r_- = k_- \prod_{i=0}^{n} c_i^{b_i}, \tag{6}$$

where k_+ and k_- are proportionality constants.

It should be noted that when the system is at equilibrium there is a flow in both directions of the reaction, but the net flow is zero. To reach the results in Equation 4 and Equation 6 a macroscopic point of view has been taken and the reactants are assumed to be well mixed together. For a throughout discussion about the law of mass action, see Nelson (2004).

Michaelis-Menten kinetics. The reaction rates are in many cases extremely slow. Enzymes are structures that have a catalytic effect on a reaction and enhance the rate of a chemical reaction. An enzyme E binds to a reactant S called the substrate and turns it to a product P. The chain of reactions is the following

$$\mathrm{S} + \mathrm{E} \underset{k_2}{\overset{k_1}{\rightleftharpoons}} \mathrm{SE} \xrightarrow{k_3} \mathrm{P} + \mathrm{E}. \tag{7}$$

Two assumptions are made to get a mathematical representation of the reaction in Equation 7. The first assumption is that the amount of substrate-bound enzyme SE is quasi-stable and changes much slower than the amounts of substrate and product ($k_1, k_2 \gg k_3$). The second assumption is that the total amount of enzyme is constant, *i.e.* $[\mathrm{E}_{\text{total}}] = [\mathrm{E}] + [\mathrm{SE}]$. With these two assumptions the reaction rate is

$$r = r_{\max} \frac{[\mathrm{S}]}{K + [\mathrm{S}]}, \quad \text{where} \quad r_{\max} = k_3[\mathrm{E}_{\text{total}}], \quad \text{and} \quad K = \frac{k_2 + k_3}{k_1}. \tag{8}$$

Equation 8 is called the Michaelis-Menten rule and the constant K is called the Michaelis constant. The important feature of this kind of reaction is that the reaction rate is saturated. The law of mass action tells us that the reaction

rate is proportional to the substrate, but the reaction in Equation 7 is bottlenecked by the intermediate step, and the reaction rate is limited by the amount of enzyme. The Michaelis-Menten rule can also be used to model intracellular transport of – for example – auxin by an influx or efflux mediator. Then the rate of auxin flow will be limited by the number of available transport mediators at the plasma membrane

The reaction in Equation 7 can be generalised. Assume that n substrate molecules bind to the enzyme instead of only one. Following the same path of derivations as above the reaction rate is now

$$r = r_{\max} \frac{[\mathrm{S}]^n}{K^n + [\mathrm{S}]^n}. \tag{9}$$

Equation 9 is called the Hill equation while n is called the Hill coefficient and is a measurement of the cooperativity of the reaction.

The chemiosmotic model revisited. The law of mass action can be applied to the chemiosmotic model. The protonated form of auxin is dissociated according to the following reaction

$$\mathrm{IAAH} \rightleftharpoons \mathrm{IAA}^- + \mathrm{H}^+. \tag{10}$$

The reaction is assumed to be fast and the equilibrium constant K for the reaction is

$$K = \frac{[\mathrm{IAA}^-] \cdot [\mathrm{H}^+]}{[\mathrm{IAAH}]}. \tag{11}$$

The fractions of dissociated anion and the protonated form are then equal to

$$f_{[\mathrm{IAA}^-]} = \frac{10^{p\mathrm{H}-pK}}{10^{p\mathrm{H}-pK}+1}, \quad \text{and} \quad f_{[\mathrm{IAAH}]} = \frac{1}{10^{p\mathrm{H}-pK}+1}, \tag{12}$$

where $p\mathrm{H} = -\log[\mathrm{H}^+]$ and $pK = -\log K$. From Equation 12 it can be seen that the protonated form will dominate if pH levels are low – as in the apoplast – while that the anion will dominate if pH levels are high – as in the cytosol.

Modelling mechanics: The spring model

The spring model is an approach to model mechanical properties of cells in the epidermal layer – in this thesis as a two-dimensional sheet. In the spring model cells are represented by a network of vertices connected by edges corresponding to cell walls. Cell walls are treated as mechanical springs, hence the name of the model. Vertices are treated as being in a viscous medium, *i.e.* the velocities of vertices are directly proportional to the forces acting at them.

The contribution of forces from walls acting on vertex i is

$$\frac{d\mathbf{v}_i}{dt} = k_w \sum_{j \in \mathcal{V}(i)} \frac{\mathbf{u}_{ij}}{|\mathbf{u}_{ij}|} \left(\frac{|\mathbf{u}_{ij}| - L_{ij}}{L_{ij}} \right), \tag{13}$$

where $\mathbf{v}_i$ is the position of vertex i, $\mathbf{u}_{ij} = \mathbf{v}_j - \mathbf{v}_i$, k_w is the spring constant and determines the stiffness of walls, and L_{ij} is the resting length of the wall connecting vertices i and j. The summation is over vertices connected via edges to vertex i.

Plastic growth is assumed for cell walls. Cell walls grow under tension as new material is added. In the spring model resting lengths of cell walls are increased as walls are being stretched.

$$\frac{dL_{ij}}{dt} = k_g \Theta \left(\frac{|\mathbf{u}_{ij}| - L_{ij}}{L_{ij}} - T \right). \tag{14}$$

k_g is a constant setting the rate of growth and Θ is the ramp function defined as

$$\Theta(x) = \begin{cases} x & \text{if} \quad x \geq 0 \\ 0 & \text{if} \quad x < 0 \end{cases}. \tag{15}$$

T is a threshold that must be exceeded before new material is added to the wall.

Microtubules. Mechanical anisotropy by microfibrils is modelled by defining a microtubule direction $\mathbf{n}_{\text{microtubule},i}$ for each cell i. The spring constants of cell walls are then updated according to

$$k_w \rightarrow k_{w,j} = k_{\text{isotropic}} + k_{\text{anisotropic}} \sum_{i \in \mathcal{C}(j)} |\mathbf{n}_{\text{microtubule},i} \cdot \mathbf{n}_{\text{wall},j}|^2, \tag{16}$$

where $k_{\text{isotropic}}$ and $k_{\text{anisotropic}}$ are the isotropic and anisotropic contributions respectively, and $\mathbf{n}_{\text{wall},j}$ is the direction of wall j. The summation is over the one or two cells that are neighbours to wall j.

Stress direction. In Paper II the hypothesis is that the alignment of microtubules is regulated by mechanical stress. Circular statistics is used to calculate the stress direction of a cell according to

$$\theta_{\text{microtubule},i} = \frac{1}{2} \text{atan} \left(\frac{\sum_{j \in \mathcal{W}(c)} f_{\text{wall},j} \sin\left(2\theta_{\text{wall},j}\right)}{\sum_{j \in \mathcal{W}(c)} f_{\text{wall},j} \cos\left(2\theta_{\text{wall},j}\right)} \right), \tag{17}$$

where $\theta_{\text{microtubule},i}$ is the direction of the microtubules of cell i, $f_{\text{wall},j}$ is the force of wall j, and $\theta_{\text{wall},j}$ is the direction of wall j.

Analytical methods

Different analytical methods have been used to study the models of this thesis. These methods are explained in this section.

Fixed point stability analysis. Given a system of ordinary differential equations it is often of interest to study the system when it is close to equilibrium. Consider the system

$$\frac{d\mathbf{x}}{dt} = f(\mathbf{x}). \tag{18}$$

If $f(\mathbf{x}^*) = 0$ then $\mathbf{x}^*$ is called a *fixed point*. For a fixed point the time-derivative is equal to zero and the system is at equilibrium. A fixed point can be either *stable* or *unstable*. A common way to find the stability of a fixed point is to linearise the system at the fixed point. Let $\boldsymbol{\epsilon}$ be a small perturbation from the fixed point, *i.e.* $\mathbf{x} = \mathbf{x}^* + \boldsymbol{\epsilon}$, then Equation 18 can be expanded in a Taylor series

$$\frac{d\boldsymbol{\epsilon}}{dt} = f(\mathbf{x}^* + \boldsymbol{\epsilon}) \approx f(\mathbf{x}^*) + \mathcal{J}\boldsymbol{\epsilon} = \mathcal{J}\boldsymbol{\epsilon}, \tag{19}$$

where $\mathcal{J}$ is the Jacobian matrix and is defined as

$$\mathcal{J}_{ij} = \frac{\partial f_i}{\partial x_j}. \tag{20}$$

Assuming that there are no degenerated eigenvalues to the Jacobian matrix the solution to Equation 19 equals to

$$\boldsymbol{\epsilon} = c_1\mathbf{v_1}e^{\lambda_1 t} + \ldots + c_n\mathbf{v_n}e^{\lambda_n t}, \tag{21}$$

where λ_i and $\mathbf{v_1}$ are the eigenvalues and eigenvectors of the Jacobian matrix, and c_i are constants determined by initial conditions. If the real parts of all eigenvalues are negative then the perturbation $\boldsymbol{\epsilon}$ vanishes with time; the fixed point is a stable fixed point. If the real part of at least one eigenvalue is positive then the perturbation will grow with time; the fixed point is an unstable fixed point. For further reading about analysis of fixed points, please see Strogatz (2000).

Robustness analysis. While modelling a biological system parameters are in most cases considered to be constants. But in a real life situation many parameters depend on environmental changes such as temperature, acidity, pressure, and so forth. For example both the equilibrium constant $K_{\text{equilibrium}}$ in Equation 4 and the proportionality constants k_+ and k_- in Equation 6 are dependent on the temperature. A model must be robust against environmental changes, a parameter value can be difficult to estimate, and the model itself is most likely to be a simplification, so it is therefore important to test the model for parameter perturbations.

One way to measure robustness is to calculate the sensitivity, here defined as

$$S = \frac{\partial C}{\partial p}\frac{p}{C} \approx \frac{C_{\text{perturbed}} - C_{\text{unperturbed}}}{p_{\text{perturbed}} - p_{\text{unperturbed}}} \times \frac{p_{\text{unperturbed}}}{C_{\text{unperturbed}}}, \tag{22}$$

where C is a measurable and p is a parameter (Savageau 1971). If the magnitude of the sensitivity is equal to one then a change of the parameter results in a

corresponding relative change of the measurable. A higher or lower magnitude of the sensitivity equals to a stronger or weaker response. If the sensitivity is negative then the measurable decreases as the parameter is increased. One advantage of the sensitivity measurement is that it is independent of magnitudes. Often the sensitivity is used to compare parameters in order to pin-point what parts of the model that are most sensitive to perturbations.

Another way to analyse the robustness is to have all but one or more parameters fixed, vary the free parameters, and plot the measurable as a function of these variables. While the sensitivity measurement is localised to a small region close to the unperturbed parameter value this approach gives information about an extended region in parameter space. The drawback is that the approach does not give a quantative measurement of the robustness that can be used to compare parameters or models.

Numerical methods

Even simple biological systems are often represented by mathematical equations that are not possible to solve analytically and one must rely on numerical methods to get an approximative solution to the problem. The numerical methods used in this thesis are given a brief overview in the following section. For further references see a standard work on numerical methods such as Kincaid and Cheney (2002) or Press et al. (2002).

Numerical solutions of ordinary differential equations. Most problems in this thesis are expressed mathematically as systems of ordinary differential equations. These equations are of the form

$$\frac{d\mathbf{x}}{dt} = f(\mathbf{x}), \tag{23}$$

where $\mathbf{x}$ is the state vector of the system and f is a vector-valued function. With a boundary condition most equations in the form of Equation 23 have a well defined solution. In this thesis the boundary condition is always an initial state $\mathbf{x}_0$ for time $t = 0$.

The most simple example of a numerical solver for ordinary differential equations is Euler's method. Euler's method is a so called Taylor-series method and is obtained by a series expansion of $\mathbf{x}(t + h)$ to the first order,

$$\mathbf{x}(t + h) = \mathbf{x}(t) + hf(\mathbf{x}) + \mathcal{O}(h^2), \tag{24}$$

where h is a step size in time. Euler's method is said to be of first order as the global error scales as the step size h. The advantage of the method is that it is very simple to implement; the function f does not – in contrast to other fancier methods – need to be differentiated. The disadvantage of the method is that – to limit the global error – the step size h must be very small. A small step size

means a large amount of iterations and the gain in simplicity is quickly lost in computational costs.

More elegant methods can be constructed by a clever use of series expansions. The Runge-Kutta method is such a kind of method and combines information from several Euler-style steps and uses that information to make a more accurate step forward in time. The fourth-order Runge-Kutta method is as follows,

$$\mathbf{x}(t+h) = \mathbf{x}(t) + \frac{1}{6}(\mathbf{k}_1 + 2\mathbf{k}_2 + 2\mathbf{k}_3 + \mathbf{k}_4) + \mathcal{O}(h^5), \tag{25}$$

where

$$\mathbf{k}_1 = hf(\mathbf{x}(t)), \tag{26}$$

$$\mathbf{k}_2 = hf(\mathbf{x}(t) + \frac{1}{2}\mathbf{k}_1), \tag{27}$$

$$\mathbf{k}_3 = hf(\mathbf{x}(t) + \frac{1}{2}\mathbf{k}_2), \tag{28}$$

$$\mathbf{k}_4 = hf(\mathbf{x}(t) + \mathbf{k}_3). \tag{29}$$

The fourth-order Runga-Kutta method requires four evaluations of the function f for every step, but the increased accuracy gained makes the method attractive. For most problems the fourth-order Runge-Kutta method is good enough and can be used as a general method to solve ordinary differential equations. It is not the most accurate nor the fastest algorithm, but the method is simple to implement and the function f – as with Euler's method – needs not to be differentiated.

Still there are improvements to be made. When choosing a step size the characteristics of the function f must be taken into consideration. In the discussion above the step size h has been kept constant, but there might be regions where f is well-behaved, and a larger step size could have been used, and regions where f is less well-behaved, and a smaller step size is needed. If additional calculations are carried out the local truncation error can be estimated and the step size can be adjusted accordingly. The Runge-Kutta-Fehlberg method is an algorithm that utilises a fourth-order together with a fifth-order Runge-Kutta method to measure the local truncation error and adjusts the step size adaptively. The method is cleverly crafted such that only six function evaluations are needed for every step in time.

Adaptive control of the step size comes with a potential increase in performance; the gains in using an adaptive step size can be huge compared with the extra computational costs from the additional function evaluations. But methods like the Runge-Kutta-Fehlberg method are not suitable for all kinds of problems. Cell division is an example of a situation for which the function f changes drastically due to a discrete event. For simulations of discrete events it is often better to use for example a fourth-order Runge-Kutta method with a constant step size.

Numerical equation solvers. In Paper I the focus is on equilibrium concentrations of chemical reactants. The problem of finding the equilibrium concentrations is equivalent to finding a solution $\mathbf{x}^*$ such that $f(\mathbf{x}^*) = 0$. In one dimension this equation can be solved by the bisection method also known as the method of interval halving. This method assumes that there is one and only one solution in a range [a, b] determined by an initial guess. The signs of $f(a)$ and $f(b)$ are compared with the sign of $f(c)$, where $c = \frac{1}{2}(a + b)$, to determine if the solution lies in the range [a, c] or [c, b]. This step of interval halving is recursively repeated until a stopping criteria is fulfilled. Granted that there is only one solution the method guarantees convergence.

For a system of equations Newton's method can instead be used. The method starts with an initial guess $\mathbf{x}$ and the solution is assumed to be $\mathbf{x}^* = \mathbf{x} + \mathbf{h}$. A Taylor-series expansion to the first order gives

$$0 = f(\mathbf{x}^*) = f(\mathbf{x} + \mathbf{h}) \approx f(\mathbf{x}) + \mathcal{J}\mathbf{h}, \tag{30}$$

where $\mathcal{J}$ is the Jacobian matrix (Equation 20). To find the step $\mathbf{h}$ Equation 30 can be solved either by Gaussian elimination or by inverting the Jacobian matrix. This procedure is repeated until a stopping criteria is fulfilled. Newton's method does not guarantee convergence. Therefore the implementation of the method must keep track of the number of iterations, stop the algorithm when a maximum number of iterations has been reached, and start over with a new initial guess – unless a solution has already been found.

Optimisation algorithms. Let $\mathbf{y}(\mathbf{p})$ be the output of a system given a set $\mathbf{p}$ of parameter values. Say that the parameter values are unknown, but that a set of data $\mathbf{y}^*$ is supplied and that we want to find an optimal parameter set $\mathbf{p}^*$ such that $\mathbf{y}(\mathbf{p}^*) = \mathbf{y}^*$. A straightforward approach to this problem is to systematically scan the parameter space until a solution is found. This approach will most likely fail as for even small systems the computational time of trying every possible combination will exceed the life time of the implementor. The common approach to most optimisation problems is not to look for the optimal solution, but instead try to find a solution that is good enough. To do this the fitness of a solution given a set of parameter values is quantified by an objective function. An example of an objective function is

$$E(\mathbf{p}) = \sum_i (y_i^* - y_i(\mathbf{p}))^2. \tag{31}$$

The optimisation problem can now be rephrased to find the minimum of the objective function. To find a minimum of the objective function it is possible to just go downhill the gradient of the function. This approach has its weaknesses; if there are more than one minimum – for example if the objective function has one or several local minima – then the minima closest to an initial guess is most likely to be found.

The simulated annealing method is an optimisation algorithm that can be used to find a local minimum. For the algorithm the objective function is considered as an energy and a virtual temperature T is introduced. The algorithm starts with an initial – often randomly chosen – set of parameter values. A new set of parameter values $\mathbf{p}_{\text{new}}$ is randomly selected, often by a step to an adjacent point in a discretised parameter space. If the energy $E(\mathbf{p}_{\text{new}})$ corresponding to the new set of parameter values is lower than the energy $E(\mathbf{p}_{\text{old}})$ corresponding to the old set of parameter values, then the new set of parameter values is kept and the old set is discarded. Otherwise the new set of parameter values is kept with a probability

$$P = e^{-\Delta E/T}, \tag{32}$$

where $\Delta E = E(\mathbf{p}_{\text{new}}) - E(\mathbf{p}_{\text{old}})$. The probability in Equation 32 enables the algorithm to sometimes walk uphill in the energy landscape, and thus it is possible for the algorithm to get out of a local minimum. The virtual temperature T starts at a high temperature and is successively reduced towards zero. For high temperatures the probability in Equation 32 is close to unity and the algorithm has the behaviour of a random walk in parameter space. As the temperature is lowered the system is "frozen" and the algorithm becomes greedy and seeks nearby minima. The algorithm is closely related to the field of thermodynamics and the probability in Equation 32 is the Boltzmann factor.

Summary of publications

Here follows a summary of the papers that are part of this thesis with descriptions of my contribution to each paper.

Paper I

In Paper I we develop two models of the CLAVATA-WUSCHEL feedback network to study the differences in phenotypes of two *clavata1* mutants. The main topic is the question how the *clv1-1* non-null mutant can have a greater phenotype – measured in number of carpels — than the *clv1-11* null mutant. It has been suggested that this counterintuitive result is due to interference between the CLAVATA1 and the CORYNE pathways. The two models we present differ only in how we implemented the *clv1-1* non-null mutant. For the first model – the *interference model* – the receptors CLAVATA1 and CORYNE form a complex with no function and which is immediately discarded. For the second model – the *loss-of-signal model* – the signal from activated CLAVATA1 is reduced.

Both implementations of the feedback network are dependent on a large amount of parameters with unknown values. We use an optimisation algorithm to find parameter values by fitting model output to data from wild type and four receptor mutant experiments. In a validation step we test the model against two receptor double mutant experiments. This procedure is repeated 25,000 times for each model and we end up with a few hundred parameter value sets for each model. We compare these sets of parameter values with an unbiased background parameter value distribution to make model predictions.

Both models show that the two receptor pathways are equally important, and that the strengths of the two are close to equal, but with a slight asymmetry with the CLAVATA1 pathway somewhat stronger than the CORYNE pathway. For the interference model the main prediction is that we expect a large amount of receptors, both of CLAVATA1 and CORYNE. For the loss-of-signal model the main prediction is that CLAVATA1 sequesters CLAVATA3 in the *clv1-1* mutant. The sequestration of CLAVATA3 by CLAVATA1 could be caused by – for example – internalisation or degradation of bound CLAVATA1 receptors.

My contribution: I developed the two models together with my supervisor

and I implemented the models, the numerical equation solver, and the optimisation algorithm. I did all simulations and optimisations. I took part of the following data analysis together with Pontus Melke and I contributed to the final manuscript.

Paper II

Paper II is an interdisciplinary group effort to test the hypothesis that microtubular cortical arrays in cells align according to stress patterns in the plant tissue. This hypothesis implies that mechanical signals in the plant are used as cues for anisotropic growth as microfibrils in cells are believed to align with microtubular cortical arrays. Microtubules are possible to be observed in experiments using markers and confocal microscopy, but stress patterns in a cell tissue are currently impossible to measure directly. We use mathematical models to predict stress patterns at the surface of the shoot apical meristem. These patterns are compared with the direction of microtubules in experiments.

We implement the spring model as a representation of the epidermal layer of the shoot apical meristem. In experiments the microtubules are aligned circumferentially at the periphery and the base of the meristem while they are randomly oriented at the summit. In accordance with experiments the spring model predicts the stress patterns to be circumferential at the periphery and less organised at the summit. In experiments microtubules also align along the boundary between the meristem and new primordia. The spring model is also able to successfully predict the expected stress pattern.

Ablation experiments in which individual cells at the summit of the meristem are destroyed by a laser are also conducted. In these experiments the microtubules in cells surrounding the wound align circumferential around the wound. The change of detail – from tissue level to cell level – in these experiments requires us to use a finite-element method (FEM) to model the surrounding of the wound. The stress patterns of the FEM model are circumferential around the wound. All these results help to strengthen the hypothesis that microtubules align according to feedback from stress patterns in the tissue.

My contribution: I contributed to the implementation of a three-dimensional model with a two-dimensional spring model representing the epidermal layer. I participated in the discussion related to the development of the model.

Paper III

We test two different rules for orienting the division plane during cell division. The first rule is our representation of Errera's rule and divides the mother cell such that the division plane is the shortest path through the cell. The second rule orients the division plane randomly. The spring model is used for simulations and we perform two parallel series of simulations; one with cell

wall mechanics and one without. Distributions of number of neighbours are measured from resulting tissues and we compare them with experimental data. We also introduce a quantative measurement of cell shape and compare the shapes of cells in simulations with shapes of cells in experiments.

We show that the distributions of number of neighbours measured from tissues resulting from simulations with the the two division rules are different, with the shortest path – or Errera's – division rule performing better than the random direction division rule. We also show that – while visual inspection of the tissues shows a difference – for simulations with and without mechanics the distributions of number of neighbours are the same. Comparing cell shapes we show that the shortest path division rule results in more plant-like cell shapes, while simulations without mechanics result in the least plant-like cell shapes.

My contribution: I implemented the two-dimensional spring model and performed all simulations. I did the following data analysis and contributed to the manuscript.

Paper IV

What is presented in Paper IV is a continuation of the project presented in Paper III. We use the same two-dimensional spring model as in Paper III to study cell division in the epidermal layer of the shoot apical meristem. In Paper III the two division rules oriented the division plane such that it passed the centre of mass of the mother cell. In Paper III we test another approach for which the division plane can be randomly oriented in the mother cell. We show by comparing simulated tissue with experiment data that the "centre of mass"-mechanism is superior to the randomised approach for modelling the tissue. This result is tied together with our main result that division rules that divide the mother cell into two symmetrically shaped daughter cells better reproduce topologies and geometries seen in experiments than division rules that divide the mother cell asymmetrically. Oryzalin depolymerises microtubules and cell division is suspended in experiment if oryzalin is applied to the plant. We test the spring model with a series of simulations without cell division and we see that the distribution of internal vertex angles converges towards 120°, as seen in experiments.

My contribution: I implemented the two-dimensional spring model and performed all simulations. I did the following data analysis and contributed to the manuscript.

Paper V

We analyse the proposed PIN1-dependent polarised auxin transport as a candidate for the pattern generating mechanism at the shoot apical meristem. The

model previously presented by Jönsson et al. (2006) is generalised and analysed by a stability analysis of the homogenous fixed point. The stability analysis is used to find requirements for pattern generation and predictions about the characteristics of final patterns. We compare the predictions with numerical simulations and the numerical simulations confirm our predictions from the analysis. We are able to predict the wave-length of the final pattern by linearisation of the homogenous fixed point. The requirements on the generalisation of the model are useful for further studies of polarised auxin transport as they can tell what kind of mechanisms that can be used for for pattern generation.

In the model PIN1-cycling is regulated by feedback from auxin concentrations in neighbouring cells. We show that this mechanism works for both exocytosis as well as for endocytosis. This result is of value as experiments have shown that auxin can affect PIN1 endocytosis (Paciorek et al. 2005). We also show that if PIN1-cycling is regulated, not by feedback from auxin concentrations in neighbouring cells, but by feedback from auxin concentrations in neighbouring walls then the model is unable to generate patterns.

In our analysis we find that AUX1 is not needed for pattern generation while PIN1 is crucial. Auxin-induced transport mediators are introduced and our analysis shows that auxin-induced PIN1 stabilises the homogenous fixed point while auxin-induced AUX1 functions in the opposite direction and destabilises the homogenous fixed point. These results agree with previous studies that show that auxin-induced PIN1 destabilises non-homogenous patterns and removal of AUX1 results in loss of stability of non-homogenous patterns (Heisler and Jönsson 2006).

The model is also able to generate patterns other than peaks, such as peaks with stripes, stripes, and reentrant (inverted) peaks. The parameters for which the model generates these patterns are found on the boundary in parameter space that separates parameters that result in peak pattern and parameters that result in no patterns.

My contribution: I implemented the model and performed all simulations with the generalised model. I did the following data analysis and contributed to the manuscript. The analysis of the model was done mainly by me with the help from Bo Söderberg.

Acknowledgement

I would like to thank all former and present members of the Department of Astronomy & Theoretical Physics, especially those of the Computational Biology & Biological Physics group. In particular I want to thank my supervisor Henrik Jönsson for guidance over these years. In addition I want to express my gratitude to the members of the plant group, Pawel Krupinski, Pontus Melke, and Bo Söderberg.

I also want to thank my collaborators at Caltech, USA, and in Lyon, France, Vijay S. Chickarmane, Olivier Hamant, Marcus G. Heisler, Elliot M. Meyerowitz, Bruce E. Shapiro, and Jan Traas.

Bibliography

Alberts, B., D. Bray, J. Lewis, M. Raff, K. Roberts, and J.D. Watson (1994), *Molecular biology of the cell*, third edition. Garland Publishing, Inc. New York and London.

Bainbridge, K., S. Guyomarc'h, E. Bayer, R. Swarup, M. Bennett, T. Mandel, and C. Kuhlemeier (2008), "Auxin influx carriers stabilize phyllotactic patterning." *Genes & Development*, 22, 810–823.

Barbier de Reuille, P., I. Bohn-Courseau, K. Ljung, H. Morin, N. Carraro, C. Godin, and J. Traas (2006), "Computer simulations reveal properties of the cell-cell signaling network at the shoot apex in *Arabidopsis*." *Proceedings of the National Academy of Sciences of the United States of America*, 103, 1627–1632.

Benková, E., M. Michniewicz, M. Sauer, T. Teichmann, D. Seifertová, G. Jürgens, and J. Friml (2003), "Local, efflux-dependent auxin gradients as a common module for plant organ formation." *Cell*, 115, 591–602.

Blancaflor, E.B. and P.H. Masson (2003), "Plant gravitropism. unraveling the ups and downs of a complex process." *Plant Physiology*, 133, 1677–1690.

Bowman, J.L. and Y. Eshed (2000), "Formation and maintenance of the shoot apical meristem." *Trends in Plant Science*, 5, 110–115.

Brand, U., J.C. Fletcher, M. Hobe, E.M. Meyerowitz, and R. Simon (2000), "Dependence of stem cell fate in *Arabidopsis* on a feedback loop regulated by *CLV3* activity." *Science*, 289, 617–619.

Campanoni, P. and P. Nick (2005), "Auxin-dependent cell division and cell elongation. 1-naphthaleneacetic acid and 2,4-dichlorophenoxyacetic acid activate different pathways." *Plant Physiology*, 137, 939–948.

Clark, S.E., M.P. Running, and E.M. Meyerowitz (1993), "*CLAVATA1*, a regulator of meristem and flower development in Arabidopsis." *Development*, 119, 397–418.

Clark, S.E., M.P. Running, and E.M. Meyerowitz (1995), "*CLAVATA3* is a specific regulator of shoot and floral meristem development affecting the same processes as *CLAVATA1*." *Development*, 121, 2057–2067.

Clark, S.E., R.W. Williams, and E.M. Meyerowitz (1997), "The *CLAVATA1* gene encodes a putative receptor kinase that controls shoot and floral meristem size in *Arabidopsis*." *Cell*, 89, 575–585.

Corson, F., O. Hamant, S. Bohn, J. Traas, A. Boudaoud, and Y. Couder (2009), "Turning a plant tissue into a living cell froth through isotropic growth." *Proceedings of the National Academy of Sciences*, 106, 8453–8458.

Douady, S. and Y. Couder (1992), "Phyllotaxis as a physical self-organized growth process." *Physical Review Letters*, 68, 2098–2101.

Feugier, F.G., A. Mochizuki, and Y. Iwasa (2005), "Self-organization of the vascular system in plant leaves: Inter-dependent dynamics of auxin flux and carrier proteins." *Journal of Theoretical Biology*, 236, 366–375.

Fletcher, J.C., U. Brand, M.P. Running, R. Simon, and E.M. Meyerowitz (1999), "Signaling of cell fate decisions by *CLAVATA3* in *Arabidopsis* shoot meristems." *Science*, 283, 1911–1914.

Fujita, H. and A. Mochizuki (2006), "Pattern formation of leaf veins by the positive feedback regulation between auxin flow and auxin efflux carrier." *Journal of Theoretical Biology*, 241, 541–551.

Geldner, N., J. Friml, Y.D. Stierhof, G. Jürgens, and K. Palme (2001), "Auxin transport inhibitors block PIN1 cycling and vesicle trafficking." *Nature*, 413, 425–428.

Heisler, M.G. and H. Jönsson (2006), "Modeling auxin transport and plant development." *Journal of Plant Growth Regulation*, 25, 302–312.

Heisler, M.G., C. Ohno, P. Das, P. Sieber, G.V. Reddy, J.A. Long, and E.M. Meyerowitz (2005), "Patterns of auxin transport and gene expression during primordium development revealed by live imaging of the *Arabidopsis* inflorescence meristem." *Current Biology*, 15, 1899–1911.

Jeong, S., A.E. Trotochaud, and S.E. Clark (1999), "The Arabidopsis *CLAVATA2* gene encodes a receptor-like protein required for the stability of the CLAVATA1 receptor-like kinase." *Plant Cell*, 11, 1925–1934.

Jönsson, H., M.G. Heisler, B.E. Shapiro, E.M. Meyerowitz, and E. Mjolsness (2006), "An auxin-driven polarized transport model for phyllotaxis." *Proceedings of the National Academy of Sciences of the United States of America*, 103, 1633–1638.

Kayes, J.M. and S.E. Clark (1998), "*CLAVATA2*, a regulator of meristem and organ development in *Arabidopsis*." *Development*, 125, 3843–3851.

Kincaid, D. and W. Cheney (2002), *Numerical Analysis: Mathematics of Scientific Computing*, third edition. Brooks/Cole.

Laux, T., K.F. Mayer, J. Berger, and G. Jürgens (1996), "The *WUSCHEL* gene is required for shoot and floral meristem integrity in *Arabidopsis*." *Development*, 122, 87–96.

Lenhard, M. and T. Laux (2003), "Stem cell homeostasis in the *Arabidopsis* shoot meristem is regulated by intercellular movement of CLAVATA3 and its sequestration by CLAVATA1." *Development*, 130, 3163–3173.

Lund, E.W. (1965), "Guldberg and Waage and the law of mass action." *Journal of Chemical Education*, 42, 548–550.

Lynch, T.M. and P.M. Lintilhac (1997), "Mechanical signals in plant development: A new method for single cell studies." *Developmental Biology*, 181, 246–256.

Mattsson, J., Z.R. Sung, and T. Berleth (1999), "Responses of plant vascular systems to auxin transport inhibition." *Development*, 126, 2979–2991.

Mayer, K.F.X., H. Schoof, A. Haecker, M. Lenhard, G. Jürgens, and T. Laux (1998), "Role of *WUSCHEL* in regulating stem cell fate in the *Arabidopsis* shoot meristem." *Cell*, 95, 805–815.

Meyerowitz, E.M. (1997), "Genetic control of cell division patterns in developing plants." *Cell*, 88, 299–308.

Mitchison, G.J. (1977), "Phyllotaxis and the Fibonacci series." *Science*, 196, 270–275.

Mitchison, G.J. (1981), "The polar transport of auxin and vein patterns in plants." *Philosophical Transactions of the Royal Society of London. B, Biological Sciences*, 295, 461–471.

Müller, R., A. Bleckmann, and R. Simon (2008), "The receptor kinase CORYNE of *Arabidopsis* transmits the stem cell-limiting signal CLAVATA3 independently of CLAVATA1." *The Plant Cell*, 20, 934–946.

Nelson, P. (2004), *Biological Physics: Energy, Information, Life*. W.H. Freeman, New York.

Ogawa, M., H. Shinohara, Y. Sakagami, and Y. Matsubayashi (2008), "*Arabidopsis* CLV3 peptide directly binds CLV1 ectodomain." *Science*, 319, 294.

Okada, K., J. Ueda, M.K. Komaki, C.J. Bell, and Y. Shimura (1991), "Requirement of the auxin polar transport system in early stages of *Arabidopsis* floral bud formation." *The Plant Cell*, 3, 677–684.

Paciorek, T., E. Zažímalová, N. Ruthardt, J. Petrášek, Y.D. Stierhof, J. Kleine-Vehn, D.A. Morris, N. Emans, G. Jürgens, N. Geldner, and J. Friml (2005), "Auxin inhibits endocytosis and promotes its own efflux from cells." *Nature*, 435, 1251–1256.

Paradez, A., A. Wright, and D.W. Ehrhardt (2006), "Microtubule cortical array organization and plant cell morphogenesis." *Current Opinion in Plant Biology*, 9, 571–578.

Parry, G., A. Marchant, S. May, R. Swarup, K. Swarup, N. James, N. Graham, T. Allen, T. Martucci, A. Yemm, R. Napier, K. Manning, G. King, and M. Bennett (2001), "Quick on the uptake: Characterization of a family of plant auxin influx carriers." *Journal of Plant Growth Regulation*, 20, 217–225.

Press, W.H., S.A. Teukolsky, W.T. Vetterling, and B.P Flannery (2002), *Numerical recipes in C: The Art of Scientific Computing*, second edition. Cambridge University Press.

Raven, J.A. (1975), "Transport of indoleacetic acid in plant cells in relation to ph and electrical potential gradients, and its significance for polar IAA transport." *New Phytologist*, 74, 163–172.

Reinhardt, D., T. Mandel, and C. Kuhlemeier (2000), "Auxin regulates the initiation and radial position of plant lateral organs." *The Plant Cell*, 12, 507–518.

Reinhardt, D., E.R. Pesce, P. Stieger, T. Mandel, K. Baltensperger, M. Bennett, J. Traas, J. Friml, and C. Kuhlemeier (2003), "Regulation of phyllotaxis by polar auxin transport." *Nature*, 426, 255–260.

Rubery, P. H. and A. R. Sheldrake (1974), "Carrier-mediated auxin transport." *Planta*, 118, 101–121.

Sachs, T. (1969), "Polarity and the induction of organized vascular tissues." *Annals of Botany*, 33, 263–275.

Savageau, M.A. (1971), "Parameter sensitivity as a criterion for evaluating and comparing the performance of biochemical systems." *Nature*, 229, 542–544.

Schoof, H., M. Lenhard, A. Haecker, K.F.X. Mayer, G. Jürgens, and T. Laux (2000), "The stem cell population of *Arabidopsis* shoot meristems is maintained by a regulatory loop between the *CLAVATA* and *WUSCHEL* genes." *Cell*, 100, 635–644.

Schopfer, P. (2006), "Biomechanics of plant growth." *American Journal of Botany*, 93, 1415–1425.

Sharma, V.K., C. Carles, and J.C. Fletcher (2003), "Maintenance of stem cell populations in plants." *Proceedings of the National Academy of Sciences of the United States of America*, 100, 11823–11829.

Sieburth, L.E. (1999), "Auxin is required for leaf vein pattern in Arabidopsis." *Plant Physiology*, 121, 1179–1190.

Smith, L.G. (2001), "Plant cell division: building walls in the right places." *Nature Reviews Molecular Cell Biology*, 2, 33–39.

Smith, R.S., S. Guyomarc'h, T. Mandel, D. Reinhardt, C. Kuhlemeier, and P. Prusinkiewicz (2006), "A plausible model of phyllotaxis." *Proceedings of the National Academy of Sciences of the United States of America*, 103, 1301–1306.

Strogatz, S.H. (2000), *Nonlinear Dynamics and Chaos: With Applications to Physics, Biology, Chemistry and Engineering (Studies in nonlinearity)*. Westview Press.

Swarup, R., J. Kargul, A. Marchant, D. Zadik, A. Rahman, R. Mills, A. Yemm, S. May, L. Williams, P. Millner, S. Tsurumi, I. Moore, R. Napier, I.D. Kerr, and M.J. Bennett (2004), "Structure-function analysis of the presumptive Arabidopsis auxin permease AUX1." *The Plant Cell*, 16, 3069–3083.

Weigel, D. and G. Jürgens (2002), "Stem cells that make stems." *Nature*, 415, 751–754.

Yang, Y., U.Z. Hammes, C.G. Taylor, D.P. Schachtman, and E. Nielsen (2006), "High-affinity auxin transport by the AUX1 influx carrier protein." *Current Biology*, 16, 1123–1127.

Paper I

Models of sequestration and receptor cross-talk for explaining multiple mutants in plant stem cell regulation

Patrik Sahlin[1], Pontus Melke[1] and Henrik Jönsson*[1]

[1]Computational Biology & Biological Physics, Lund University, Sölvegatan 14A, SE 223 62 Lund, Sweden

Email: Patrik Sahlin - sahlin@thep.lu.se; Pontus Melke - pontus@thep.lu.se; Henrik Jönsson*- henrik@thep.lu.se;

*Corresponding author

Abstract

Background: Stem cells reside in the plant shoot meristem throughout its life and are the main regulators of above-ground plant development. The stem cell maintenance depends on a feedback network between the *CLAVATA* and *WUSCHEL* genes. The CLAVATA3 peptide binds to the CLAVATA1 receptor leading to WUSCHEL inhibition. WUSCHEL, on the other hand, activates CLAVATA3 expression. Recent experiments suggest a second pathway where CLAVATA3 inhibits WUSCHEL by binding to the CORYNE receptor. An interesting question, central for understanding the receptor signaling, is why the *clavata1-11* null mutant have a weaker phenotype compared with *clavata1-1* non-null mutant. It has been suggested that this relies on interference from the mutated CLAVATA1 acting on the CORYNE pathway.

Results: We develop two models for the CLAVATA-WUSCHEL feedback network including two receptor pathways for WUS repression and differing only by the hypothezised mechanisms for the *clavata1-1* non-null mutant. The first model is an implementation of the previously suggested interference mechanism. The other model assumes an unaltered binding between CLAVATA3 and the mutated CLAVATA1 but with a loss of propagated signal into the cell. We optimize the models to data from wild type and four single receptor mutant experiments, and use data from two receptor double mutant experiments in a validation step. Both models are able to explain all seven phenotypes, and in addition qualitatively predict CLAVATA3 perturbations. The two models for the *clavata1-1* mutant differ in the direct mechanism of the mutant, but they also predict other differences in the dynamics of the stem cell regulating network. We show that the interference hypothesis leads to an abundance of receptors, while the loss-of-signal hypothesis leads to sequestration of CLAVATA3 and relies on degradation or internalization of the bound CLAVATA1 receptor.

Conclusions: Using computational modeling, we show that an interference hypothesis and a more parsimonious loss-of-signal hypothesis for a *clavata1* non-null mutant both lead to behaviors predicting wild type and six receptor mutant experiments. Although the two models have identical implementations of the unperturbed feedback network for stem cell regulation, we can point out model-predicted differences that may be resolved in future experiments.

Background

The development of animals and plants is dependent on undifferentiated stem cells residing in special locations called niches [1]. In a plant, stem cells are maintained in the shoot apical meristem (SAM) throughout its life, and the SAM is the source of all aerial parts of the plant [2,3].

Spatial regions of different expression patterns and functions are found within the SAM. The central zone is located at the tip of the apex and consists of slowly dividing stem cells expressing the *CLAVATA3* (*CLV3*) gene. Due to cellular growth and proliferation, stem cells from the central zone move into the surrounding tissue where the spatial location of each daughter cell is a main determinant of cell fate. Located below the central zone is a small group of cells that are believed to form a control zone for the organization of the SAM. These cells express the *WUSHEL* (*WUS*) gene, which encodes a homeodomain transcription factor and has been shown to be required for maintaining stem cells in the shoot [4]. Although not expressed in the same cells, WUS and CLV3 regulate the expression of each other. While WUS upregulates CLV3, the intercellular peptide CLV3 acts together with the receptor kinase CLAVATA1 (CLV1) in a signaling pathway that downregulates WUS [4–7]. This feedback network is a main regulator of stem cell maintenance in the SAM. If the number of stem cells is low the CLV3 signal will be weak and expression of WUS will increase, which in turn will induce CLV3 expression. If instead there is an abundance of stem cells, WUS will be downregulated and CLV3 expression will decrease.

Additional molecules have been identified as important for the stem cell regulation. The receptor-like CLAVATA2 (CLV2) is involved in WUS repression acting within the CLV3 signaling pathway [8]. Müller et al. (2008, 2009) [9, 10] recently identified a kinase CORYNE (CRN) that interacts with CLV2 and together form a receptor for CLV3. In addition, the BAM family of receptors has an antagonistic effect compared to CLAVATA1 in stem cell regulation [11, 12], and several members of the CLE (CLAVATA3/ESR-related) ligand family were shown to affect the SAM development in perturbation assays [13]. The intracellular components of the WUS-repressing signal are to a large extent unknown, but POLTERGEIST (POL) and POLTERGEIST-LIKE1 (PLL1) have been shown to be important for mediating the signal [14].

Reduction in CLAVATA signaling leads to increased WUS and CLV3 expressions and an increase in number of stem cells and shoot size [15]. Another phenotype related to CLAVATA signaling is the number of carpels produced in flowers. A number of *clv1* alleles have been shown to have different strenghts in these phenotypic traits. Somewhat unintuitively, the *clv1-11* null-mutant was shown to have a weaker phenotype than the non-null *clv1-1* mutant [16]. Müller et al. (2008) [9] also found that the *crn-1 clv1-1* double mutant showed weaker phenotype than the *crn-1 clv1-11* double mutant. It was suggested that the stronger phenotype of the *clv1-1* mutant compared to the null mutant is due to a functional overlap between multiple receptors, and that the dominant effect of *clv1-1* could relate to cross-talk with other receptors [16]. With the identification of CRN/CLV2, this receptor was suggested to be the target for an interference by the mutated CLV1 [9].

Several theoretical models have been used to investigate different aspects of the stem cell regulatory network in the SAM [17]. For example, spatial models using static cell-based SAM templates have been used to investigate how the WUS-activated CLV3 expression region could be localized to the central zone, and how WUS may be spatially activated via a pattern-forming mechanism [18,19]. The intracellular WUS activation network has been further investigated showing the importance of the hormone cytokinin for WUS activation [20], and a cell-population based model has been used to investigate uncoupling of the sizes of the *CLV3* and *WUS* domains at different growth conditions [21].

None of the published models have included multiple receptor pathways for the WUS-repressing signal, and in this paper we use computational modeling to investigate details of receptor and ligand turnover, interactions, and signaling. We focus on the differences in receptor mutants, where the main question is how a *clv1-11* null mutant can have a weaker phenotype than a *clv1-1* non-null mutant in the context of phenotypes for a number of single and double receptor mutants. We develop two models capturing the main aspects of the negative feedback loop for stem cell regulation. In the models, CLV3 binds to both CLV1 and CRN/CLV2 receptors, the bound receptors propagate a combined signal repressing WUS, and WUS induces CLV3 production. The two models only differ in the implementation of the *clv1-1* non-null mutant. The first model is used

to test the proposed idea of receptor interference as an explanation of the differences in phenotypes of *clv1* mutants and the second model is used to test a more parsimonious loss-of-signaling mutant hypothesis. A motivation for the second model is that the *clv1-1* has been identified as a missense mutation in the kinase part of the receptor [16].

A common problem for modeling biological systems is the abundance of unknown values for the kinetic reaction parameters. To adress this problem we use a parameter ensemble approach, where we for each model extract a number of parameter sets, chosen for the ability of the model (simulated with such a set of parameter values) to explain data from multiple mutant experiments [22]. For each model of the *clv1-1* mutant, the parameter sets provide a semi-global description of the model behavior, instead of a more parameter value dependent description that results if a single parameter set would be used.

We apply statistical tools on the parameter sets to obtain predictions about biological properties of the stem cell regulating network resulting from introducing the hypothezised mechanisms for the *clv1-1* mutant.

Results and Discussion

We implemented the stem cell regulatory network as a system of ordinary differential equations (ODEs) using standard mass action kinetics for molecular reactions (Fig. 1, Methods). The model consists of two receptors, CLV1 and CRN (representing the CRN/CLV2 receptor), that when bound to CLV3 repress WUS expression, and WUS-induced CLV3 expression.

Models of two clv1-1 hypotheses are both able to explain data from wild type and six receptor mutant experiments

To objectively obtain parameter values we compared the models with experimental data from wild type and the four receptor loss-of-function mutants *clv1-1*, *clv1-11*, *crn-1*, and *crn-1 clv2-1* (Methods). We implemented *clv1-11* and *crn-1 clv2-1* as null mutants, removing the receptors from the model, and the *crn-1* as a complete loss-of-signal mutant [9] (Methods). The *clv1-1* mutant is implemented as either a loss-of-signal mutant (*loss-of-signal model*, Fig. 1B) or by adding interference of the CRN receptor pathway (*interference model*, Fig. 1C). To compare phenotypic strength between a model and experiments, we use WUS levels as a measure in the models and compare with carpel numbers, which represent an experimental estimate of phenotypic strength, see e.g. [9, 16, 20] (Methods).

We used an optimization algorithm to find candidates for parameter values [23] and performed multiple optimizations to get an ensemble of parameter (value) sets for each of the two models (Methods). We performed 25,000 optimizations for each model and kept only parameter sets for which the model was able to reproduce data observed in the experiments (Fig. 2). For the two models the optimization algorithm found 21,968 (loss-of-signal) and 23,121 (interference) valid parameter sets (Fig. 2).

Given that the number of parameters in the model exceeded the number of available experiments, it was important to lower the tendency of overfitting. Hence we applied double mutants as an *a posteriori* validation step, where we compared data from simulations with data from the two double loss-of-function and null-mutants *crn-1 clv1-11* and *crn-1 clv1-1* (Tab. 1), keeping only parameter sets for which the models were able to explain the double mutants (Fig. 3). We observed that for most parameter sets the models showed too strong phenotypes for the double mutants (Fig. 3), and after the validation only 118 (loss-of-signal) and 531 (interference) parameter sets remained. The strong double mutant phenotypes in the simulations can be explained by that there is no other dynamic input to the system than the two pathways that are knocked out.

In conclusion, the loss-of-signal and interference models are both able to reproduce data seen in wild type, four single receptor, and two double receptor mutant experiments.

The loss-of-signal hypothesis implies sequestration of CLV3 for the clv1-1 mutant

The main difference between the two models is the implementations of the *clv1-1* mutant, which in each case is described by a single parameter – $k_{3,\mathrm{weak}}$ for the loss-of-signal model and k_8 for the interference model. For the loss-of-signal model, we observed that the average CLV1/CLV3 signal in the mutant ($k_{3,\mathrm{weak}}$) is an order of magnitude smaller than the wild type signal (k_3) (Tab. 2), meaning that the model indeed shows a loss-of-signal behavior. Likewise, we observed for the interference model that the

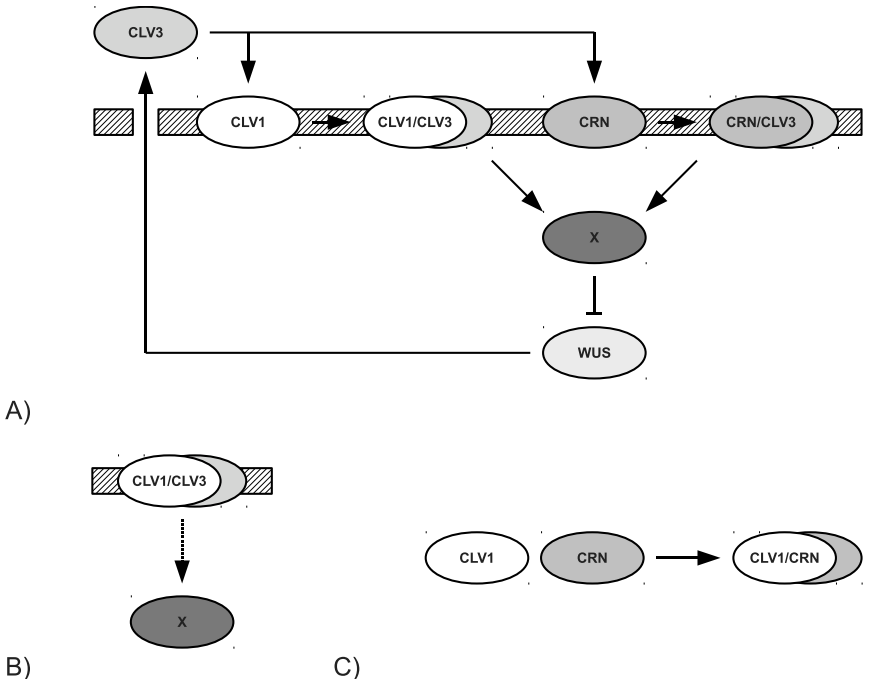

Figure 1: A) A schematic drawing of the stem cell regulation model. B-C) Schematic drawings of the two different models for the *clv1-1* mutant. B) In the loss-of-signal model the strength of the signal from the active CLV1-receptor is affected. C) In the interference model the two receptors form a complex without function.

average interference strength in the mutant (k_8) is an order of magnitude larger than the receptor turnover rates (t_1 and t_2) (Tab. 2). This simple sanity check confirmed that the hypothesized *clv1-1*-mechanisms were used by the models in the parameter sets obtained in the optimization and validation steps.

The stronger phenotype of the *clv1-1* mutant requires that the CRN pathway signal is weaker in the *clv1-1* mutant compared with the *clv1-11* null mutant. For the interference model this requirement is fulfilled by the interference mechanism itself since CRN receptors are made unavailable for binding when interfered by the mutated CLV1 in the *clv1-1* mutant.

For the loss-of-signal model it is not as obvious how the CRN pathway signal can be weaker in the *clv1-1* mutant than in the *clv1-11* null mutant, but since the *clv1-1* protein product still binds CLV3 it could sequester CLV3, making it unavailable for the CRN pathway. This would indirectly affect the signal strength of the CRN pathway. For the *clv1-11* null mutant no CLV1 is present to bind to CLV3 leading to an increase of bound CRN receptors. To verify this intuitive explanation, we investigated the amounts of free CLV3 and bound CRN receptors in the different *clv1* mutants. As expected we observed that both models had a lower amount of bound CRN receptors in the *clv1-1* mu-

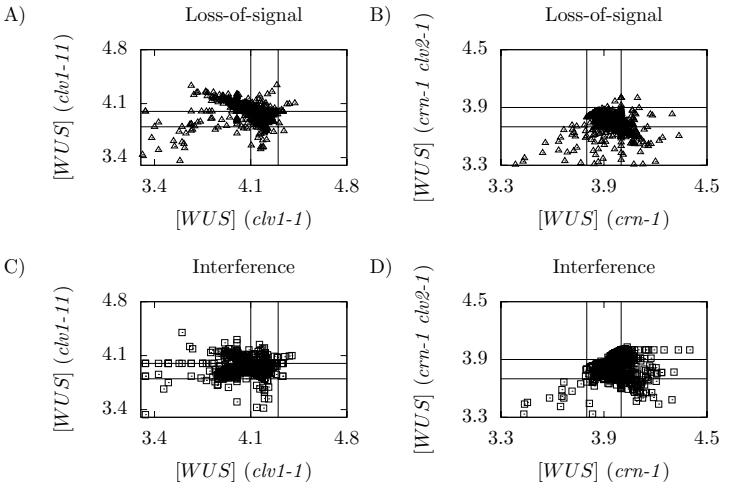

Figure 2: WUS equilibrium expressions in simulations of the *clv1-1*, *clv1-11*, *crn-1*, and *crn-1 clv2-1* single receptor mutants with the loss-of-signal (A-B) and the interference (C-D) models. Parameter sets obtained from the optimization algorithm. Solid lines mark the regions that were selected in the optimization step (Tab. 1).

tant than in the *clv1-11* null mutant (Fig. 4A and C), although the mechanisms for achieving this differed. Furthermore, the *clv1-1* loss-of-signal mutant had lower levels of free CLV3, confirming the sequestration of CLV3 (Fig. 4B). In contrast, for the interference model we observed no signs of CLV3 sequestration (Fig. 4D).

Taken together these results show that the loss-of-signal model utilizes sequestration of CLV3 in the *clv1-1* mutant in order to generate a stronger phenotype than the *clv1-11* null mutant. The interference model, on the other hand, uses interference between the receptor pathways and simulations suggest that the model is less constrained by experimental data to achieve this result (cf. Figs. 4A and C), as was also indicated by the number of parameter sets that passed the validation step for the two models.

The two clv1-1 hypotheses leads to differences in properties of the stem cell regulating network

Each model had – after the optimization and validation steps – a large ensemble of parameters. Since the wild type stem cell regulating networks of the two models are identical, there are no *a priori* reasons for the parameter values of the models – excluding the parameters unique for each implementation of the *clv1-1* mutant – to differ. To analyze differences in parameter values we generated a hypothesis-neutral background distribution by optimizing the model without using the *clv1-1* mutant. We performed 25,000 optimizations and for 24,686 parameter sets the model was able to reproduce the wild type and the three single mutant experiments. These parameter sets were used as a background parameter distribution for the two models in the proceeding analysis.

We performed a *Principal Component Analysis* (PCA) on the joint parameters of the models. Interestingly, we observed that there was a clear separation both between the distributions coming from

Mutants	Carpels/Flower	SE	Threshold error
Wild-type	2.0	0.0	-
crn-1	3.9	0.1	0.1
clv1-11	3.9	0.1	0.1
crn-1 clv2-1	3.8	0.1	0.1
clv1-1	4.2	0.1	0.1
crn-1 clv1-11	5.3	0.1	0.5
crn-1 clv1-1	4.5	0.1	0.5

Table 1: Experiments used in the optimization and validation steps to find parameter values. The first four mutants (above the line) are single-receptor mutants and are used in the optimization step. The remaining two double mutants are left for the validation step. Carpel number values and standard errors from [9]. The threshold errors are the errors used to find valid parameter sets in the optimization and validation steps.

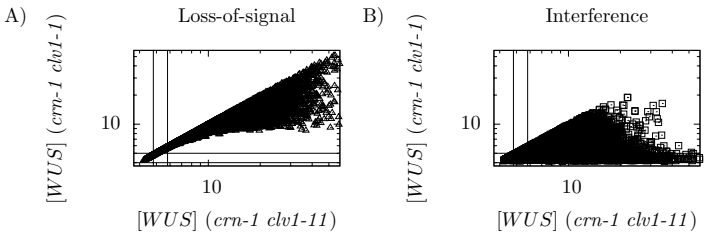

Figure 3: WUS equilibrium expressions in simulations of the *crn-1 clv1-11* and *crn-1 clv1-1* double mutants with the loss-of-signal (A) and the interference (B) models with the parameter sets obtained from the optimization step. Solid lines mark the regions that were selected in the validation step (Tab. 1).

the two models, and between those of the individual models and the background distribution (Fig. 5). This showed that the introduction of the two hypotheses for the *clv1-1* mutant leads to differences in the properties of the stem cell regulating network.

To further analyze the differences between the models we compared each parameter individually between the two models and the background by using *receiver operating characteristics* (ROC) curves. The area under the ROC-curves (AUC) quantify differences between the three parameter distributions (Methods) [24]. We generated sorted lists of the AUC values (Tab. 3), and some parameters showed differences between either *clv1-1* model and the background.

To highlight features of each model we studied the parameters that differed the most in more detail to find out how they relate to biological mechanisms. We noted that the Hill parameters (K and n) were among the top candidates for both hypotheses (Tab. 3). These parameters tune the regulation of WUS by the combined pathway (Methods). In Fig. 3 we show that the validation step did introduce large constraints on the parameters. It is likely that fitting the parameters to the double mutant experiments, led to a tighter regulation of these parameters. To confirm this, we did an AUC parameter comparison between data after the optimization step and data after the validation step, wherein both Hill parameters appeared among the top three parameters (data not shown). We also did an AUC comparison between the two models' data sets, and in this case the Hill parameters did not show up at the top of the list (data not shown). As a consequence of these results we did not look further into these two parameters, but focused on the receptor ligand dynamics.

We chose, somewhat *ad hoc*, to make a cut in

	Loss-of-signal		Interference	
Parameter	Mean value	Sensitivity	Mean value	Sensitivity
k_1	2.6 ± 2.4	-0.35 ± 0.14	1.2 ± 0.6	-0.48 ± 0.10
k_2	1.4 ± 1.0	0.12 ± 0.08	2.2 ± 1.4	0.32 ± 0.12
k_3	3.6 ± 1.5	-1.0 ± 0.10	1.7 ± 0.9	-0.85 ± 0.13
k_4	1.3 ± 0.9	-0.44 ± 0.10	1.0 ± 0.5	-0.49 ± 0.09
k_5	2.3 ± 1.4	0.33 ± 0.12	2.3 ± 1.4	0.35 ± 0.10
k_6	2.3 ± 1.2	-0.81 ± 0.08	1.8 ± 0.9	-0.77 ± 0.06
k_7	1.2 ± 0.7	0.85 ± 0.13	1.3 ± 0.8	0.91 ± 0.09
K	2.47 ± 1.17	2.5 ± 0.6	2.2 ± 0.9	2.5 ± 0.7
n	5.1 ± 1.3	-0.19 ± 0.04	4.4 ± 1.2	-0.29 ± 0.08
t_1	2.6 ± 1.2	0.61 ± 0.17	0.95 ± 0.48	0.32 ± 0.20
s_1	1.3 ± 0.7	-0.62 ± 0.11	2.3 ± 1.0	-0.69 ± 0.08
t_2	0.77 ± 0.55	0.24 ± 0.12	0.71 ± 0.36	0.21 ± 0.09
s_2	1.9 ± 0.9	-0.67 ± 0.09	2.0 ± 0.9	-0.69 ± 0.05
t_3	1.8 ± 0.9	-0.36 ± 0.21	3.9 ± 2.2	-0.15 ± 0.18
s_3	2.1 ± 1.2	-1.2 ± 0.3	1.5 ± 0.6	-1.1 ± 0.2
t_4	1.6 ± 0.8	1.8 ± 0.1	1.2 ± 0.6	1.6 ± 0.2
s_4	0.65 ± 0.33	-0.76 ± 0.51	0.76 ± 0.35	-0.87 ± 0.59
d_W	2.4 ± 2.2	-0.85 ± 0.12	2.1 ± 1.4	-0.90 ± 0.08
k_W	1.4 ± 1.0	-0.15 ± 0.13	1.3 ± 0.84	-0.088 ± 0.088
$k_{3,\text{weak}}$	0.15 ± 0.13	—	—	—
k_8	—	—	5.6 ± 4.8	—

Table 2: Model parameter properties for parameter sets remaining after the validation step. Mean value columns: Averages and standard deviations of parameter values. Sensitivity column: Averages and standard deviations of wild type WUS sensitivities (Eq. 21). (loss-of-signal 118 parameter sets, interference 531 parameter sets).

AUC at 0.75 for this analysis. The comparison between the loss-of-signal hypothesis and the background emphasized two parameters: the strength of the CLV1/CLV3 signal into the cell (k_3) and the CLV1 turnover rate (t_1) (Fig. 6A-B). The comparison between the interference hypothesis and background also highlighted two parameters, which in this case were the production rates for the two receptors (s_1, s_2) (Fig. 6C-D).

In conclusion we have shown that parameter calibration of the different implementations of the *clv1-1* mutants imposes non-expected constraints on the parameters of the respective models, and in the further analysis we found four parameters, which were the most discriminating between the models. These four parameters will be used in the proceeding analysis to evaluate their consequences in a biological perspective.

The WUS-repressing signal is dependent on both receptor pathways with a slightly stronger CLV1-dependence

The parameter that differed the most in the comparison between the loss-of-signal and background distributions was k_3 (Tab. 3), wherein it was larger for the loss-of-signal model. This is not surprising since k_3 sets the strength of the signal from the bound CLV1 receptor and the loss-of-signal mutant needs to be able to reduce this signaling strength for the *clv1-1* mutant.

The selection of k_3 may also be an indication that it is important for the loss-of-signal model that the CLV1/CLV3 pathway is stronger than the CRN/CLV3 pathway. In our implementation the strength of the former is given by k_3 times the concentration of bound CLV1 receptors, and the latter is given by k_6 times the concentration of bound CRN receptors. We observed that the CLV1 pathway indeed was slightly stronger for both models (Fig. 7)

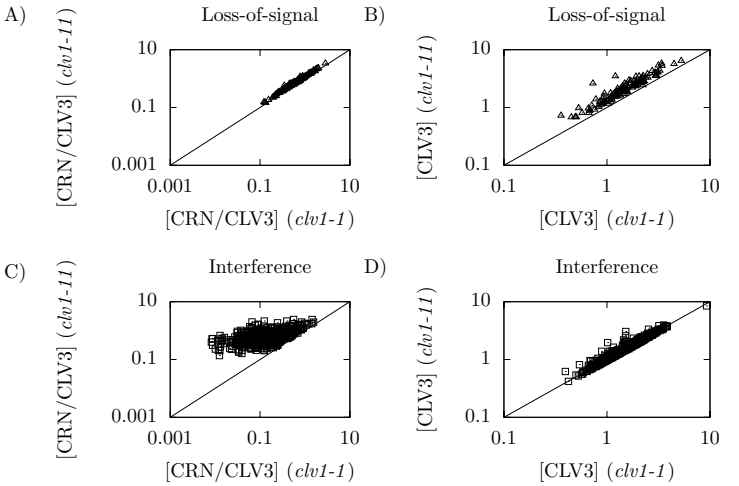

Figure 4: Equilibrium concentrations of bound CRN receptors and free CLV3 in simulations of the *clv1-1* and *clv1-11* mutants of the two models. A-B) Loss-of-signal model. C-D) Interference model. A) and C) Concentrations of bound CRN. B) and D) Concentrations of bound CLV3.

and this effect was somewhat stronger for the loss-of-signal model. However, the asymmetry between the two pathways was fairly small and it is obvious that the WUS-repressing signal is dependent on both pathways. By only considering the wild type network, one might assume that using double pathways would mean that the strengths of the two could be freely tuned: if the strength of one of the pathways is increased, the increase could be compensated by decreasing the other to obtain the same signal of the model. This was however not what we observed in our analysis. In contrast – when taking the mutants into account – the simulations showed clearly that it is important to divide the signal evenly among the two pathways, with a slight asymmetry in favor of the CLV1 pathway (Fig. 7). This is true for both models, as was also suggested by the mutant experiments since the *clv1* phenotypes are slightly stronger than the *crn* phenotypes (Tab. 1).

Degradation or internalization of the bound receptor is implicated by the loss-of-signal clv1-1 hypothesis

The second parameter highlighted for the loss-of-signal model, from the comparison with the background distribution, was t_1 (Tab. 3). The t_1 parameter sets the turnover rate of the CLV1 receptor, including the degradation of the bound receptor (Methods). The loss-of-signal model typically had a larger value of this parameter. Interestingly, this was in accordance with our finding that the loss-of-signal model without degradation of the bound CLV1 receptor cannot explain all the mutants simultaneously (data not shown). Together these results predict that for the loss-of-signal model to work the bound CLV1 receptor needs to be removed from the membrane, possibly via internalization.

Receptor trafficking has been suggested to be important for several cell-signaling pathways [25] and endosomal functions play major role in plants [26]. Although there has been no experimental evidence for CLV1 internalization, other receptors such as FSL2 and BRI have been shown to be internalized

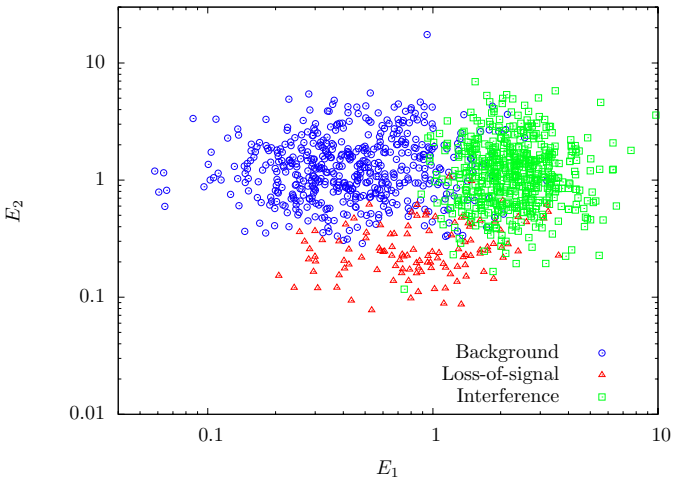

Figure 5: Parameter sets for the two models and the background distribution presented with the help of a PCA-analysis. The parameter sets are projected on the two largest principal components (E_1 and E_2).

[26]. Recent GFP-data of CLV1 indicates that CLV1 is located mainly in the plasma membrane but can also be found in internal cell compartments [10]. The model suggests that there should be a non-negligible rate of internalization of the bound CLV1 receptor.

The interference hypothesis leads to large quantities of receptors

From the comparison between the interference model and the background distribution it was seen that the parameters for receptor production, s_1 and s_2, are large in the interference model (Tab. 3). This suggests that the interference model requires large quantities of receptors to reproduce the differences in phenotype of the *clv1-1* non-null mutant and the *clv1-11* null mutant. An explanation could be that for the receptor interference mechanism to be efficient there must be enough receptors available. In Fig. 8A the amount of free receptors was compared with the amount of free CLV3 in wild type simulations and we observed that there was an abundance of receptors. It can be noted that large quantities of both receptors are present (data not shown). We also compared the background levels of receptors and CLV3, and we observed that the background distribution did not show any bias towards an abundance of free receptors (Fig. 8C).

In addition, we compared the amount of unbound versus free receptors (Figs. 8B and D), and only for the interference model did we observe a bias towards more free than bound receptors in the wild type simulations. From a biological point of view, the strategy of having large amounts of free receptors might not be advantageous given the metabolic cost associated with the production of receptors. However, the optimization algorithm does not take metabolic costs into consideration and it might be that, if it had, the result could be different. The addition of metabolic cost would be an interesting improvement of the optimization algorithm that could be tested.

At this point, we have examined all parameters highlighted by the AUC value, but our threshold value for choosing parameters to scrutinize was somewhat *ad hoc*. Hence it could be of interest to briefly look at the parameters that follow in the sorted list (Tab. 3). For the interference model the CLV3 production rate (s_3) is lower and the unbind-

Loss-of-signal vs. Background			Interference vs. Background		
Name	Relation	AUC	Name	Relation	AUC
n	LOS > Bg	0.93	n	I > Bg	0.88
k_3	LOS > Bg	0.86	K	I > Bg	0.77
K	LOS > Bg	0.84	s_1	I > Bg	0.76
t_1	LOS > Bg	0.83	s_2	I > Bg	0.75
s_2	LOS > Bg	0.70	s_3	I < Bg	0.71
k_5	LOS > Bg	0.67	k_2	I > Bg	0.67
t_4	LOS > Bg	0.66	d_W	I > Bg	0.66
k_1	LOS > Bg	0.65	k_5	I > Bg	0.66
t_3	LOS < Bg	0.64	t_3	I > Bg	0.66
s_3	LOS < Bg	0.63	t_4	I > Bg	0.61
s_4	LOS < Bg	0.61	k_W	I < Bg	0.60
d_w	LOS > Bg	0.61	k_7	I < Bg	0.58
k_7	LOS < Bg	0.58	k_4	I < Bg	0.58
k_W	LOS < Bg	0.57	s_4	I < Bg	0.57
k_2	LOS > Bg	0.57	k_1	I < Bg	0.57
k_4	LOS < Bg	0.56	k_3	I > Bg	0.56
t_2	LOS > Bg	0.56	k_6	I > Bg	0.56
k_6	LOS > Bg	0.54	t_2	I > Bg	0.54
s_1	LOS > Bg	0.51	t_1	I < Bg	0.53

Table 3: The results from the analysis step, comparing parameter value distributions of the two models with the background distribution. Parameters are sorted by area under ROC curves (AUC). The parameters under the line has a p-value greater than 0.05 and are not statistically significant, where p-values are calculated with a *Wilcoxon rank-sum test*. See also Fig. 6.

ing rate of the CLV1/CLV3 complex (k_2) is higher compared to the background distribution, acting in directions of having low CLV3 and much unbound receptor, strengthening the conclusions in this section. For the loss-of-function model the CRN production rate (s_2) and the unbinding rate of the CRN/CLV3 complex (k_5), acting in the direction of having much unbound CRN, which we could se in the simulated data (data not shown). Unbound CRN favours the possibility of sequestration of CLV3 in the *clv1-1* mutant, strengthening our sequestration discussion above.

In conclusion, our model analysis pinpointed the receptor abundance as important for both receptors in the interference model and also for the CRN receptor in the loss-of-function model. It would be interesting to see how these predictions relate to experimental data, especially the somewhat counterintuitive prediction that there is a large pool of inactivated receptors.

Additional perturbations

Although the CLV3 feedback is simplified in the model, it is of interest to analyze the model behavior for different CLV3 perturbations since these have been extensively studied in experiments. Loss-of-function *clv3* mutants show an increase in WUS expression, and gain-of-function mutants repress WUS. Simulated perturbations where CLV3 production was changed an order of magnitude up and down are presented in Fig. 9. The models correctly predicted an increase of WUS as the CLV3 was lowered and a decrease when CLV3 was increased. However, it has been shown in more detailed CLV3 perturbation experiments that it is possible to change CLV3 expression strength over a large range without any apparent phenotypical effects [27]. This was not captured in our CLV3 perturbation simulations (Fig. 9) and hence the model only qualitatively predicted the perturbations. This did not come as a surprise since we have focused our investigations on receptor mutants.

In addition, the models' robustness to param-

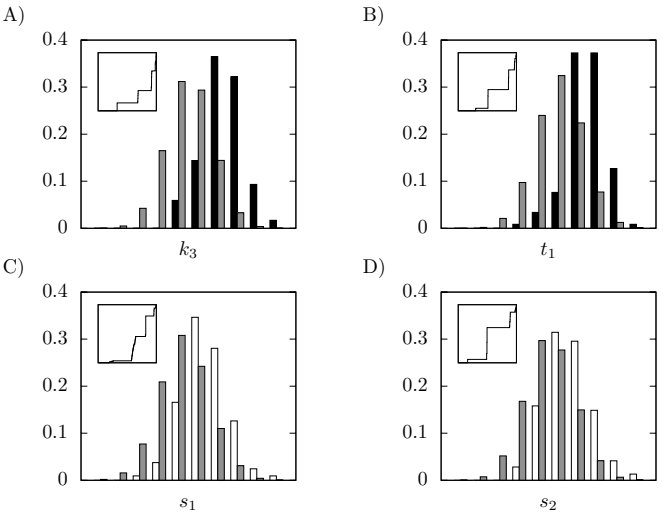

Figure 6: Distributions of parameter values of parameters highlighted in the analysis step. A-B) Comparing parameter value distributions of parameters k_3 (A) and t_1 (B) for the loss-of-signal model (black) and the background distribution (gray). C-D) Comparing parameter value distributions of parameters s_1 (C) and s_2 (D) for the interference model (white) and the background distribution (gray). Axes have log-scale and have ranges [0.23, 12] (A), [0.082, 9.9] (B), [0.24, 9.5] (C), and [0.21, 7.6] (D). Corresponding ROC-curves are presented in each plot with axes ranging from 0 to 1.0.

eter perturbations were tested. We used a sensitivity analysis to investigate the robustness of the WUS levels (Methods) and the results are presented in Tab. 2. Both models were robust to changes in most parameters, an important feature given that the stem cell regulation needs to be robust to environmental changes and stable over long periods of time. The only parameters that had a sensitivity significantly above one were K and t_4, both parts of the pathway between the signal and the WUS expression (Methods). This part of the model is a crude approximation of the internal pathway architecture. This was the second time the internal signaling pathway was highlighted (cf. n and K in Tab. 3), which indicates the importance to further investigate this part of the network, both in experiments and modeling.

Conclusions

The stem cell regulation in the plant shoot apical meristem is a well studied system given its necessity for above-ground plant development. The large amount of mutant phenotype data together with several gaps in knowledge of network details call for computational modeling as a tool for understanding the complex regulation at a systems level.

We have developed a model for the stem cell regulation based on the negative feedback loop between CLV3 and WUS and focused on CLV3-receptor dynamics and mutants. The model takes into account a negative regulation of WUS via two different – although merging – receptor pathways, CLV1 and CRN, as well as a WUS-induced CLV3 production. Starting from the question how the *clv1-11* null mutant can be weaker in phenotype compared to the non-null *clv1-1* mutant, we scrutinized two models implementing different hypothesized mechanisms for the *clv1-1* mutant.

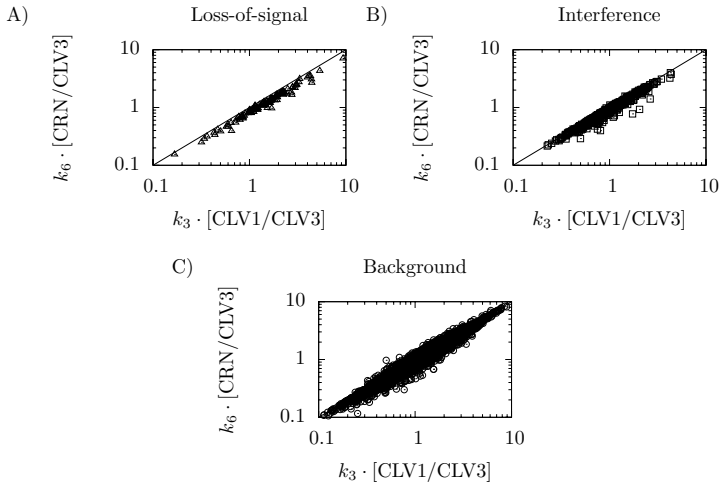

Figure 7: The parameters k_3 and k_6 set the strengths of the signals from bound CLV1 and CRN receptors. To compare the strengths of the two receptor pathways we plot each parameter multiplied with respective concentration of bound receptors. The comparison is done for the loss-of-signal model (A), the interference model (B), and the background distribution (C). Number of parameter sets for which the CRN pathway is stronger than the CLV1 pathway: Loss-of-signal - 0 (0%), Interference - 17 (3.2%), Background - 1696 (6.9%).

The first tested mechanism for *clv1-1* was that the mutated *CLV1* product interfered with the CRN pathway, as previously suggested [27]. Due to the interference, the CRN signal is decreased in the *clv1-1* mutant, as compared to the null mutant. Since both pathways are decreased the phenotype becomes stronger. We could also conclude that this hypothesis led to the prediction that there is an abundance of receptors in relation to CLV3.

In the second model the *clv1-1* mutant was implemented as a loss-of-signal mutant, i.e. the receptor still binds CLV3 but no signal is propagated. We showed that the CRN signal is decreased in the *clv1-1* mutant compared to the null mutant due to sequestration of CLV3 by the continued binding to the CLV1-receptor. For this model to work it is necessary that the bound CLV1 receptor is internalized or degraded.

We have applied a parameter inference method where the models were optimized to wild type and four different single receptor mutants and later tested against two double receptor mutants in a validation step. From 25,000 optimization runs, only a few hundred parameter sets were extracted, which showed how the method constrained the models. In addition, we generated hypothesis-neutral parameter sets by optimizing to the wild type and three single receptor mutants not including the *clv1-1* mutant. We continued our analysis with these three ensembles of parameters to get a semi-global comparison between the two models. The area under ROC-curve was used as a statistical quantification of how the two hypothesized *clv1-1* mechanisms lead to differences in parameter values, which was used to obtain the conclusions described above. The adopted approach for extracting parameter ensembles and using statistical methods when comparing different hypotheses is generally applicable for systems biology modeling and provides an objective approach for dealing with unknown parameters. A future im-

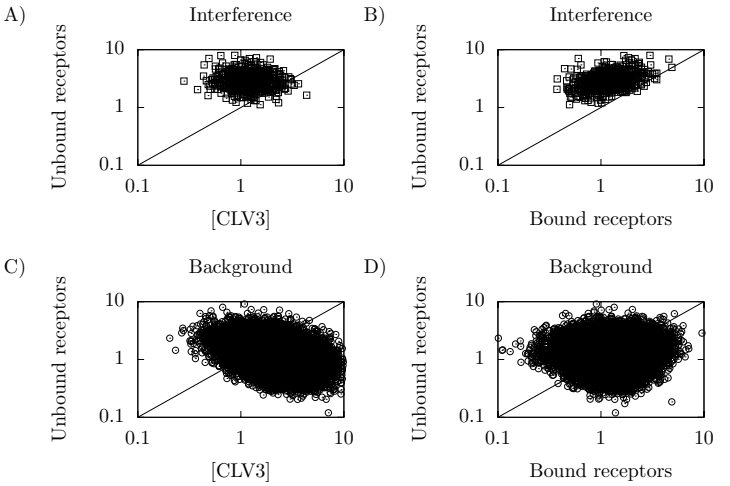

Figure 8: Study of the amount of free receptors compared with the amounts of bound receptors and free CLV3. A and C) Concentrations of free CLV3 compared with amounts of free receptors in simulations of wild-type with the interference model (A) and the background distribution (C). B and D) Amounts of bound receptors compared with amounts of free receptors in simulations of wild-type with the interference model (C) and the background distribution (D).

provement could be to adopt machine learning techniques of cross-validation by selecting different mutants to be included in the optimization and validation sets and then merge into a single parameter ensemble.

Our model represents a simplification of the system, most notably by disregarding spatial factors and not including all possible receptors known to be important for WUS regulation. However, these simplifications allowed us to investigate multiple receptors with an almost complete set of receptor mutants. We were not able to discard any of the two *clv1-1* hypotheses, but still we were able to deliver experimentally verifiable predictions for both hypotheses, also on general properties of the stem cell regulating network that are indirect consequences of the hypotheses that would have been difficult to predict by intuition alone. The loss-of-signal mechanism has the advantage that it is more parsimonious since it only affects the signaling capacity, which fits well with the allele's known mutation in the kinase domain. The interference mechanism, on the other hand, is less constrained and seems to have an easier task in producing the mutant results. In the end it is experiments that should resolve the issue and we hope that this investigation can serve as an inspiration both for new experiments and for modelers to include multiple receptors in models of plant stem cell regulation.

Methods

Models

In our models CLV3 binds to the receptors CLV1 and CRN and thereby activates them. Activated CLV1 and CRN contribute to a signal X which inhibits expression of WUS. WUS promotes production of CLV3 and therefore enables for a self-regulating system. CLV3, the receptors CLV1 and CRN, and the signal X all have a basal level of production, while WUS has basal production that can be repressed by the X signal. All molecules have a concentration-

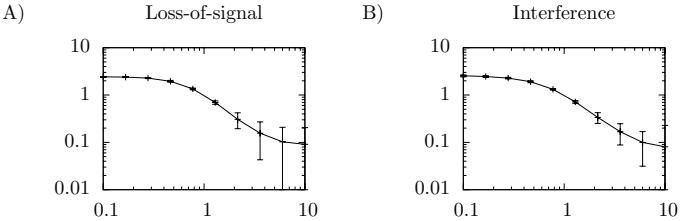

Figure 9: Study of CLV3 over- and underexpression. The parameters s_3 and k_W are multiplied by a factor (presented as the abscissa). The perturbed WUS expression is then normalized with the unperturbed WUS expression (presented as the ordinate). Presented data is average and standard deviation of normalized equilibrium WUS expressions in simulations of wild-type with the loss-of-signal model (A) and the interference model (B).

dependent degradation rate. See Fig. 1A for a schematic drawing of the wild type model. We use mass action kinetics to get a mathematical representation of the model in the form of a system of ordinary differential equations. For the wild type case the equations are

$$\frac{d[\text{CLV1}]}{dt} = t_1(s_1 - [\text{CLV1}]) - k_1[\text{CLV1}] \cdot [\text{CLV3}] + k_2[\text{CLV1/CLV3}] \quad (1)$$

$$\frac{d[\text{CRN}]}{dt} = t_2(s_2 - [\text{CRN}]) - k_4[\text{CRN}] \cdot [\text{CLV3}] + k_5[\text{CRN/CLV3}] \quad (2)$$

$$\frac{d[\text{CLV3}]}{dt} = t_3(s_3 - [\text{CLV3}]) + k_W[\text{WUS}] - k_1[\text{CLV1}] \cdot [\text{CLV3}] + k_2[\text{CLV1/CLV3}] - k_4[\text{CRN}] \cdot [\text{CLV3}] + k_5[\text{CRN/CLV3}] \quad (3)$$

$$\frac{d[\text{CLV1/CLV3}]}{dt} = k_1[\text{CLV1}] \cdot [\text{CLV3}] - k_2[\text{CLV1/CLV3}] - t_1[\text{CLV1/CLV3}] \quad (4)$$

$$\frac{d[\text{CRN/CLV3}]}{dt} = k_4[\text{CRN}] \cdot [\text{CLV3}] - k_5[\text{CRN/CLV3}] - t_2[\text{CRN/CLV3}] \quad (5)$$

$$\frac{d[\text{X}]}{dt} = t_4(s_4 - [\text{X}]) + k_3[\text{CLV1/CLV3}] + k_6[\text{CRN/CLV3}] \quad (6)$$

$$\frac{d[\text{WUS}]}{dt} = k_7 \frac{K^n}{K^n + [\text{X}]^n} - d_W[\text{WUS}], \quad (7)$$

where [CLV1] and [CRN] are concentrations of unbound receptors, [CLV3] is the concentration of the CLV3 peptide, [CLV1/CLV3] and [CRN/CLV3] are concentrations of bound receptors, [X] is the concentration of the signal X, and [WUS] is the concentration of the transcription factor WUS.

The parameters k_1, k_2, k_4, and k_5 are reaction constants for binding of CLV3 to CLV1 and CRN. The parameters k_3 and k_6 set the strengths of the signals from the activated receptors to the signal X. Production and degradation of CLV1, CRN, CLV3, and X are determined by the parameters t_1, s_1, t_2, s_2, t_3, s_3, t_4, and s_4, while d_w sets degradation of WUS. Production of WUS, downregulated by X, is controlled by parameters k_7, K, and n. Note that we do not have experimental estimates of parameter values and it is mainly the relation between parameters that is of importance; hence we refrain from specifying unit values on our parameters.

Our model is to be seen as a simplification of the SAM. The SAM is divided into several spatial regions each characterized by different gene expression patterns. Cells in the SAM also divide with

time and move between different regions. We do not address the positioning associated with the different expression domains. While WUS, CLV1, and CRN are expressed in the same cells, CLV3 is not [2, 3]. We include a simplified CLV3 feedback via a direct connection from WUS and a direct binding of CLV3 to the receptors. The rationale for this simplification is that the way the spatial signals are propagated is not fully understood and would require adding multiple additional hypotheses (see e.g. [18, 19]). Our implementation still covers the main feedback interactions needed to investigate the behavior of the different receptor mutants that are the main target of this work. The internal part of the signaling pathway is in our model described by a single signal X. Although the POL/PLL1 has been shown to be important for mediating the signal [14], the details of the architecture is unknown and we point this out by instead representing the signal with X.

The state of the CLV signaling network is in our model measured via the WUS expression levels. In the plant, WUS and CLV3 are known to be altered when the CLV signaling is perturbed, both by an expanding/decreasing expression region and in an increase/decrease in levels [15], and our WUS measure serves as a simplification of this.

Mutants

We are interested in several receptor mutants and we implement them in different ways. The *clv1-11* and *crn-1 clv2-1* mutants are both modeled by removing all presence of CLV1 ($[\text{CLV1}] = [\text{CLV1/CLV3}] = 0$) and CRN ($[\text{CRN}] = [\text{CRN/CLV3}] = 0$) respectively. The *crn-1* mutant is modeled by setting $k_6 = 0$. The remaining mutant of interest – *clv1-1* – is treated differently in two models.

In the loss-of-signal model the parameter k_3 is replaced by another parameter $k_{3,\text{weak}}$ for the *clv1-1* mutant (Fig. 1B).

In the interference model an extra mechanism is introduced (Fig. 1C). For the *clv1-1* mutant, the receptors CLV1 and CRN can form a complex and when they do the complex is discarded. Mathematically an extra term is added to the time derivative of CLV1 and CRN,

$$\frac{d[\text{CLV1}]}{dt} = \ldots - k_8[\text{CLV1}] \cdot [\text{CRN}] \quad (8)$$

$$\frac{d[\text{CRN}]}{dt} = \cdots - k_8[\text{CLV1}] \cdot [\text{CRN}]. \quad (9)$$

Computational Procedures

Our approach can be divided into three steps; an optimization step, a validation step, and an analysis step. In the optimization step we use an optimization algorithm to find parameter (value) sets for which the models can reproduce the wild type and the four loss-of-function mutants. In the validation step we choose the subset of these parameter sets for which the models also explain the two double mutants. In this way we are reducing the problem of overfitting to data, which usally hampers the predictive power of the models.

After the validation step a large number of possible parameter sets remain. Instead of the more usual approach of just choosing the parameter set for which the model best matches experimental data, we keep all parameters and look at the ensemble-output of the model. In this way we get semi-global robust predictions of the model behavior. However, this leaves us with lots of possible parameter sets which require further analysis. In the analysis step of our computational approach we deploy a number of computational and statistical tools to analyze the ensemble of obtained parameter sets. In this way we are trying to further analyze the behavior of the models to find significant differences.

Optimization

A Simulated annealing algorithm was used to fit parameters to experimental data [28]. The algorithm is divided into four steps.

1. An initial set of parameters, p_{initial}, is randomly chosen from a uniform distribution.

2. A proposed new set of parameters p_{new} is chosen by randomly picking a parameter and changing its value by – with equal probability – multiplying or dividing with a factor 1.01. An associated energy is calculated by a parameter-dependent energy (objective) function $E = E(p)$ (see below).

3. The new parameter set p_{new} is kept with a probability $P = \min(1, e^{-\beta(E(p_{\text{new}})-E(p_{\text{old}}))})$, where β is a positive parameter inversely proportional to a virtual temperature.

4. Step 2-3 is repeated while β is being increased every thousand iterations by a factor 1.1, starting from 1 until it ends at 10,000.

For every iteration, the energy associated with the current parameter set is compared to the overall best performing parameter set, i.e. the parameter set with the lowest corresponding energy. When β reaches its maximum value the algorithm stops and the best performing parameter set is used as the solution to the optimization problem.

Each optimization gives a proposed parameter set. After each optimization the parameter set is tested with the model against the experimental data. If the model is able to reproduce the experimental data within the errors supplied the parameter set is kept, otherwise it is discarded.

Energy function

To compare phenotypic strength between models and experiments, we use WUS levels as a measure in the models and compare with carpel numbers from experiments. Carpel numbers have been used extensively in the literature as a measure of the phenotypic strength of perturbations to the CLV signaling network (see e.g. [9, 16], and [20] for an example where both RT-PCR measurements of WUS and carpel numbers are reported).

To calculate the energy for a given parameter set we first calculate the equilibrium of WUS concentration, $[\text{WUS}]^*$, for the wild type experiment, and for the *crn-1*, *clv1-11*, *crn-1 clv2-1*, and *clv1-1* mutant experiments. The WUS levels for the mutant experiments are normalized with the wild type WUS level. The energy function is defined as

$$E = \sum_i \left([\text{WUS}_i]^* - D_i\right)^2, \tag{10}$$

where $[\text{WUS}_i]^*$ is the normalized equilibrium WUS expression for experiment i, D_i is the expected value from experiment, and the summation is over all mutant experiments. The experimental values that we have used to find parameters are presented in Tab. 1 [9].

Validation

To reduce overfitting we leave two double mutant experiments out of the optimization step and instead use them for a validation step. Simulations of two double mutants *crn-1 clv1-11* and *crn-1 clv1-1* for the two models are compared with experimental data to find parameters that can be used to reproduce the behavior of both the single and double mutant experiments. In the validation step we use a larger threshold for validating simulations compared to what was used in the optimization step (Tab. 1).

Numerical solutions

We are interested in fixed point solutions to the system, which are obtained by solving the system of equations when all time derivatives are equal to zero. At equilibrium the fixed point concentrations $[\text{X}]^*$, $[\text{CLV1/CLV3}]^*$, and $[\text{CRN/CLV3}]^*$ are equal to

$$[\text{X}]^* = s_4 + \frac{k_3[\text{CLV1/CLV3}]^* + k_6[\text{CRN/CLV3}]^*}{t_4}, \tag{11}$$

$$[\text{CLV1/CLV3}]^* = \frac{k_1}{k_2 + t_1}[\text{CLV1}]^* \cdot [\text{CLV3}]^*, \tag{12}$$

$$[\text{CRN/CLV3}]^* = \frac{k_4}{k_5 + t_2}[\text{CRN}]^* \cdot [\text{CLV3}]^*. \tag{13}$$

The three fixed point concentrations $[\text{CLV1}]^*$, $[\text{CRN}]^*$, and $[\text{CLV3}]^*$ are given by the solution to the system of equations

$$\begin{aligned} 0 =& t_1(s_1 - [\text{CLV1}]^*) - b_1[\text{CLV1}]^* \cdot [\text{CLV3}]^* \\ & - k_8[\text{CLV1}]^* \cdot [\text{CRN}]^*, \end{aligned} \tag{14}$$

$$\begin{aligned} 0 =& t_2(s_2 - [\text{CRN}]^*) - b_2[\text{CRN}]^* \cdot [\text{CLV3}]^* \\ & - k_8[\text{CLV1}]^* \cdot [\text{CRN}]^*, \end{aligned} \tag{15}$$

$$\begin{aligned} 0 =& t_3(s_3 - [\text{CLV3}]^*) - b_1[\text{CLV1}]^* \cdot [\text{CLV3}]^* \\ & - b_2[\text{CRN}]^* \cdot [\text{CLV3}]^* + k_W[\text{WUS}]^*, \end{aligned} \tag{16}$$

with $k_8 \neq 0$ for the *clv1-1* mutant in the interference model and $k_8 = 0$ otherwise, and where

$$b_1 = \frac{t_1 k_1}{k_2 + t_1} \quad \text{and} \quad b_2 = \frac{t_2 k_4}{k_5 + t_2}. \tag{17}$$

The equilibrium expression of WUS, $[\text{WUS}]^*$, is the solution to

$$k_7 \frac{K^n}{K^n + [\text{X}]^{*n}} - d_W[\text{WUS}]^* = 0, \tag{18}$$

To numerically find the equilibrium concentrations we first consider Eq. 18 as a function f of WUS expression

$$f([\mathrm{WUS}]) = k_7 \frac{K^n}{K^n + \mathrm{X}^*([\mathrm{WUS}])^n} - d_W[\mathrm{WUS}], \tag{19}$$

where $X^* = X^*([\mathrm{WUS}])$ is a function of WUS given by Eqs. 11-16. The equation $f([\mathrm{WUS}]) = 0$ is solved numerically by the bisection method [28]. As an intermediate step we solve the system of equations, Eqs. 14-16, with Newton's method [28]. We define equilibrium as follows; the Newton's method iterates until $|\mathbf{e}| < 0.001$, where

$$\mathbf{e} = \left(\frac{d[\mathrm{CLV1}]}{dt}, \frac{d[\mathrm{CRN}]}{dt}, \frac{d[\mathrm{CLV3}]}{dt} \right), \tag{20}$$

and the bisection method iterates until $|f([\mathrm{WUS}])| < 0.0001$.

Sensitivity analysis

The models' robustness to parameter perturbations were tested by a sensitivity analysis [29]. If M is a quantity of the system and p is a parameter, the sensitivity S_p is defined as

$$S_p = \frac{\partial M}{\partial p} \frac{p}{M}. \tag{21}$$

The absolute value of S_p serves as a measurement of how sensitive M is to perturbations in parameter p. A greater value corresponds to a greater sensitivity. The sign of S_p tells if the response is positive or negative in respect to a positive change of the parameter. We use the equilibrium WUS concentration for the wild type network for our measurable quantity during our sensitivity analysis.

Receiver under chacteristic curves

A receiver under characteristic (ROC) curve measures the overlap of the distributions of two data sets A and B. The area under the ROC-curves (AUC) quantify differences between A and B independent of the number of parameter sets within the distributions. By calculating the AUC we get a value between 0 and 1, where 0 means that the values of data set A are all greater than those of data set B, 0.5 means that the two sets come from the same distribution, and 1 means that all values of data set B are greater than those of data set A [24].

Implementation and data set

The optimization algorithm, the numerical solver, and the statistical tools are in house implementations and are publicly available upon request. Parameter data can be found at `http://www.thep.lu.se/~henrik/clvCrn/`.

Author contributions

All authors designed experiments. PS and PM implemented and applied simulation and analysis tools. All authors analyzed data. All authors wrote the paper.

Acknowledgements

We are grateful for valuable discussions with Patrik Edén, Pawel Krupinski, Elliot Meyerowitz, and Eric Mjolsness. This work was in part supported by The Swedish Research Council.

References

1. Scheres B: **Stem-cell niches: nursery rhymes across kingdoms**. *Nat Rev Mol Cell Biol* 2007, **8**(5):345–54.
2. Sablowski R: **The dynamic plant stem cell niches**. *Curr Opin Plant Biol* 2007, **10**(6):639–44.
3. Bleckmann A, Simon R: **Interdomain signaling in stem cell maintenance of plant shoot meristems**. *Mol Cells* 2009, **27**(6):615–20.
4. Schoof H, Lenhard M, Haecker A, Mayer KF, Jürgens G, Laux T: **The stem cell population of Arabidopsis shoot meristems in maintained by a regulatory loop between the CLAVATA and WUSCHEL genes**. *Cell* 2000, **100**(6):635–44.
5. Fletcher JC, Brand U, Running MP, Simon R, Meyerowitz EM: **Signaling of cell fate decisions by CLAVATA3 in Arabidopsis shoot meristems**. *Science* 1999, **283**(5409):1911–4.
6. Brand U, Fletcher JC, Hobe M, Meyerowitz EM, Simon R: **Dependence of stem cell fate in Arabidopsis on a feedback loop regulated by CLV3 activity**. *Science* 2000, **289**(5479):617–9.
7. Ogawa M, Shinohara H, Sakagami Y, Matsubayashi Y: **Arabidopsis CLV3 peptide directly binds CLV1 ectodomain**. *Science* 2008, **319**(5861):294.
8. Jeong S, Trotochaud AE, Clark SE: **The Arabidopsis CLAVATA2 gene encodes a receptor-like protein required for the stability of the CLAVATA1 receptor-like kinase**. *Plant Cell* 1999, **11**(10):1925–34.
9. Müller R, Bleckmann A, Simon R: **The receptor kinase CORYNE of Arabidopsis transmits the stem cell-limiting signal CLAVATA3 independently of CLAVATA1**. *Plant Cell* 2008, **20**(4):934–46.

10. Bleckmann A, Weidtkamp-Peters S, Seidel C, Simon R: **Stem cell signalling in Arabidopsis requires CRN to localize CLV2 to the plasma membrane**. *Plant Physiol* 2010, **152**:166–76.

11. DeYoung BJ, Bickle KL, Schrage KJ, Muskett P, Patel K, Clark SE: **The CLAVATA1-related BAM1, BAM2 and BAM3 receptor kinase-like proteins are required for meristem function in Arabidopsis**. *Plant J* 2006, **45**:1–16.

12. DeYoung BJ, Clark SE: **BAM receptors regulate stem cell specification and organ development through complex interactions with CLAVATA signaling**. *Genetics* 2008, **180**(2):895–904.

13. Miwa H, Kinoshita A, Fukuda H, Sawa S: **Plant meristems: CLAVATA3/ESR-related signaling in the shoot apical meristem and the root apical meristem**. *J Plant Res* 2009, **122**:31–9.

14. Song SK, Lee MM, Clark SE: **POL and PLL1 phosphatases are CLAVATA1 signaling intermediates required for Arabidopsis shoot and floral stem cells**. *Development* 2006, **133**(23):4691–8.

15. Reddy GV, Meyerowitz EM: **Stem-cell homeostasis and growth dynamics can be uncoupled in the Arabidopsis shoot apex**. *Science* 2005, **310**(5748):663–7.

16. Diévart A, Dalal M, Tax FE, Lacey AD, Huttly A, Li J, Clark SE: **CLAVATA1 dominant-negative alleles reveal functional overlap between multiple receptor kinases that regulate meristem and organ development**. *Plant Cell* 2003, **15**(5):1198–211.

17. Jönsson H, Krupinski P: **Modeling plant growth and pattern formation**. *Curr Opin Plant Biol* 2010, **13**:5—11.

18. Jönsson H, Shapiro B, Meyerowitz E, Mjolsness E: **Signaling in multicellular models of plant development**. In *On Growth, Form and Computers*. Edited by Kumar S, Bentley P, London: Academic Press 2003:156–161.

19. Jönsson H, Heisler M, Reddy GV, Agrawal V, Gor V, Shapiro BE, Mjolsness E, Meyerowitz EM: **Modeling the organization of the WUSCHEL expression domain in the shoot apical meristem**. *Bioinformatics* 2005, **21 Suppl 1**:i232–40.

20. Gordon SP, Chickarmane VS, Ohno C, Meyerowitz EM: **Multiple feedback loops through cytokinin signaling control stem cell number within the Arabidopsis shoot meristem**. *Proc Natl Acad Sci USA* 2009, **106**(38):16529–34.

21. Geier F, Lohmann JU, Gerstung M, Maier AT, Timmer J, Fleck C: **A quantitative and dynamic model for plant stem cell regulation**. *PLoS ONE* 2008, **3**(10):e3553.

22. Melke P, Jönsson H, Pardali E, ten Dijke P, Peterson C: **A rate equation approach to elucidate the kinetics and robustness of the TGF-beta pathway**. *Biophys J* 2006, **91**(12):4368–80.

23. Kirkpatrick S, Gelatt C, Vecchi M: **Optimization by Simulated Annealing**. *Science* 1983, **220**(4598):671–680.

24. Hanley JA, McNeil BJ: **The meaning and use of the area under a receiver operating characteristic (ROC) curve**. *Radiology* 1982, **143**:29–36.

25. Vilar JMG, Jansen R, Sander C: **Signal processing in the TGF-beta superfamily ligand-receptor network**. *PLoS Comput Biol* 2006, **2**:e3.

26. Otegui MS, Spitzer C: **Endosomal functions in plants**. *Traffic* 2008, **9**(10):1589–98.

27. Müller R, Borghi L, Kwiatkowska D, Laufs P, Simon R: **Dynamic and compensatory responses of Arabidopsis shoot and floral meristems to CLV3 signaling**. *Plant Cell* 2006, **18**(5):1188–98.

28. Press WH, Teukolsky SA, Vetterling WT, Flannery BP: *Numerical recipes: the art of scientific computing*. Cambridge University Press, NY, third edition 2007.

29. Savageau MA: **Parameter sensitivity as a criterion for evaluating and comparing the performance of biochemical systems**. *Nature* 1971, **229**(5286):542–4.

Paper II

Developmental Patterning by Mechanical Signals in *Arabidopsis*

Olivier Hamant,[1,2]* Marcus G. Heisler,[3]* Henrik Jönsson,[4]* Pawel Krupinski,[4] Magalie Uyttewaal,[1,2] Plamen Bokov,[5,6] Francis Corson,[5] Patrik Sahlin,[4] Arezki Boudaoud,[5] Elliot M. Meyerowitz,[3]† Yves Couder,[6]† Jan Traas[1,2]†

A central question in developmental biology is whether and how mechanical forces serve as cues for cellular behavior and thereby regulate morphogenesis. We found that morphogenesis at the *Arabidopsis* shoot apex depends on the microtubule cytoskeleton, which in turn is regulated by mechanical stress. A combination of experiments and modeling shows that a feedback loop encompassing tissue morphology, stress patterns, and microtubule-mediated cellular properties is sufficient to account for the coordinated patterns of microtubule arrays observed in epidermal cells, as well as for patterns of apical morphogenesis.

The surface layers of plant tissues are under considerable tension (*1*). This results from the fact that individual cells, including those in deeper layers, are tightly bound to each other through their cellulosic walls, on which they exert turgor pressure (*2*). In addition, plant cell walls resist stress (force per unit area) differentially, depending on the direction of stress (*3*). This anisotropy is a consequence of the direction in which the rigid cellulose microfibrils are laid down during wall synthesis (*4*). Because this direction is often parallel to the cortical microtubules of the plant cell, it is thought that the microtubules might serve as tracks along which the cellulose synthase complexes travel (*5*, *6*). Green and others have proposed that cortical microtubule orientations correlate with anisotropic stresses, but the existence of such a causal link with morphogenesis has never been further investigated (*7*–*11*). We have chosen to dissect this link in shoot apical meristems, a population of stem cells that continuously generate aerial organs while undergoing complex shape transformations (*12*, *13*) (fig. S1).

Morphogenetic role of the microtubules at the shoot apex. To assess the functional importance of microtubules within the *Arabidopsis* meristem, we depolymerized the microtubules with the use of oryzalin and monitored the resulting cell morphology (*14*). In the absence of microtubules, the meristems kept growing but no cytokinesis occurred, and giant polyploid cells formed (Fig. 1A) (*14*). Despite these changes, differentiation and patterning were not drastically affected. We observed slow-growing cells in the meristem and fast-growing cells in the primordia, and phyllotaxis was not altered 46 hours after complete depolymerization of microtubules (Fig. 1B and fig. S2). Cell identity in the boundary domain between the meristem and new floral primordia did not seem to be altered, as a boundary domain reporter, *pBOUND-GFP*, was induced in this domain several days after the treatment (Fig. 1C and fig. S2).

However, depolymerization of the microtubules resulted in a distinct change in the geometry of the cells. The final structure resembled two-dimensional (2D) foams, which are purely isotropic in nature. Notably, all the walls met at angles of 120° and the curvature of the walls approached that of a soap-bubble network (Fig. 1A) (*15*, *16*). In addition, certain morphogenetic events did not occur. In particular, the crease between the meristem and primordia no longer formed (Fig. 1, B to D, and fig. S2). Hence, although microtubules may not be critical for developmental patterns such as phyllotaxis, they are required for certain morphogenetic events such as tissue folding.

In the presence of oryzalin, organ outgrowth was still observed, which suggests that plant shape is at least partially independent of microtubule-based anisotropy. Because growth patterns are thought to depend largely on the plant hormone auxin (*17*–*21*), we next used a double drug treatment where both microtubules and auxin transport were inhibited. This led to the formation of a spherical shoot tip (fig. S3A) (*14*), as might be expected if microtubule-controlled anisotropy operates in parallel with auxin-driven growth rate patterns.

Cortical microtubule orientations and dynamics are correlated with morphogenesis. To further analyze the role of microtubules in morphogenesis, we investigated microtubule dynamics in the meristem via live imaging of plants expressing green fluorescent protein (GFP) fused to the microtubule-binding domain (MBD) of microtubule-associated protein 4 MAP4 (*22*, *23*). A quantitative analysis of the cortical microtubules at the surface of more than 30 meristems revealed three aspects of microtubular arrays:

1) The microtubules at the meristem summit were highly dynamic, constantly changing their orientation at 1- to 2-hour intervals (Fig. 2, A to C, and movie S1) (*24*, *25*).

2) At the periphery and base of the meristem, orthoradial (circumferential) cortical microtubule arrays were dominant. This orientation was more apparent when organ initiation was inhibited in the presence of the auxin transport inhibitor *N*-1-naphthylphthalamic acid (NPA) and seemed to be the default orientation at the periphery in the absence of floral primordia (fig. S4).

3) As flower primordia started to grow out, a supracellular alignment of microtubules along the boundary between the meristem and the primordium appeared (Fig. 2, A and B, and fig. S4). This configuration was stably maintained over prolonged periods (up to 20 hours). Consistent with these highly ordered and stable interphase arrays, about 90% of the cells (n = 158, eight meristems) in this zone displayed preprophase bands and division planes in the same tangential orientation. Microtubules were aligned during the activation of *pFIL::dsRED-N7* (*18*), a late marker of floral primordium initiation, showing that the alignment accompanies flower outgrowth (Fig. 2D).

Microtubule orientations align along predicted principal stresses. In a multicellular setting, the field of physical forces represents a potential source of information for the cells to know their relative position (*7*, *26*–*30*). Several studies have supported the proposal that maximal stress directions orient cortical microtubules, most probably via a response to strain in the cell wall (*8*, *10*, *31*–*33*). However, these studies do not address the link with morphogenesis. In addition, it remains difficult to test the plausibility of such a hypothesis in a tissue context. We therefore used a combination of physical and mathematical approaches to address these issues.

To assess whether stresses might orient microtubules, we first calculated the expected pattern of stresses at the shoot apical meristem surface by considering the apex at the tissue scale. Our mechanical model of the meristem as a pressure vessel—a shell inflated by an inner pressure—depends on the following assumptions: (i) The tissue is elastic [(*34*, *35*) and our results], (ii) the outer wall of the epidermal layer supports the turgor pressure and acts as a limiting factor for growth (*36*, *37*), and (iii) the outer wall of the epidermal layer is under a uniform pressure from the inside (*34*). Using these properties, we calculated the directions of principal stresses in different domains of the shoot apex and found that they are parallel to the observed cortical microtubule orientations (Fig. 3, A and B).

[1]INRA, Laboratoire de Reproduction et Développement des Plantes, 46 Allée d'Italie, 69364 Lyon Cedex 07, France. [2]Université de Lyon, CNRS, ENS, 46 Allée d'Italie, 69364 Lyon Cedex 07, France. [3]Division of Biology, California Institute of Technology, Pasadena, CA 91125, USA. [4]Computational Biology and Biological Physics Group, Department of Theoretical Physics, Lund University, S-221 00 Lund, Sweden. [5]Laboratoire de Physique Statistique, Ecole Normale Supérieure, 24 rue Lhomond, 75231 Paris Cedex 05, France. [6]Matière et Systèmes Complexes, Université Paris-Diderot, 10 rue Alice Domont et Léonie Duquet, 75025 Paris Cedex 13, France.

*These authors contributed equally to this work.

†To whom correspondence should be addressed. E-mail: jan.traas@ens-lyon.fr (J.T.); meyerow@caltech.edu (E.M.M.); couder@lps.ens.fr (Y.C.)

To further investigate the correlation between predicted stresses and microtubule orientations, we designed a 3D cell- and wall-based tissue model representing the surface of the L1 layer of the shoot and incorporating the three assumptions listed above. The model includes mechanisms such as elastic wall mechanics, wall growth, cellular mechanical anisotropy (microfibrils), stress feedback, and growth and proliferation (fig. S5, A and B) (*38*). Mechanical anisotropy is introduced by defining a microtubule direction within each 2D cell where the stiffness of the wall material increases as the wall becomes more parallel to the direction of the cortical microtubules. Stress feedback is introduced by updating the microtubule directions to align along maximal stress directions, which for one cell is measured by the directional weighted average of its wall stresses. Note that strengthening of the walls (by aligning microfibrils) counteracts the main stress intensity but maintains the main stress direction.

The model faithfully reproduced the orthoradial and random microtubule alignments on synthetic templates of the stem and tip of a dome, respectively, and predicted alignment along the crease for a saddle-shaped template (fig. S6). Simulated microtubule directions in a template extracted from a confocal data set also predicted the experimentally seen boundary alignment zone as well as the more random microtubule orientations at the apex (Fig. 3C). A growth model was then introduced to examine microtubule orientations during morphogenetic events, including primordium growth and tip growth (*38*). Primordium growth was initiated by locally decreasing wall stiffness, leading to the outgrowth of a well-defined bump. As the simulated primordium formed, the model also predicted an orthoradial microtubule alignment as observed in the region between the meristem and the primordium (Fig. 3D and movie S2) as well as around the simulated primordium, thus reproducing the alignment zone between the meristem and the primordium. Growth of the meristem and stem was simulated by implementing growth at a rate that was depen-

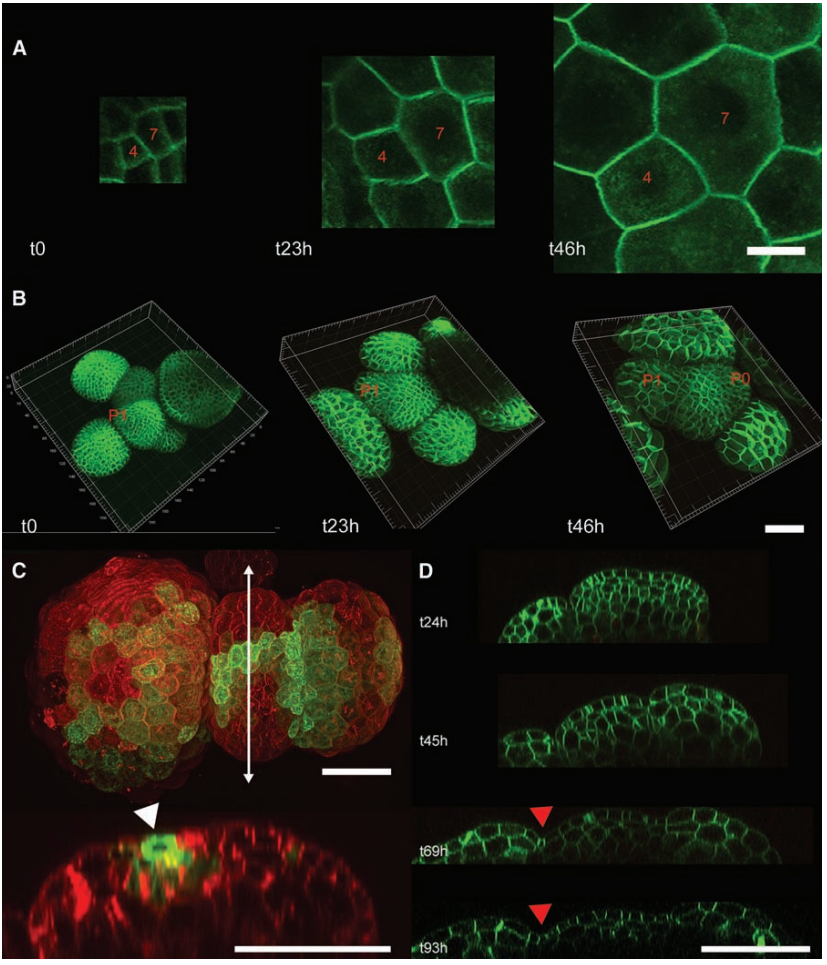

Fig. 1. Morphogenetic role of the microtubules. (**A**) Effect of oryzalin treatment on cell shape. Walls tend to meet at 120° and become convex or concave in cells with less or more than six walls, respectively, as observed in a 2D foam. Numbers of walls are in red. Scale bar, 10 μm. (**B**) Three-dimensional reconstructions of *GFP-LTI6b* meristems treated with oryzalin immediately after the treatment (t0) and 23 and 46 hours later. Note the absence of a crease at P1 and the position of P0 following the expected phyllotactic pattern. Scale bar, 50 μm. (**C**) *pBOUND-GFP* (green) expression 3 days after the first oryzalin treatment, in the absence of a crease (arrowhead), in a meristem stained with the fluorescent lipophilic dye FM4-64 (red). Scale bars, 50 μm. (**D**) Longitudinal optical sections of an existing crease being flattened over time after oryzalin treatment (red arrowhead). Scale bar, 50 μm.

dent on the distance to the apex (Fig. 3E and movie S3) (*39*). In these simulations, the microtubule orientations were unstable at the apex while the orientations on the stem stabilized in a mainly orthoradial pattern, as was observed. Finally, we tested whether the model could also predict the effects of oryzalin treatment, simulated by removing the anisotropic contribution to wall mechanics. Both a loss of the crease in the experimental template and ballooning of cells in a pin-shaped growth simulation were qualitatively predicted (fig. S3, B and C).

Cell ablation results in characteristic microtubule reorientations. The results so far suggest a scenario where the alignment of microtubules to maximal stress directions modifies the orientation of newly deposited cellulose microfibrils, thereby regulating morphogenesis. We next tested this scenario experimentally.

We began with a laser ablation approach. We reasoned that by killing cells and thereby locally eliminating turgor pressure and weakening cell walls, we could induce characteristic changes in stress and strain patterns. To obtain theoretical predictions for the resultant stress patterns due to laser ablation, we used the finite-element method (FEM) to model the L1 layer of meristem cells (*38*). The ablation is simulated as a loss of turgor as well as diminution of elastic properties of the walls of the ablated cells (fig. S5C) (*38*).

The simulation predicts rearrangement of principal stress directions during ablation. Before the removal of the cell, the principal stress patterns depend more on the geometry of each individual cell than on the relationship between cells (Fig. 4A, left). Assuming that the top wall is intact at $t = 0$ hours and gradually weakens afterward, our modeling predicted the maximal stress direction (hence the microtubule orientations) initially to be radial and then to become circumferential with respect to the wound (Fig. 4A).

We used a laser to target cells within the central zone of the meristem, where observed cortical microtubule alignments and growth patterns suggest that cell walls are largely mechanically isotropic. Time-lapse analysis of cells surrounding an ablation site showed a slight initial expansion of surrounding cells into the wound during the first 1.5 hours after laser treatment, consistent with a sudden imbalance in stresses due to loss of turgor in the dead cell or cells (Fig. 4B and movie S4). During this time, no significant microtubule reorientation was detected. However, starting at 1.5 hours and continuing to about 5.5 hours after ablation, we subsequently observed microtubule orientations to align circumferentially (Fig. 4B and movie S4). These results match the predictions of our model and are also consistent with previous reports of circumferential microtubule rearrangements in response to wounding (*40*, *41*). The absence of an initial radial alignment suggests that the initial stresses associated with radial expansion are too transient to trigger a response.

Although these results support our hypothesis, several alternative hypotheses could not be excluded at this stage. For instance, it is possible that the microtubules may be reorienting perpendicular to the observed initial cell deformations, contrary to our stress alignment proposal. However, because the realignment occurs hours after the initial radial deformation is initiated, this possibility seems less likely. Another hypothesis is that the microtubules may not be responding to mechanical stress but rather to unrelated biochemical wound signals. To test this last scenario, we first proceeded with ablations in the boundary domain. We reasoned that local diffusion of a biochemical signal in this domain and in the central zone should be roughly similar, whereas in the boundary the stress field generated by the ablation should be in competition with the strong tangential stress at the crease (fig. S7, A and B). In contrast to central zone ablations, ablations in boundary regions resulted in a lack of microtubule reorientation in neighboring cells, or a delay of reorientation lasting 7.5 hours or more in some cases. In most cases (five of six experiments), we could find at least one cell with no circumferential microtubule orientation 7.5 hours after ablation, and in two cases, no reorientations

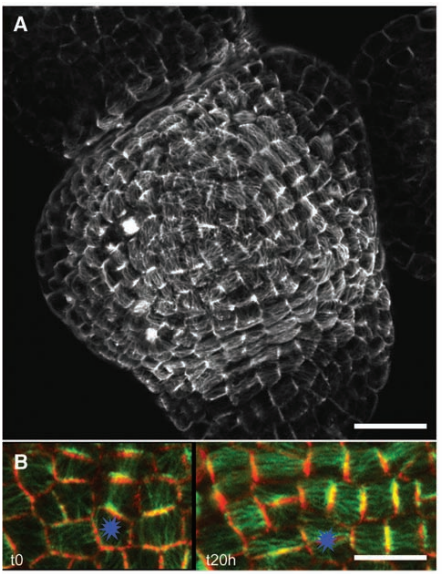

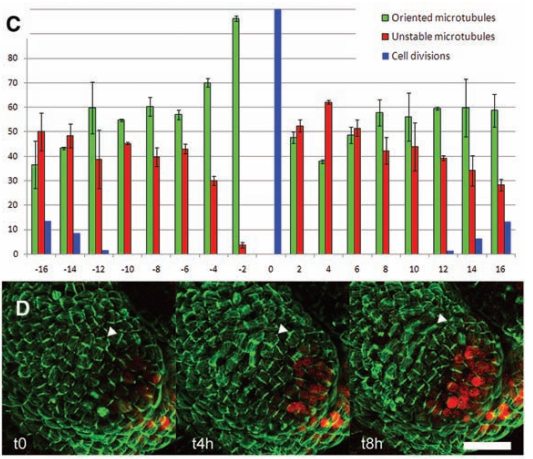

Fig. 2. Microtubule patterns in the shoot apical meristem. (**A**) *p35S::GFP-MBD* expression at the surface of a representative meristem 48 hours after NPA removal. Scale bar, 20 μm. (**B**) Close-up of the same group of cells at the periphery of the meristem, with mixed microtubule orientation before primordium initiation and a coherent supracellular microtubule alignment 20 hours later as the primordium grows out. The blue star marks the same position in both images. Scale bar, 10 μm. (**C**) Cortical microtubule behavior in each cell of the meristematic dome every 2 hours for 16 hours before and after cell division ($n = 144$ cells, compiled from five meristems). Blue, percentage of dividing cells at each time point; green, percentage of cells with one major orientation maintained between two time points; red, percentage of cells with a changing microtubule orientation greater than 30° over two time points. (**D**) *p35S::GFP-MBD* (green) and *pFIL::dsRED-N7* (red) expression in the boundary (arrowhead) of a representative meristem at three time points. Scale bar, 20 μm.

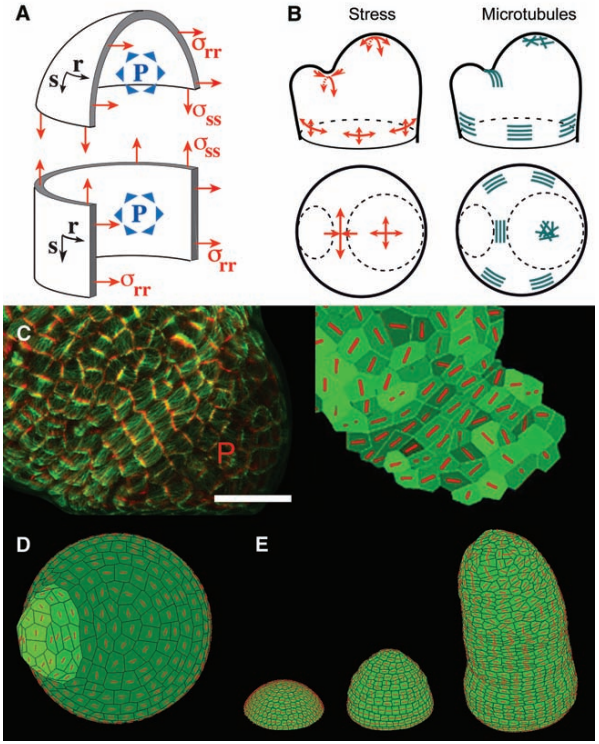

Fig. 3. Physical calculations and modeling of stress patterns in the meristem. (**A**) The meristem modeled as a pressure vessel. Each point has a coordinate in the orthoradial (r) and meridional (s) direction and is characterized by a curvature tensor (C_{ss}, C_{rr}, C_{rs}) and a stress tensor (σ_{ss}, σ_{rr}, σ_{rs}), where R is the radius of the cylindrical stem and of the apical dome, and P is pressure. (**B**) The direction of microtubules is in agreement with the highest-stress orientations. The mechanical equilibrium of the outer layer imposes $\partial_s\sigma_{ss} + \partial_r\sigma_{rs} = 0$, $\partial_s\sigma_{rs} + \partial_r\sigma_{rr} = 0$, and $C_{ss}\sigma_{ss} + C_{rr}\sigma_{rr} + 2C_{rs}\sigma_{rs} = P$, where ∂_s is the partial derivative with respect to s. In the following, we consider only special points (of local symmetry) for which (r,s) are principal directions and $C_{rs} = 0$, $\sigma_{rs} = 0$. If the apical dome is represented as a spherical dome of radius R, we obtain $\sigma_{ss} = \sigma_{rr} = PR/2$, meaning that the stress is isotropic (*44*). This is correlated with the absence of preferential direction for microtubules in the apical dome. $\sigma_N = PR/2$ serves as a reference for stress and $\delta = |\sigma_{ss} - \sigma_{rr}|/\sigma_N$ as a measure of the anisotropy of stress. We represent the flanks of the meristem as a cylinder of radius R. The stress is greater in the circumferential direction, $\sigma_{rr} = PR$, than along the meridian, $\sigma_{ss} = PR/2$ (*44*), so that $\delta = 1$, thus leading to a strongly anisotropic stress on the flanks of the meristem. We consider the center of the crease between a primordium and the apex as having radii of curvature R along the axis of the crease, r, and $-\rho$ in the perpendicular direction, s. The minus sign denotes the inverted direction of curvature with respect to the rest of the meristem. The corresponding curvatures are $C_{ss} = -1/\rho$ and $C_{rr} = 1/R$. The equations of equilibrium can be solved in the limit where ρ is small relative to R: $\sigma_{ss} \approx -P\rho/2$ and $\sigma_{rr} \approx PR/2$, so that $\delta \approx 1$, thus leading to a strongly anisotropic stress at the crease between a primordium and the apex. (**C**) Left: *p35S::GFP-MBD* marking cortical microtubules (green) and cell shape (red) at the surface of a meristem generating a young primordium (P). Scale bar, 20 μm. Right: Microtubule orientation (red bars) in the 2D stress-feedback model on cells extracted from the confocal data, notably reproducing the original microtubule orientations in the boundary. (**D**) Simulation of an auxin-induced primordium. The 2D stress-feedback model results in alignment of microtubules orthoradially around the growing primordium. (**E**) Tip-growing simulation with the stress-feedback model generating a growing stem. Microtubules align mainly orthoradially on the stem, which has a regular shape.

occurred in any of the surrounding cells 7.5 hours after ablation (fig. S7C). The variability of the results could reflect the different stages of boundary development or the exact position of the ablated cells. We also tried a different set of experiments in which two cells or patches of cells, in close proximity but separated, were ablated. We reasoned that diffusion of any type of biochemical signal emanating from the ablated regions would result in a relatively flat diffusion gradient in the regions between them, and therefore that the microtubule arrays in these regions should not be well defined (fig. S8, A and B). In both cases, with ablations separated by multiple cells or single cells, we found that the resulting microtubule orientations for regions between the ablation sites were well defined and clearly circumferential in nature (fig. S8C; four of four experiments). This pattern matches our theoretical predictions for stress patterns surrounding two ablation sites but did not match our prediction for response to a diffusion gradient. Although stress is the simplest explanation, more complex, non-mechanical cell-cell communication models are still possible.

Application of constraints shows a cell-autonomous microtubule response to stress. To more directly ascertain the relationship between microtubule orientations and mechanical signals, we pursued a second approach involving the direct application of force to the meristem. We designed growth chambers in which meristems could be constrained between one fixed teflon blade and one teflon blade attached to a spring (Fig. 4, C and D). Using this device, we were able to change meristem shape (Fig. 4E and figs. S9A and S10). After the release of the constraint, the meristem reverted to its original shape, showing its elastic properties, and later initiated organs (fig. S9A). We predicted a weakly anisotropic stress larger in the direction parallel to the blades (fig. S10). Consistent with these calculations, only weak anisotropic changes in the shape of individual cells were visible at the meristem summit of the constrained meristems (Fig. 4F and movie S5).

We next analyzed the behavior of the cortical microtubules in each cell before and after the constraint. This revealed that the number of cells with unstable microtubules decreased relative to observations of nonconstrained meristems (Fig. 4G, green histograms, and figs. S9B and S10). Second, an analysis of microtubule orientation in 489 individual cells from 13 compressed meristems showed that most cells reoriented their microtubules toward the axis parallel to the blades, either by stabilizing an orientation parallel to the blades after compression or by rotating their microtubules parallel to the blades (Fig. 4F, figs. S10 and S11, and movies S5 and S6). These data are consistent with our proposal that microtubules align parallel to maximal stress directions. Although the response was statistically significant under the conditions tested here, it was also a noisy response because even neighboring cells can have micro-

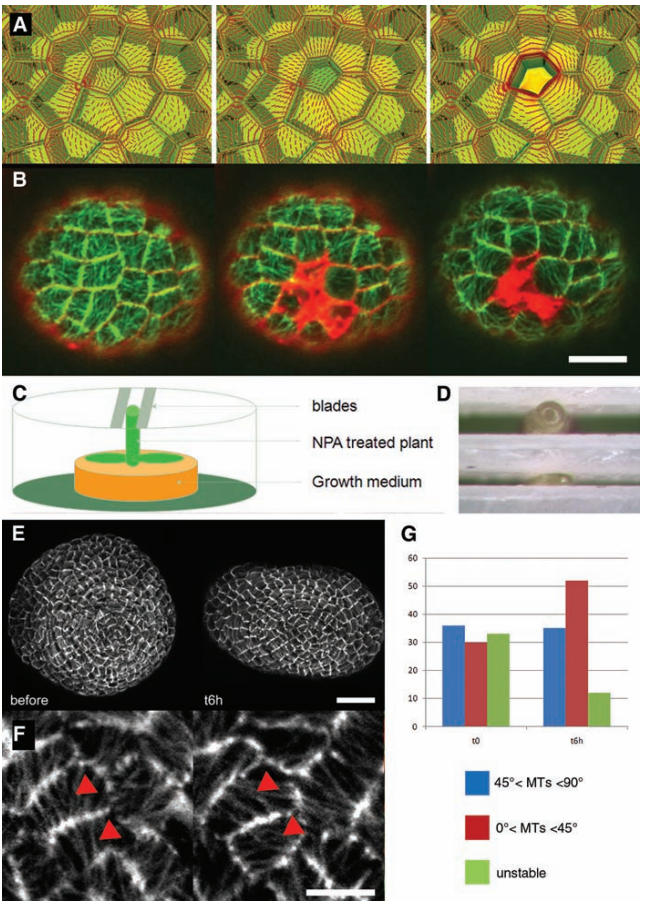

Fig. 4. Reorientation of the cortical microtubules in the presence of a mechanical stress. (**A**) Theoretical principal stress direction pattern (red lines) in outer surface of meristem tissue obtained from FEM simulation of L1 layer under uniform tension and turgor pressure, before and after ablation. Color gives relative values of maximal stress (green, low; red, high). Left: A stress pattern in a group of reference cells. Middle: Radial stresses after the drop of turgor in an ablated cell at the center. Right: Circumferential stresses after the weakening of the top wall. (**B**) *GFP-MBD* expression (green) in the L1 layer of the central zone of a meristem just before, just after, and 6 hours 30 min after ablation (FM4-64 staining in red). Scale bar, 10 μm. (**C**) Schematic drawing of the setup used to apply lateral constraints onto the meristem. (**D**) An NPA-treated plant with a naked meristem is put between two blades, and the blades are then adjusted to compress the apex. (**E**) *GFP-MBD* expression in the L1 layer of a meristem before the application of the constraint (left) and 6 hours (right) after the application of the constraint. Scale bar, 20 μm. (**F**) Close-up showing the microtubule reorientations before and after the application of the constraint. Arrowheads mark cells where microtubules have reoriented parallel to the blades. Scale bar, 5 μm. (**G**) Six hours after the application of the constraint, the number of cells with unclear microtubule orientation (green) is decreasing while the number of cells with microtubules having an angle greater than 45° (blue) remains relatively stable and the number of cells with microtubules having an angle less than 45° with the blades (red) is increasing; t0 corresponds to 0 hours after compression. This tendency to alignment matches the predicted weak anisotropy of stress (see fig. S10).

tubules with radically different orientations (Fig. 4F and movie S5). We propose that this variability reflects the cell-autonomous nature of the response and that this follows from the likely different mechanical configurations of different plant cells.

Concluding remarks. We have described a link between mechanical forces and development in plants. Recent work has also revealed such a relation in animals. In particular, the phenomenon of wound-induced actin alignment in epithelial sheets closely parallels the alignment of plant microtubules around a wound, with both responses presumably functioning to reduce or heal tissue damage (*42*). Unlike animals, however, plant tissues seem to react to oriented forces by conferring anisotropic properties to their extracellular matrix. As a result, plant tissues seem to react to mechanical forces as solids, whereas animal tissues react as fluids. From a physical perspective, this points to a basic difference between the two kingdoms.

On the basis of our results, we propose that two fundamental regulatory circuits control plant morphogenesis at the shoot apex. First, a microtubule-dependent, cell-autonomous mechanism mechanically reinforces cells against maximal tension directions along the meristem surface, most likely via the regulation of load-bearing cellulose fiber deposition and by the addition of new walls generated by oriented mitosis in these directions. This mechanism is required for specific morphogenetic events such as tissue folding and the maintenance of a cylindrical stem. However, in contrast to previous proposals (*36*, *43*), this stress-dependent control of morphogenesis at the meristem can be uncoupled from the control of differential expansion rates, because the rapid outgrowth of organs at particular locations continues despite microtubule depolymerization. This second process involves the creation of differential auxin concentrations through polar transport and possibly synthesis (*17*–*21*). We therefore propose that auxin-dependent patterning operates at least partially independently of, and in parallel to, the microtubule-controlled anisotropy. Our experimental results and models show that these two mechanisms are sufficient to explain all observed complex shape changes at the meristem.

References and Notes

1. W. S. Peters, A. D. Tomos, *Ann. Bot.* **77**, 657 (1996).
2. P. Schopfer, *Am. J. Bot.* **93**, 1415 (2006).
3. E. S. Castle, *J. Cell. Comp. Physiol.* **10**, 113 (1937).
4. D. J. Cosgrove, *Plant Physiol. Biochem.* **38**, 109 (2000).
5. G. O. Wasteneys, M. E. Galway, *Annu. Rev. Plant Biol.* **54**, 691 (2003).
6. A. R. Paredez, C. R. Somerville, D. W. Ehrhardt, *Science* **312**, 1491 (2006); published online 20 April 2006 (10.1126/science.1126551).
7. P. B. Green, A. King, *Aust. J. Biol. Sci.* **19**, 421 (1966).
8. R. E. Williamson, *Aust. J. Plant Physiol.* **17**, 601 (1990).
9. A. L. Cleary, A. R. Hardham, *Plant Cell Physiol.* **34**, 1003 (1993).
10. C. L. Wymer, S. A. Wymer, D. J. Cosgrove, R. J. Cyr, *Plant Physiol.* **110**, 425 (1996).
11. K. Fischer, P. Schopfer, *Plant J.* **15**, 119 (1998).
12. J. Traas, J. H. Doonan, *Int. Rev. Cytol.* **208**, 161 (2001).
13. D. Kwiatkowska, J. Dumais, *J. Exp. Bot.* **54**, 1585 (2003).
14. O. Grandjean *et al.*, *Plant Cell* **16**, 74 (2004).

15. C. W. J. Beenakker, *Phys. Rev. Lett.* **57**, 2454 (1986).
16. J. A. Glazier, S. P. Gross, J. Stavans, *Phys. Rev. A* **36**, 306 (1987).
17. D. Reinhardt *et al.*, *Nature* **426**, 255 (2003).
18. M. G. Heisler *et al.*, *Curr. Biol.* **15**, 1899 (2005).
19. P. B. de Reuille *et al.*, *Proc. Natl. Acad. Sci. U.S.A.* **103**, 1627 (2006).
20. H. Jönsson, M. G. Heisler, B. E. Shapiro, E. M. Meyerowitz, E. Mjolsness, *Proc. Natl. Acad. Sci. U.S.A.* **103**, 1633 (2006).
21. R. S. Smith *et al.*, *Proc. Natl. Acad. Sci. U.S.A.* **103**, 1301 (2006).
22. S. Sakaguchi, T. Hogetsu, N. Hara, *Bot. Mag. (Tokyo)* **101**, 497 (1988).
23. J. M. Selker, *Protoplasma* **158**, 95 (1990).
24. Z. Hejnowicz, *Protoplasma* **225**, 243 (2005).
25. J. Chan, G. Calder, S. Fox, C. Lloyd, *Nat. Cell Biol.* **9**, 171 (2007).
26. P. M. Lintilhac, in *Positional Controls in Plant Development*, P. W. Barlow, D. J. Carr, Eds. (Cambridge Univ. Press, Cambridge, 1984), pp. 83–105.
27. J. Dumais, C. R. Steele, *J. Plant Growth Regul.* **19**, 7 (2000).
28. E. Farge, *Curr. Biol.* **13**, 1365 (2003).
29. L. Hufnagel, A. A. Teleman, H. Rouault, S. M. Cohen, B. I. Shraiman, *Proc. Natl. Acad. Sci. U.S.A.* **104**, 3835 (2007).
30. T. Lecuit, P. F. Lenne, *Nat. Rev. Mol. Cell Biol.* **8**, 633 (2007).
31. J. M. Hush, R. L. Overall, *Cell Biol. Int. Rep.* **15**, 551 (1991).
32. R. E. Williamson, *Int. Rev. Cytol.* **129**, 135 (1991).
33. R. J. Cyr, *Annu. Rev. Cell Biol.* **10**, 153 (1994).
34. Z. Hejnowicz, in *Pattern Formation in Biology, Vision and Dynamics*, A. Carbone, M. Gromov, P. Prusinkiewicz, Eds. (World Scientific, Singapore, 2000), pp. 240–251.
35. C. Wei, P. M. Lintilhac, J. J. Tanguay, *Plant Physiol.* **126**, 1129 (2001).
36. J. M. Selker, G. L. Steucek, P. B. Green, *Dev. Biol.* **153**, 29 (1992).
37. S. Savaldi-Goldstein, J. Chory, *Curr. Opin. Plant Biol.* **11**, 42 (2008).
38. See supporting material on *Science* Online.
39. J. Dumais, S. L. Shaw, C. R. Steele, S. R. Long, P. M. Ray, *Int. J. Dev. Biol.* **50**, 209 (2006).
40. J. M. Hush, C. R. Hawes, R. L. Overall, *J. Cell Sci.* **96**, 47 (1990).
41. K. C. Goodbody, C. Lloyd, *Protoplasma* **157**, 92 (1990).
42. P. Martin, J. Lewis, *Nature* **360**, 179 (1992).
43. L. F. Hernandez, P. B. Green, *Plant Cell* **5**, 1725 (1993).
44. W. Flugge, *Stresses in Shells* (Springer-Verlag, New York, ed. 2, 1973).
45. We thank A. Roeder for critical reading of the manuscript, and P. Barbier de Reuille and IFR128 Platim for help with imaging. Supported by the International Human Frontier Science Program Organization, by U.S. Department of Energy grant FG02-88ER13873 (E.M.M.), by the Balzan Foundation (E.M.M.), and by the Swedish Research Council (H.J.).

Supporting Online Material

www.sciencemag.org/cgi/content/full/322/5908/1650/DC1
Materials and Methods
SOM Text
Figs. S1 to S11
Movies S1 to S6
References

8 September 2008; accepted 14 November 2008
10.1126/science.1165594

Paper III

Statistical Properties of Cell Topology and Geometry in a Tissue-Growth Model

Patrik Sahlin[1], Olivier Hamant[2], and Henrik Jönsson[1]

[1] Computational Biology & Biological Physics, Department of Theoretical Physics, Lund University, Sölvegatan 14A, SE-223 62 Lund, Sweden
{sahlin,henrik}@thep.lu.se
[2] INRA, CNRS, ENS, Université de Lyon, 46 Allée d'Italie, 69364 Lyon Cedex 07, France
Olivier.Hamant@ens-lyon.fr

Abstract. Statistical properties of cell topologies in two-dimensional tissues have recently been suggested to be a consequence of cell divisions. Different rules for the positioning of new walls in plants have been proposed, where e.g. Errara's rule state that new walls are added with the shortest possible path dividing the mother cell's volume into two equal parts. Here, we show that for an isotropically growing tissue Errara's rule results in the correct distributions of number of cell neighbors as well as cellular geometries, in contrast to a random division rule. Further we show that wall mechanics constrain the isotropic growth such that the resulting cell shape distributions more closely agree with experimental data extracted from the shoot apex of *Arabidopsis thaliana*.

1 Introduction

Cell division in plants has been studied by plant biologists for over one hundred years (see review in [1]). From simple microscope observations biologists have formulated rules for cell division. During mitosis plant cells are divided into two daughter cells by introducing a dividing cell wall. Hofmeister suggested a rule where new cell walls are formed perpendicular to the main axis of growth, i.e. perpendicular to the main axis of the cell [2]. Sachs noted that new walls form almost perpendicular to old walls [3]. Similarly to Hofmeister's rule, Errara's rule state that the division is along the shortest path dividing the mother cell into two parts of equal volume [4]. More recently, experiments where spherical cells have been compressed into oval shapes agrees with these rules [5,6]. It has also been seen that the arrangement of cytoskeletal structures reveal the placement of new cell walls [1].

Many biological tissues develop in two-dimensional sheets. The epidermal layer in plants is an example, where anticlinal divisions and the lack of cell migration assure the two-dimensional structure of the layer. The epidermal layer can then be described by a network of connected polygons (cells), edges (walls) and vertices, where the connections are updated at divisions only. The predominant existance of three-vertices leads to the average number of cell neighbors (walls)

J. Zhou (Ed.): Complex 2009, Part I, LNICST 4, pp. 971–979, 2009.
© ICST Institute for Computer Sciences, Social Informatics and Telecommunications Engineering 2009

to be six following Euler's rule. But the average can be fulfilled by many neighbor distributions, and already in the 1920's F. T. Lewis studied this in growing and proliferating cucumber epithelia [7,8]. He found that although most cells had six neighbors (47%), the distribution was not symmetric, with more five-sided cells (25%) compared to seven-sided (22%). He also noted the non-existance of triangular cells as well as cells with more than nine neighbors. Recently, Gibson *et. al.* found similar asymmetric distributions in epithelial cell layers in several animal tissues including epithelia from *Drosophila melanogaster* wing primordium [9]. Interestingly, they also introduced a probabilistic model where a discrete Markov chain was used to describe topological updates due to cell divisions and the model was able to predict the experimental distribution of the number of cell neighbors.

The approach by Gibson *et al.* focused on the topology of the cells in the tissue, but disregarded details of cellular geometry, growth and proliferation. Here, we use a two-dimensional cell-based tissue growth model to analyze how explicit division rules and wall mechanics lead to different topological as well as cellular shape distributions. We assume isotropic growth, and mainly study tissues with quite homogeneous cell sizes. This resembles the situation in the plant shoot apex, and we compare our models with novel data from the *Arabidopsis thaliana* shoot apical meristem.

Our model allow us to compare Errara's classical division rule (new walls are placed such that the cell is divided into two equally sized daughters along the shortest path) with a random-direction division rule. We also investigate how wall mechanics constraining the purely isotropic growth affect the topology and cell geometry. We compare the resulting tissues with the distributions of the number of neighbors (topology) as well as cell shapes (geometry) from experimental data.

2 Materials and Methods

2.1 Experimental Data

The model results are compared with the experimental data presented in Gibson *et al.* [9], as well as new data from the shoot apex in *Arabidopsis thaliana* (Fig. 1). The shoot data was extracted from a confocal projection using the merryproj software [10]. It is interesting to note that although the statistics is sparse, the overall topological distribution in the shoot data is very similar to the *Drosophila* case as well as the Lewis data [7,8].

2.2 Tissue Model

The model is a two-dimensional model where the spatial degrees of freedom are for vertices, which are connected via edges that represent cell walls. Each cell is described by a polygon, i.e a number of vertices together with corresponding edges. The vertex positions are updated viscously, where we assume that velocities are proportional to the forces acting upon them. The cell walls are treated

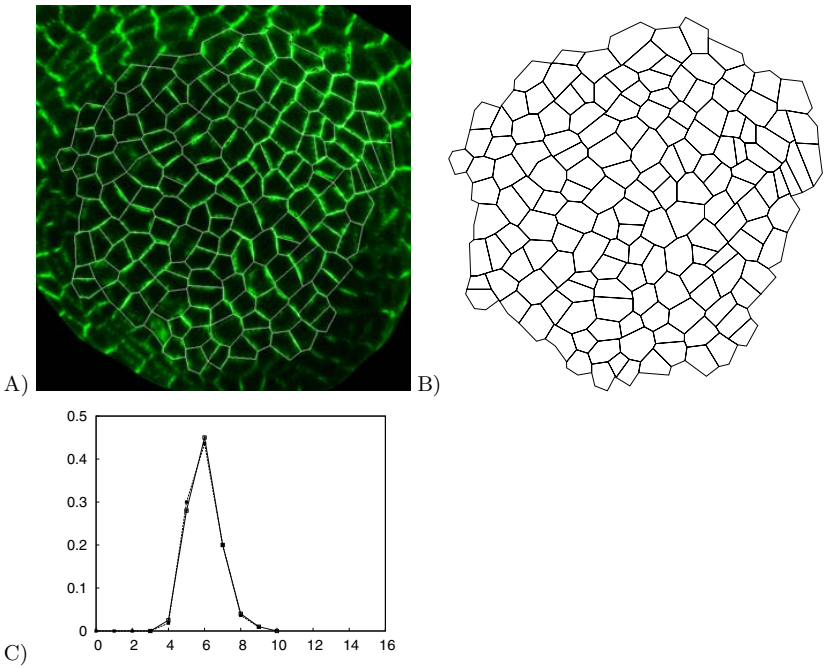

Fig. 1. Data from an image of the meristem of *Arabidopsis* is compared with data from *Drosophila* presented by Gibson *et al.*. A) The original image taken with confocal microscopy. Cell walls are marked manually. B) The template extracted from the image. C) The distribution of the number of neighbors for *Arabidopsis thaliana* marked with filled black squares (■) (110 cells) and *Drosophila melanogaster* marked with empty white squares (□) (2,172 cells) [9].

as mechanical springs. We describe the dynamics with a system of ordinary differential equations originating from an isotropic growth term, wall mechanics, and plastic wall growth. The contribution from wall springs is described by

$$\frac{d\mathbf{v}_i}{dt} = k_w \sum_{j \in \mathcal{C}(i)} \frac{\mathbf{u}_{ij}}{|\mathbf{u}_{ij}|} \left(\frac{|\mathbf{u}_{ij}| - L_{ij}}{L_{ij}} \right) \quad , \tag{1}$$

where $\mathbf{v}_i$ is the position of vertex i, k_w is a material constant setting the strength of the wall springs, L_{ij} is the resting length of the wall spring between vertex i and j, and $\mathbf{u}_{ij} = \mathbf{v}_j - \mathbf{v}_i$. The summation is over vertices connected via edges to vertex i.

Cell walls under tension grow plastically. The change in resting length of a wall spring is

$$\frac{dL_{ij}}{dt} = k_g \Theta \left(\frac{|\mathbf{u}_{ij}| - L_{ij}}{L_{ij}} \right) \quad , \tag{2}$$

where k_g is a constant setting the rate of growth and Θ is the ramp function defined as

$$\Theta(x) = \begin{cases} x \text{ if } x \geq 0 \\ 0 \text{ if } x < 0 \end{cases} . \tag{3}$$

A radial force is used to model isotropic growth of the tissue originating from internal cell pressure. The force on a vertex is described by

$$\frac{d\mathbf{v}_i}{dt} = k_r \mathbf{v}_i \ , \tag{4}$$

where k_r is a constant setting the strength of the radial force.

To decrease computational time, cells on the boundary of the tissue are removed if a cell is outside a given threshold radius, R_t.

Division Rules. If the area of a cell exceeds a threshold value, D_t, the cell is divided into two daughter cells. At division, two new vertices are added at two different walls in the cell, and a new wall connects the vertices. The resting length of the new wall is set to the distance between the two vertices. In addition, the walls at which the new vertices are added are split into two, and the new resting lengths are set proportionally to the split distance such that $L_1^{\text{new}} + L_2^{\text{new}} = L^{\text{old}}$.

The new wall dividing the cell into two daughters is defined by a spatial position and a direction. As an approximation of dividing the cell into two almost equally sized daughters, the new wall is passing through the center of mass of the dividing cell. The direction of the new wall is determined from two different rules. In the first rule, called *random direction*, a random (uniform) direction is chosen. In the second rule, called *shortest path*, the direction of the dividing wall is chosen such that the path through the cell is the shortest possible. This is the model definition of the Errara rule. To avoid four-vertices, walls that are closer to a vertex than a threshold, $w_t L_{ij}$ is moved away from the vertex to the threshold position.

2.3 Simulations

The system of ordinary differential equations is solved numerically with a 5th order Runge-Kutta ODE solver using adaptive stepsize. Data is sampled at ten different time points. As we remove cells at the boundary a new generation of cells is present at each time point. The number of cell neighbors are collected for all cells, excluding cells at the boundary. Five different intial states are used for each model to gather statistics. The initial states are all one single cell represented by a regular polygon with three, five, seven, nine, or eleven vertices. Data from the 50 different time points is averaged to give final distributions for each model.

We use in house developed software allowing for discrete updates between each time step taken by the numerical ODE solver. In these updates we check cells for division and removal. Parameter values used in the simulations are presented in Table 1.

Table 1. Parameter values used during simulations

Parameter	With mechanics	Without mechanics
k_w	0.05	-
k_g	0.01	-
k_r	0.05	0.05
D_t	1	1
R_t	10	10
w_t	0.1	0.1

3 Results

3.1 Comparing Different Division Rules

First we compared the topology distributions from the two different cell division rules. The result is presented in Figs. 2A and C, where the data from the simulations are presented together with the experimental distributions. For both division rules the distributions have their maximum at six cell neighbors, but while the distribution for the shortest path division rule match the experimental data well, the distribution for the random direction division rule is broader compared to the experimental data.

3.2 Removal of Spring Wall Mechanics

To study how removal of wall mechanics affects the distribution of cell neighbors, we kept the radial force that drives the isotropic growth, but removed the cell wall springs.

The result is presented in Figs. 2B and D. What might be found surprising is that the differences between the distributions with and without wall spring mechanics are very small. This is true for both the shortest path division rule and the random direction division rule.

3.3 A Quantative Measurement of Cell Shapes

A striking result from our simulations is that even if the mechanics has no or little effect on the distributions, there is an obvious visual difference of cell shapes between simulations with and without mechanics. Examples of cell shapes from simulations with the two different division rules are presented in Fig. 3. Clearly, the cell shapes emerging using the shortest path division rule is more plant-like, and also the simulations with mechanics look more like cellular tissue in comparison with the non-mechanical simulations.

To quantify differences in cell shape, we measure the ratio between the length of the boundary of a cell squared and the area of the cell. In Fig. 4 this measure is presented for different simulations and compared with the *in vivo* data. First, it can be seen that the shortest path division rule generally has a closer match to the experimental values than the random direction division rule. The random

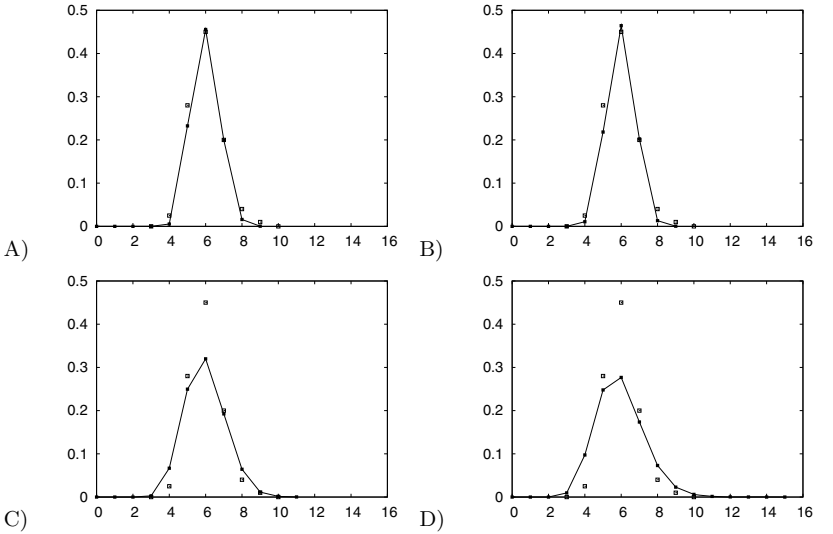

Fig. 2. Distributions of number of neighbors for simulations with different division rules with and without mechanics. Filled black squares (■) marks results from simulations while empty white squares (□) marks experimental data. A) Shortest path division rule with mechanics. B) Shortest path division rule without mechanics. C) Random direction division rule with mechanics. D) Random direction division rule without mechanics.

direction division rule not only differ more in the average value, but it also has a much larger spread among cells. A closer inspection also reveals that simulations with mechanics is closer to the experimental values than simulations without mechanics.

4 Discussion

We have used a simple two-dimensional cell-based tissue growth and proliferation model to investigate the dependence on cell division rules on statistical properties of cell topology and geometry. We used an isotropically growing tissue and showed that one of the classical rules for plant division (Errara's rule), where new plant walls appear at the shortest path that divides the cell in two equally sized dughter cells, indeed do produce a skewed topology distribution seen *in vivo* with an average of six neighbors but with more five than seven neighbor cells (Fig. 2A). On the contrary, the 'control' model with new walls placed in a random direction did not follow this distribution (Fig. 2C).

For each division rule we performed two sets of simulations, one with wall mechanics and one without. While the non-mechanics simulations follow pure isotropic growth, wall mechanics constrains the growth via a wall growth model.

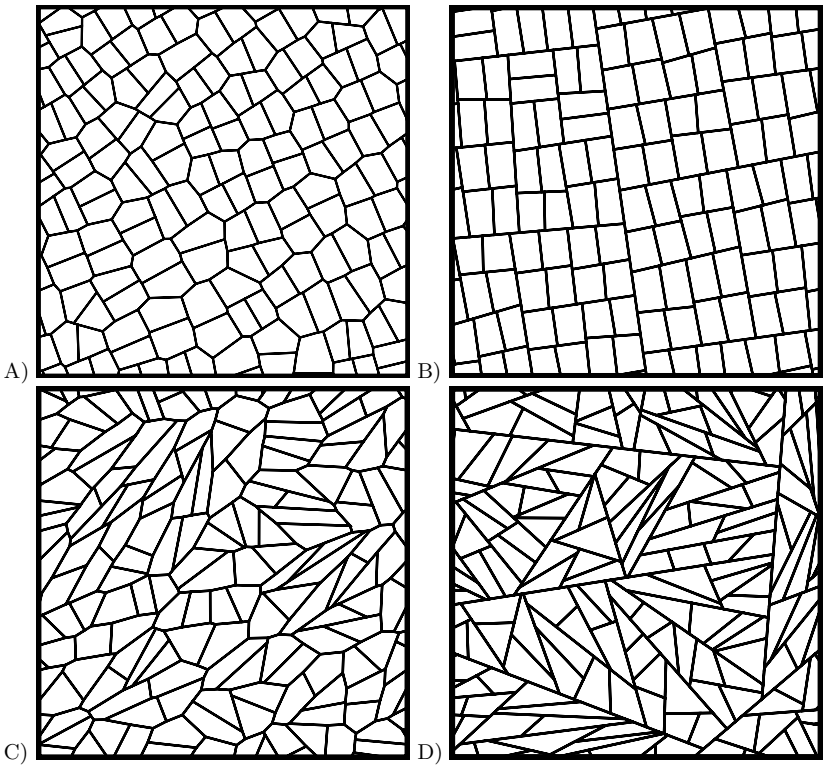

Fig. 3. Examples of simulations with different division rules. Simulations with the shortest path division rule with (A) and without (B) mechanics. Simulations with the random division rule with (C) and without (D) mechanics.

When comparing distributions of number of neighbors there was no difference between the sets with mechanics and the simulations without mechanics, although a visual difference could be seen, where the simulations with mechanics produced more plant-like cells (Fig. 3).

To investigate this further we quantified cell shapes and compared with novel data from the *Arabidopsis* shoot apex. We could again see that Errara's division rule produced a statistical distribution very similar to our measured data, while the random division rule produced far more asymmetric cell shapes. In this case, we could also see a small difference between simulations with or without mechanics, where including wall mechanics generated shapes more similar to the *in vivo* data (Fig 4).

In conclusion, we have showed that statistical properties of cell topology and shape indeed can be used to discern among different model hypotheses for cell proliferation. Interestingly, divisions at random directions do not lead to correct

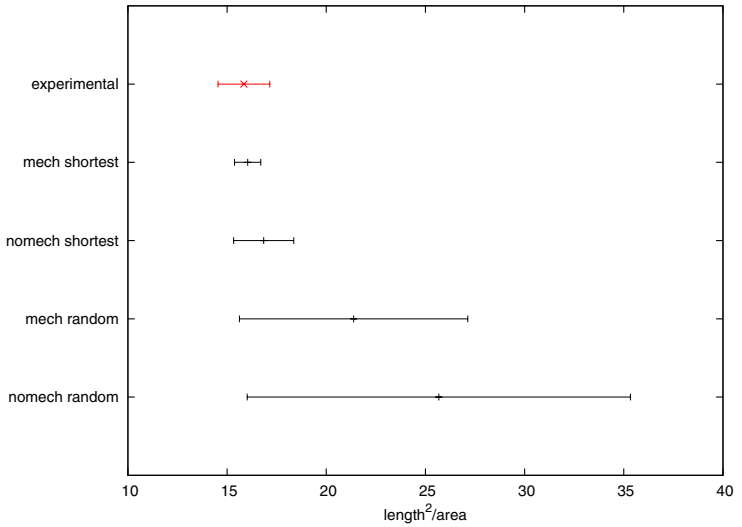

Fig. 4. Mean and standard deviation for the ratio between length of cell boundary squared and cell area. The data point marked with a cross (×) shows the experimental data. Other data points marked with a vertical dash (|) show results from simulations. Simulations have been done with the two different division rules, with and without mechanics.

topology or cell geometries, while Errara's classical cell division rule do agree with the statistical properties from experimental data. Of course, statistical agreement is only a first test which many hypotheses may pass, and ultimately the hypotheses must be compared with statistics of single cell data. Still, we have presented a useful methodology, where explicit and mechanistic hypotheses that combine into a cellular plant growth and proliferation model can be compared on merits based on experimental data.

Acknowledgement. We thank Pawel Krupinski and Pontus Melke for discussions. This work was in part supported by the Swedish Research Council and the Human Frontier Science Program.

References

1. Smith, L.G.: Plant Cell Division: Building Walls in the Right Places. Nat. Rev. Mol. Cell. Biol. 2, 33–39 (2001)
2. Hofmeister, W.: Zusatze und Berichtigungen zu den 1851 Veröffentlichen Untersuchungengen der Entwicklung Höherer Kryptogamen. Jahrbucher für Wissenschaft und Botanik 3, 259–293 (1863)
3. Sachs, J.: Über die Anordnung der Zellen in Jüngsten Pflanzentheilen. Arb. bot. Inst. Wurzburg 2, 46 (1878)

4. Errera, L.: Über Zellformen und Siefenblasen. Botanisches Centralblatt 34, 395–399 (1888)
5. Lintilhac, P.M., Vesecky, T.B.: Stress-induced Alignment of Division Plane in Plant Tissues Grown in Vitro. Nature 307, 363–364 (1984)
6. Lynch, T.M., Lintilhac, P.M.: Mechanical Signals in Plant Development: A New Method for Single Cell Studies. Dev. Biol. 181, 246–256 (1997)
7. Lewis, F.T.: The effect of cell division on the shape and size of hexagonal cells. Anatomical Records 33, 331–355 (1926)
8. Lewis, F.T.: The correlation between cell division and the shapes and sizes of prismatic cells in the epidermis of cucumis. Anatomical Records 38, 341–376 (1928)
9. Gibson, M.C., Patel, A.B., Nagpal, R., Perrimon, N.: The Emergence of Geometric Order in Proliferating Metazoan Epithelia. Nature 442, 1038–1041 (2006)
10. de Reuille, P.B., Bohn-Courseau, I., Godin, C., Traas, J.: A Protocol to Analyse Cellular Dynamics During Plant Development. Plant J. 44, 1045–1053 (2005)

Paper IV

A modeling study on how cell division affects properties of epithelial tissues

Patrik Sahlin[1] and Henrik Jönsson[1,*]

[1]Computational Biology & Biological Physics
Lund University, Sölvegatan 14A, SE 223 62 Lund, Sweden
*Corresponding author

Abstract

Cell proliferation affects both cellular geometry and topology in a growing tissue, and hence rules for cell division are key to understand multicellular development. Epithelial cell layers have for long times been used to investigate how cell proliferation leads to tissue-scale properties, including organism-independent distributions of cell areas and number of neighbors. We use a cell-based two-dimensional tissue growth model including mechanics to investigate how different cell division rules result in different statistical properties of the cells at the tissue level. We focus on isotropic growth and division rules suggested for plant cells, and compare the models with data from the *Arabidopsis* shoot. We find that several division rules can lead to the correct distribution of number of neighbors, as seen in recent studies. In addition we find that when also geometrical properties are taken into account other constraints on the cell division rules result. We find that division rules acting in favor of equally sized and symmetrically shaped daughter cells can best describe the statistical tissue properties.

Introduction

Multicellular development is governed by cellular differentiation and morphogenesis. Cellular differentiation has mainly been described as a process of gene regulation and molecular signaling between cells, although signaling via mechanical interactions due to the morphogenesis has recently been suggested [1–4]. Both molecular and mechanical signaling between cells in a growing tissue are affected by cell division. Therefore, cell division is one of the means for an organism to regulate different aspects of development [5].

In many growing epithelial tissues, cells divide perpendicular to the surface and this allows for a detailed study of cell topology (quantified by the number of neighbors for each cell) and geometry (cell shapes and sizes) in these monolayered tissues. Such a tissue may hence be described as a two-dimensional sheet

defined by vertex points representing wall junctions, one-dimensional edges representing cell walls, and two-dimensional faces representing cells. Epithelial tissues are dominated by three-cell vertices and according to Euler's law the average number of neighbors is therefore equal to six. In the 1920's, F.T. Lewis showed that cucumber epithelium has a skew distribution of number of neighbors, dominated by hexagonal cells (47%) and with more five-sided cells (25%) than seven-sided (22%) [6, 7]. He also noted that the distribution was quite narrow, ranging from four- to eight-sided cells. More interestingly, surprisingly similar topologies have been found in epithelia of many species ranging over different kingdoms [8]. An important question is how these topological distributions can emerge at a tissue level from cell division.

The epidermal layer in plants provides a beneficial model system for investigating cell division without cellular reorganization, since plant cell walls govern tissue rigidity and there is no sliding between cells. Hence, cell division is the only way to affect the topology of the tissue and proper cell division is needed for developmental processes in the plant [5]. When a plant cell divides, a new cell wall is added between the two daughter nuclei. In the epidermal cell layer new walls are anticlinal, preserving the two-dimensional structure of the tissue. Also, at the shoot apical meristem (SAM) summit, growth is isotropic [9, 10], and the tissue may be represented by a two-dimensional sheet with isotropic growth.

Rules for determining the position and direction of new cells walls in plants have been proposed for more than a century [5, 11–14]. Hofmeister (1863) suggested that cells divide perpendicular to the main axis of growth, which also correlates with the main axis of cell extension in many plant tissues. Sachs (1878) noted that new walls form nearly perpendicularly to older walls. Errara (1888) proposed that cells behave similarly to soap bubbles, and that cells are divided by the shortest path dividing the cells into two equally sized daughters. More recently, cell growth and proliferation have been investigated in more detail at the plant shoot, and while clear directional patterns can be found at the periphery where new organs form, strain is isotropic and proliferation directions are omnidirectional at the apex [9, 10]. Division planes in mother and daughter cells can be related where orthogonal division directions are common [9, 10]. Recently, a correlation between the directions of cortical microtubules (MTs) and the cell division plane has also been found [4, 15]. At the SAM summit the MT directions are dynamic and suggested to be random [4]. Two main rules for orienting MTs in plants have been proposed; perpendicular to maximal strain directions, and parallel to maximal stress directions [4, 16].

What biological mechanisms that determine positions and directions of cell division are still unknown, and it may very well be that different mechanisms act in different organisms and even in different tissues of the same organism. Cell division rules have been investigated in mathematical models for a long time [14]. Mathematical models of cell division have recently been used to show that different division rules lead to specific topological distributions on a tissue-scale, and that a subset of the division rules successfully reproduce the common topology distribution found in the epithelium of several organisms [8, 17]. These

models have neglected geometrical properties, but an important property of the successful models was symmetric cell division, *i.e.* the vertices of the mother cell are distributed evenly among the daughter cells.

We have previously introduced a two-dimensional spring-based model to take also geometrical aspects into account and compared simulated tissues with data from the *Arabidopsis* SAM [18]. We were able to show that although cell wall-mechanics is not important for the resulting topology, simulations with mechanics resulted in better shaped cells. Here we continue to use the spring-based model to test different division rules and compare results with experimental data. Using the spring-based model we are able to investigate consequences for both topology and geometry of using the different division rules.

Definitions of division rules and tissue properties

At cell division the mother cell is divided into two daughter cells by introducing a new wall, which is described by a *division plane*. How the division plane is located is determined in the model by a *division rule*. A division rule consists of two mechanisms; one to determine the *division center* and one to determine the *division direction*. The division plane is then the straight path that goes through the division center parallel to the division direction.

In this work we are studying two different mechanisms for determining division centers,

- Center of Mass (COM). The division center is the center of mass of the mother cell.
- Random. The division center is a random point within the mother cell drawn from a uniform distribution.

The COM rule will produce daughters with quite symmetric sizes, while the Random rule allows for asymmetrically sized daughters. In addition, we are studying four different mechanisms for determining the division direction,

- ShortestPath. The direction is the shortest path through the division center. Combined with the COM mechanism for determining the division center this is our representation of Errara's rule [13].
- RandomDirection. The direction is randomly chosen from a uniform distribution.
- Orthogonal. The division direction is orthogonal to the direction of the previous cell division, following patterns seen in plant tissues [9, 10].
- StrainPerpendicular. The direction is perpendicular to the direction of strain in the mother cell (Methods). This rule is our representation of Hofmeisters cell division rule [11].

The division directions are important for determining the shapes of the daughter cells, where the ShortestPath favors more symmetrically shaped daughter

cells, while RandomDirection has no such bias. The two types of mechanisms are combined into division rules with the following notation DivisionDirection|DivisionCenter.

We are interested in two different types of tissue properties.

- **Topology**. We quantify the topology of the tissue by the distribution of number of neighbors.
- **Geometry**. We quantify the geometry of the tissue by distributions of cell shapes and sizes.

Results and Discussion

We performed series of simulations with isotropic growth using a two-dimensional spring-based model, and with different division rules (Methods, Introduction). Cells outside a boundary were removed and statistics was gathered from snapshots of simulated tissues at different time points, neglecting cells at the boundary of the tissue. We analyzed the topologies and the geometries of simulated tissues and compared with experimental data to test different division rules. We also investigated how well tissues fitted to Lewis' law, which states that a linear relationship exists between number of neighbors and areas of cells [7]. Finally, we also simulated an oryzalin experiment by continuing tissue growth after suspending cell division [19].

The COM mechanism for determining the division center is superior to the Random mechanism in reproducing the topology of experiments

First we studied topologies resulting from simulations with the different division rules and compared them with data from the *Arabidopsis* SAM (Figure 1A, Tab. 1). It can be seen that all division rules using the Random mechanism for the orientation of the division center generate distributions of number of neighbors that were wider than the one for the experimental data. To quantify the difference between the topology resulting from each model and the experimental topology, we defined a fitness measure (Methods, Fig. 2A). As can be seen, there is a clear separation between models using the COM mechanism and models using the Random mechanism, where the former have a better fitness. One interesting feature of the experimental number of neighbor distributions is the skewness. Although all models display a skewness in the distribution of number of neighbors, where the number of five-neighbor cells is always larger than the number of seven-neighbor cells (Fig. 1A), the skewnesses associated with models using the COM mechanism are weaker compared with experimental data (Tab. 1).

Among the rules using the COM mechanism, there was a slight advantage for the ShortestPath|COM and the StrainPerpendicular|COM division rules. An interesting result is that the fitness is not fully correlated with

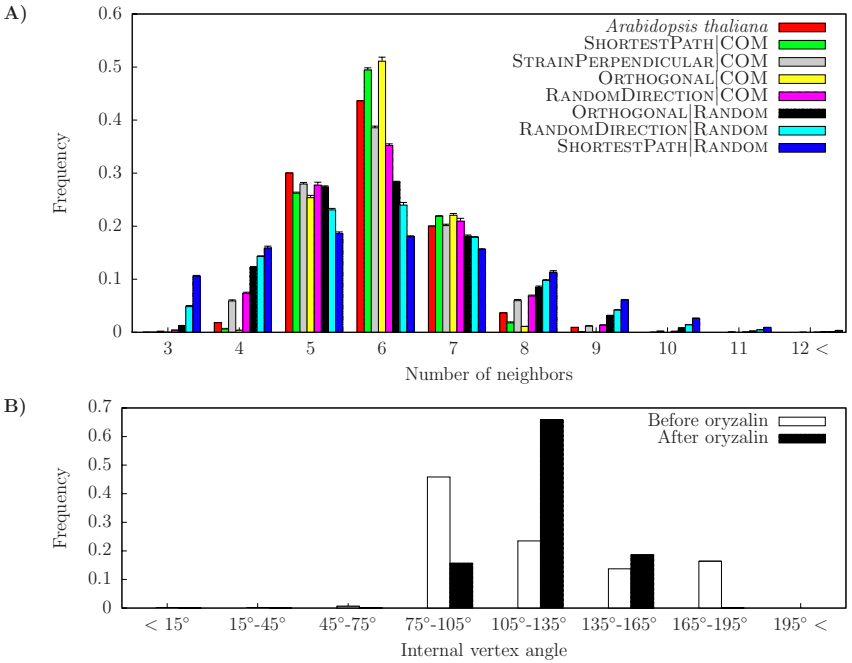

Figure 1: Distributions of number of neighbors and internal vertex angles from simulations with different division rules. Error bars represent standard deviation. A) Distributions of number of neighbors. Experimental data from *Arabidopsis thaliana* is also presented for comparison. B) Distributions of internal vertex angles before and after suppression of cell division.

Division rule	Standard deviation	Skewness
Orthogonal|COM	0.73±0.04	0.14±0.13
ShortestPath|COM	0.76±0.04	0.20±0.14
Arabidopsis thaliana	0.90	0.53
StrainPerpendicular|COM	1.0±0.0	0.39±0.20
RandomDirection|COM	1.1±0.1	0.29±0.17
Orthogonal|Random	1.4±0.1	0.54±0.16
Random|Random	1.6±0.1	0.41±0.13
ShortestPath|Random	1.9±0.1	0.41±0.08

Table 1: Standard deviation and skewness of distributions of number of neighbors. Standard deviation and skewness have been measured for each simulated tissue and the values presented are average values with standard deviation as errors.

the mechanism for determining the division direction. While the ShortestPath|COM division rule had best fitness, the ShortestPath|Random division rule generally performed badly. This shows how important a proper mechanism for determining the division center is as a top performing mechanism for orienting the division direction can easily be turned into the worst by changing the mechanism for determining the division center.

In conclusion, our results show that division rules that divide mother cells into almost symmetrically sized daughters result in topologies with better fitness to experimental data than division rules that generated more asymmetric daughter sizes. This feature was particularly important for generating narrow distributions – as seen in the experimental data – and agrees with what have been shown with non-geometrical models for which a symmetric division of cell vertices has been shown to be important for narrow distributions [8, 17].

ShortestPath and Orthogonal division directions produce most plant-like cell shapes

For simulated tissues generated by division rules with symmetric division (using the COM mechanism), topology alone could not be used to discern among the division rules studied in this work. Instead, we also analyzed geometrical properties, where one can note that cells at the *Arabidopsis* apex have quite symmetrical shapes as measured by the cell area divided by the total cell wall length squared [18]. This shape measure revealed that – for all proposed division rules – cells of the SAM were more symmetrically shaped than cells of simulated tissues (Fig. 2B). Cell shapes of each division rule were differently shaped (Fig. 3 for examples). The division rules that generated cell shapes closest to the experimental data were those with systematic rules for dividing the cell such that the wall is directed perpendicularly to the main axis of the cell (Fig. 2B). The ShortestPath division rule does this explicitly, and the Orthogonal division rule does it implicitly since the isotropic growth together with cell division perpendicular to the last division plane will approximate the shortest path. Interestingly, both these rules have been suggested for plant cells. A third division rule suggested for plant cells is to divide the cell perpendicular to the principal strain direction, but with isotropic growth the maximal growth direction is ambiguous, and the rule led to cell shapes similar to those obtained by choosing a random division direction (Fig. 2B).

In conclusion, our results suggest that epithelial cells in an isotropically growing tissue tend to divide such that symmetrically shaped daughter cells are favored. Our results also emphasize that while using a given division rule can result in a topology very similar to what is found in experiments, the same division rule might not correctly reproduce geometrical properties, in this case cell shape. For example, using the StrainPerpendicular|COM division rule results in a topology resembling the one of an *Arabidopsis* meristem, but the same series of simulations produce cells with a different shape distribution compared with the experimental data. A final note is that an absolute requirement for any of the division rules to generate cell shapes similar to what is seen in

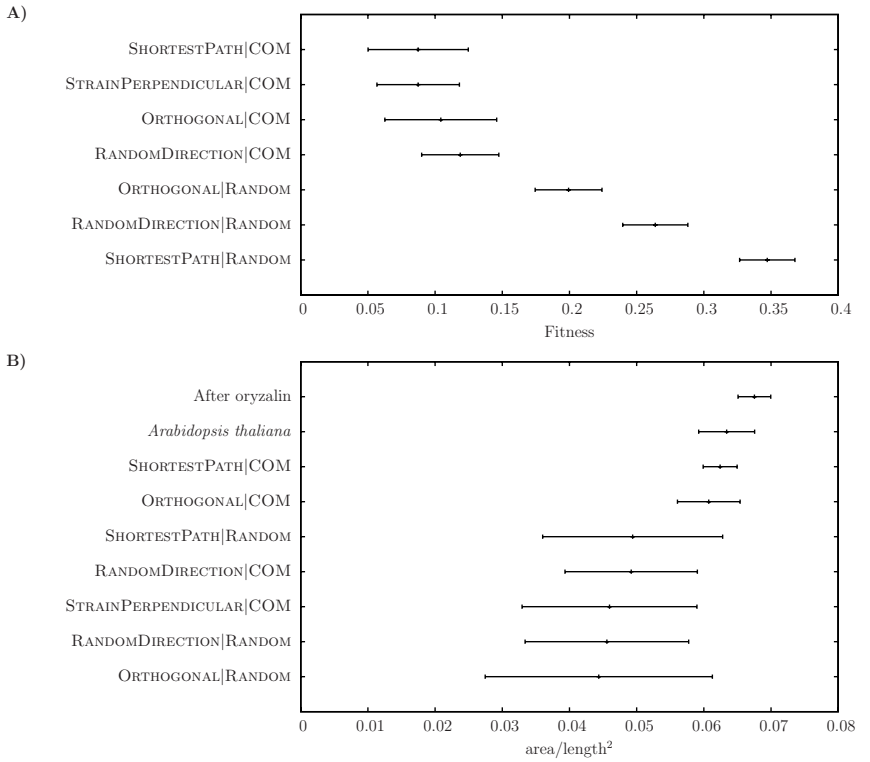

Figure 2: Topological and geometrical properties of simulated tissues. A) The fitness of each division rule. The fitness quantitatively measures how well resulting tissues of simulations with a given division rule reproduces the distribution of number of neighbors compared with experimental data of *Arabidopsis thaliana*. B) Results from the quantitatively measurement of cell shape (Methods). The numerical values for the shape measurement range from zero ("flat" cells without area) and $(4\pi)^{-1} \approx 0.08$ (circular cells).

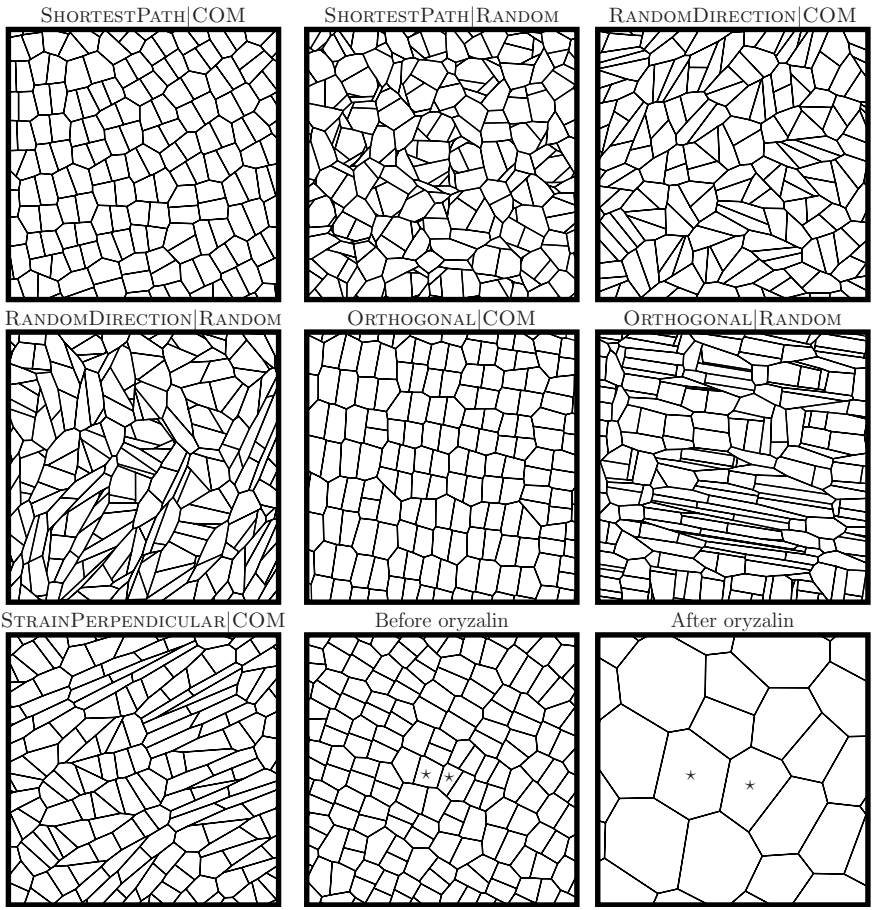

Figure 3: Example images of tissues from simulations with different division rules. The stars in the tissues from the oryzalin experiment identify cells before and after cell division has been suspended. The width and height of all images are ten length units.

the experimental SAM data is that the walls have mechanical properties [18].

Analysis of cell size distributions via Lewis' law reveals small discrepancies between the models and the data

Another geometrical property of the tissue is cell sizes. We used Lewis' law [7] – stating that a linear relationship exists between number of neighbors and areas of cells – to compare the distributions of cell areas from our simulations with the distribution of the SAM (Fig. 4). The experimental data displayed an almost perfect fit to the linear function defined by Lewis' law. The data from the simulations showed a linear dependence between number of neighbors and areas, but the slope deviated slightly from Lewis' law. For example, the two best performing models sofar – ShortestPath|COM and Orthogonal|COM – have a lower slope compared with Lewis' law. This is an indication that the COM positioning mechanism may generate too symmetrically sized daughters, and will hence not allow for as large deviations in cell area as seen in experiments. Partly, this result depends on our definition of a constant maximal cell size in the model (Methods). If the daughter cells are equally sized, the resulting tissues will have cell areas bounded below by a factor one half of this maximal area. But the ShortestPath|COM and Orthogonal|COM models also have narrower distributions of number of neighbors compared with experiments (Tab. 1), which is another indication that the cell divisions of the models are too symmetric. In the plant cell the position of the division plane is guided by the nucleus, which is often located centrally in the cell, although not exactly at the center of mass. Hence, the positioning of the division plane may be at a random position close to the center of mass, which can be interpreted as something in-between our COM and Random positioning mechanisms. Interestingly, this may increase the slope of the cell areas as a function of number of neighbors for the ShortestPath division rule (cf. Figs. 4C and D) while this may not be the case for the Orthogonal division rule (cf. Figs. 4E and F).

The tissue model qualitatively reproduces the behavior of experiment where cell division is impaired

The microtubules of the shoot meristem can be depolymerized by application of oryzalin [19]. In the experiments lack of microtubules resulted in inhibited cell division. Cells still grow and the internal vertex angles converge towards 120°.

We performed a series of simulations without cell division to test our model for this perturbation experiment. First we performed a first series of simulations with the ShortestPath division rule and then, using the tissues from the first series as initial states, we performed a second series of simulations, but this time without cell division. The virtual time of each of these simulations in the second series corresponded to about three generations of cell division. Example images of tissues from simulations before and after suspension of cell division are presented in Fig. 3.

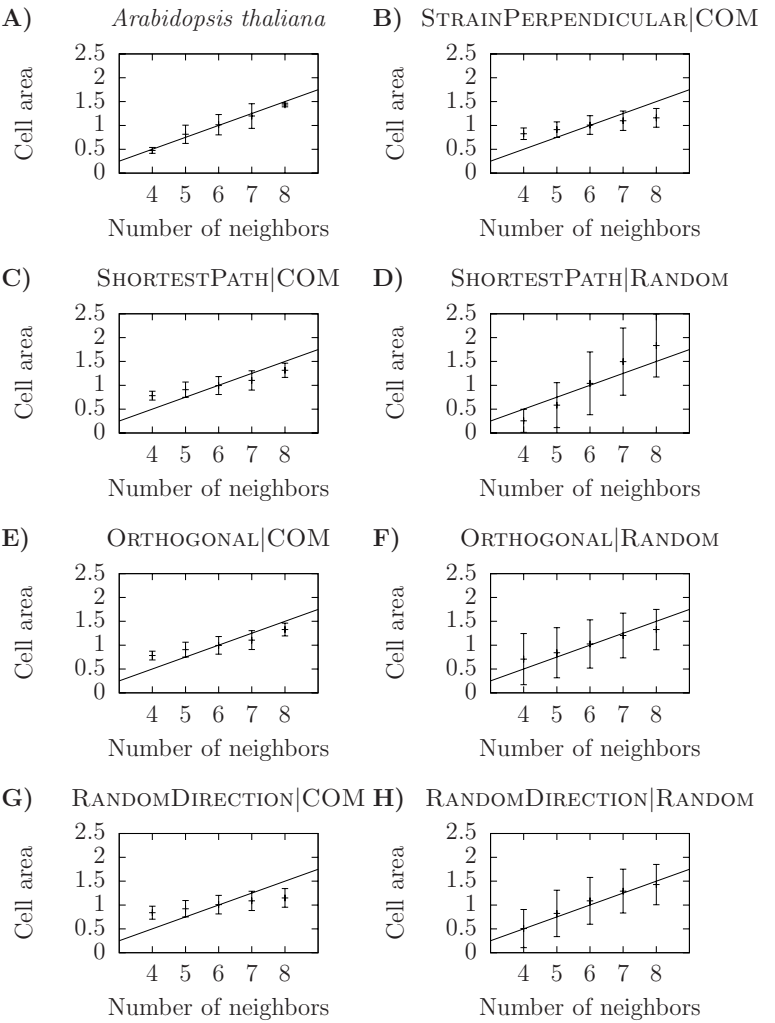

Figure 4: Cell area plotted as a function of number of neighbors for different division rules. Cell areas are normalized such that the average cell area – including all cells of the tissue – is equal to unity. Presented data is average values together with standard deviations. The diagonal line is the relationship: Cell area $= (n-2)/4$, where n is number of neighbors, defining Lewis' law [7].

Distributions of internal vertex angles before and after disabling cell division converge towards 120° for simulated tissues (Fig. 1B). We also compared the shapes of cells before and after disabling cell division in the model (Fig. 2B). Cells in simulated tissue before division is suspended are less symmetrically shaped than cells in the unperturbed experiment, but cells after division is suspended are more symmetrically shaped than cells in the experiment, showing that cell divisions act "against" symmetrically shaped cells.

Conclusions

Already in the 1920s F.T. Lewis noted statistical properties of the topology and geometry of epithelial plant tissue, which later have been seen also in other species. At the same time, the discussion on rules for determining cell division planes in plants has been ongoing since the 19th century. We have used a model of a two-dimensional growing tissue which includes mechanical properties to test several of these rules against experimental data of topological and statistical properties of the epidermal layer of the shoot apical meristem of *Arabidopsis thaliana*.

Our results suggest that epithelial cells in an isotropically growing tissue tend to divide such that the daughter cells are symmetric both in size and in shape, which depends on positioning a new wall close to the center of the cell and to divide along some approximation of a shortest path. It is well known that a shortest path rule for dividing plant cells is not a general rule of generating division directions. Examples exists for which this rule performs badly, *e.g.* in the boundary region between the shoot apical meristem and forming primordium [4]. It was suggested that the microtubules in these regions align in directions following the principal stress direction, and the divisions tended to be along this direction, independent of cell shape. It may very well be that different mechanisms interact and that in regions of isotropic growth, where stresses are isotropic, a shortest path rule might be the result.

We have shown that statistical comparisons are useful when comparing different division rules, but by comparing the models with live imaging data it will be possible to test different division rules at a cellular level. Models – such as the one presented here – will be essential to be able to compare rules not only depending on the cell itself, but also for testing hypotheses based on variables depending on the tissue neighborhood such as growth and mechanical-based mechanisms.

Materials and Methods

The model

The two-dimensional spring-based model is a mechanical model for the epidermal layer of plant tissue. Cells are represented by vertices connected by edges representing cell walls. The edges are treated as mechanical springs and give

the mechanical properties of cell walls. The vertices are treated as being in a viscous medium; their velocities are proportional to the forces acting upon them.

The contribution of forces from walls acting on vertex i is

$$\frac{d\mathbf{v}_i}{dt} = k_w \sum_{j \in \mathcal{V}(i)} \frac{\mathbf{u}_{ij}}{|\mathbf{u}_{ij}|} \left(\frac{|\mathbf{u}_{ij}| - L_{ij}}{L_{ij}} \right), \tag{1}$$

where $\mathbf{v}_i$ is the position of vertex i, k_w is a constant that determines the stiffness of walls, $\mathbf{u}_{ij} = \mathbf{v}_j - \mathbf{v}_i$, and L_{ij} is the resting length of the wall connecting vertices i and j. The summation is over all vertices connected via edges to vertex i.

Cell walls grow under tension. Resting lengths of cell walls are in the model increased as walls are being stretched,

$$\frac{dL_{ij}}{dt} = k_g \Theta \left(\frac{|\mathbf{u}_{ij}| - L_{ij}}{L_{ij}} \right), \tag{2}$$

where k_g is a constant that sets the rate of growth and Θ is the ramp function defined as

$$\Theta(x) = \begin{cases} x & \text{if} \quad x \geq 0 \\ 0 & \text{if} \quad x < 0 \end{cases} . \tag{3}$$

For the StrainPerpendicular division rule the direction of division is parallel to the strain pattern of a cell. We calculate the direction of strain of a cell using circular statistics according to

$$\theta_c = \frac{1}{2} \text{atan} \left(\frac{\sum_{w \in \mathcal{W}(c)} f_w \sin(2\theta_w)}{\sum_{w \in \mathcal{W}(c)} f_w \cos(2\theta_w)} \right), \tag{4}$$

where θ_c is the direction of strain of cell c, $f_w = (|\mathbf{u}_{ij}| - L_{ij})/L_{ij}$ is the magnitude of strain of wall w, and θ_w is the direction of wall w. The summation is over all walls of cell c.

The focus of this work is to model the development of the shoot apical meristem. Turgor pressure and internal growth is represented by a radial force,

$$\frac{d\mathbf{v}_i}{dt} = k_r \mathbf{v}_i, \tag{5}$$

where k_r is a constant which determines the internal growth rate. The model is an approximation of the meristem and the further cells are located from the origin the less accurate is the representation of cells in the epidermal layer. Cells outside a threshold radius, R_t, are therefore removed.

Cell division

A cell is divided into two daughter cells if its area exceeds a threshold value, D_t. The division plane is defined by a spatial position and a direction. The division plane is then the straight path that passes the spatial position in the

Parameter	Standard simulations	Oryzalin simulations
k_w	0.05	0.05
k_g	0.01	0.01
k_r	0.05	0.05
D_t	1.0	-
w_t	0.1	-
R_t	7.0	-

Table 2: The different sets of parameter values that was used in the different types of simulations.

given direction. A division rule determines how the division plane is located (Introduction). At each cell division two new vertices are added to two walls of the mother cells and a new cell wall is added connecting these two vertices. The resting length of the new cell wall is set to be equal to the distance between the two vertices. The two original walls of the mother cell are split into two walls each and the resting lengths of the new walls are set proportionally to respective length such that $L_1^{\text{new}} + L_2^{\text{new}} = L^{\text{old}}$. If the distance between a new vertex and a three-vertex is shorter than a threshold, $w_t L_{ij}$, then the vertex is moved to the threshold position. This measure is taken to avoid four-vertices.

Numerical simulations

A fifth-order Runge-Kutta ODE solver using adaptive stepsize is used for all simulations. The initial states that are used in the simulations are obtained in the following way. First an initial state of one single cell is created. This single cell is then used in a longer simulation and from this simulation 25 snapshots of the tissue are captured and stored to be used as initial states. This process is repeated with 13 different initial single cells represented by regular polygons of 3 to 15 vertices. In total 325 initial states are created and used in the simulations of each division rule. The ShortestPath|COM division rule is used in the simulations to generate initial states as the division rule has in previous studies proved itself to generate plant-like tissues [18].

The average numbers of cells (with standard deviations) at one snapshot in simulated tissues were; 237±45 (ShortestPath|COM), 437±66 (ShortestPath|COM), 231±43 (RandomDirection|COM), 310±48 (RandomDirection|Random), 235±42 (Orthogonal|COM), and 282±46 (Orthogonal|Random), 218±39 (StrainPerpendicular|COM). Cells on the boundary of the tissue were neglected.

Parameter values are presented in Tab. 2. We have performed a robustness analysis by performing series of simulations with parameter values perturbed by an order of magnitude. The analysis showed that the results are robust to these parameter perturbations (data not shown).

Experimental data

We compare simulations of the model with experimental data from *Arabidopsis thaliana*. The experimental data consists of a tissue with 110 cells and is taken from [18].

Data analysis

After each simulation data is gathered from the resulting tissue. There are three types of data that are gathered; number of neighbors, internal vertex angles, and a measurement of cell shape. While gathering data we neglect cells at the boundary since such cells can be affected by the boundary condition.

The measurement of cell shape is here defined as the ratio between cell area and the total length of cell walls squared. The numerical value of this measurement ranges from zero for cells without area, to $(4\pi)^{-1}$ for circular cells.

We introduced a fitness test to quantify how well a simulated tissue reproduces the distributions of number of neighbors from experiments. The fitness is defined as

$$\text{Fitness} = \left[\sum_i (n_i - n_i^*)^2\right]^{1/2}, \tag{6}$$

where n_i is the fraction of cells in the tissue with i neighbors, and n_i^* is the corresponding fraction measured from experimental data.

Acknowledgments

This work was in part supported by the Swedish Research Council. We thank Pawel Krupinski for valuable discussions and feedback on the manuscript.

Author Contributions

Conceived and designed the experiments (PS, HJ). Performed the experiments (PS). Analyzed the data (PS, HJ). Wrote the paper (PS, HJ).

References

[1] Martin P, Lewis J (1992) Actin cables and epidermal movement in embryonic wound healing. Nature 360: 179–83.

[2] Engler AJ, Sen S, Sweeney HL, Discher DE (2006) Matrix elasticity directs stem cell lineage specification. Cell 126: 677–89.

[3] Dumais J (2007) Can mechanics control pattern formation in plants? Curr Opin Plant Biol 10: 58–62.

[4] Hamant O, Heisler MG, Jönsson H, Krupinski P, Uyttewaal M, et al. (2008) Developmental patterning by mechanical signals in arabidopsis. Science 322: 1650–5.

[5] Smith LG (2001) Plant cell division: building walls in the right places. Nat Rev Mol Cell Biol 2: 33–9.

[6] Lewis FT (1926) The effect of cell division on the shape and size of hexagonal cells. Anatomical Records 33: 331—335.

[7] Lewis FT (1928) The correlation between cell division and trhe shapes and sizes of prismatic cells in the epidermis of cucumis. Anatomical Records 38: 341—376.

[8] Gibson MC, Patel AB, Nagpal R, Perrimon N (2006) The emergence of geometric order in proliferating metazoan epithelia. Nature 442: 1038–41.

[9] Kwiatkowska D, Dumais J (2003) Growth and morphogenesis at the vegetative shoot apex of anagallis arvensis l. J Exp Bot 54: 1585–95.

[10] Reddy GV, Heisler MG, Ehrhardt DW, Meyerowitz EM (2004) Real-time lineage analysis reveals oriented cell divisions associated with morphogenesis at the shoot apex of arabidopsis thaliana. Development 131: 4225–37.

[11] Hofmeister W (1863) Zusatze und berichtigungen zu den 1851 veröffentlichen untersuchungen der entwicklung höherer kryptogamen. Jahrbucher für Wissenschaft und Botanik 3: 259—293.

[12] Sachs J (1878) Über die anordnung der zellen in jüngsten pflanzentheilen. Arb bot Inst Wurzburg 2: 46.

[13] Errara L (1888) Über zellformen und siefenblasen. Botanisches Centralblatt 34: 395—399.

[14] Thompson D (1942) On Growth and Form. Dover Publications, New York.

[15] Grandjean O, Vernoux T, Laufs P, Belcram K, Mizukami Y, et al. (2004) In vivo analysis of cell division, cell growth, and differentiation at the shoot apical meristem in arabidopsis. Plant Cell 16: 74–87.

[16] Fischer K, Schopfer P (1998) Physical strain-mediated microtubule reorientation in the epidermis of gravitropically or phototropically stimulated maize coleoptiles. Plant J 15: 119–23.

[17] Patel AB, Gibson WT, Gibson MC, Nagpal R (2009) Modeling and inferring cleavage patterns in proliferating epithelia. PLoS Comput Biol 5: e1000412.

[18] Sahlin P, Hamant O, Jönsson H (2009) Statistical properties of cell topology and geometry in a tissue-growth model. In: Zhou J, editor, Complex 2009, LNICST 4. pp. 971–979.

[19] Corson F, Hamant O, Bohn S, Traas J, Boudaoud A, et al. (2009) Turning a plant tissue into a living cell froth through isotropic growth. Proc Natl Acad Sci USA 106: 8453–8.

Paper V

Journal of Theoretical Biology 258 (2009) 60–70

Contents lists available at ScienceDirect

Journal of Theoretical Biology

journal homepage: www.elsevier.com/locate/yjtbi

Regulated transport as a mechanism for pattern generation: Capabilities for phyllotaxis and beyond

Patrik Sahlin, Bo Söderberg, Henrik Jönsson *

Computational Biology and Biological Physics, Department of Theoretical Physics, Lund University, Sölvegatan 14A, SE-223 62 Lund, Sweden

ARTICLE INFO

Article history:
Received 23 June 2008
Received in revised form
13 January 2009
Accepted 22 January 2009
Available online 31 January 2009

Keywords:
Auxin
PIN1
AUX1
Plant development
Developmental model

ABSTRACT

Large-scale pattern formation is a frequently occurring phenomenon in biological organisms, and several local interaction rules for generating such patterns have been suggested. A mechanism driven by feedback between the plant hormone auxin and its polarly localized transport mediator PINFORMED1 has been proposed as a model for phyllotactic patterns in plants. It has been shown to agree with current biological experiments at a molecular level as well as with respect to the resulting patterns. We present a thorough investigation of variants of models based on auxin-regulated polarized transport and use analytical and numerical tools to derive requirements for these models to drive spontaneous pattern formation. We find that auxin concentrations in neighboring cells can feed back either on exocytosis or endocytosis and still produce patterns. In agreement with mutant experiments, the active cellular efflux is shown to be more important for pattern capabilities as compared to active influx. We also find that the feedback must originate from neighboring cells rather than from neighboring walls and that intracellular competition for the transport mediator is required for patterning. The importance of model parameters is investigated, especially regarding robustness to perturbations of experimentally estimated parameter values. Finally, the regulated transport mechanism is shown to be able to generate Turing patterns of various types.

© 2009 Elsevier Ltd. All rights reserved.

1. Introduction

In nature, spontaneous pattern formation is a common and important result from dynamic interactions. Several mechanisms have been proposed for generating regular patterns where the reaction–diffusion mechanism has proven to be capable of generating patterns of different forms such as peaks and stripes. The idea of reactions of morphogens within cells combined with different molecular diffusion rates as a main regulator of biological development was introduced by Turing (1952) already in the 1950s. Gierer and Meinhardt (1972) also discussed the mechanism in terms of local activation and long-range inhibition.

One of the most studied and intriguing patterns found in nature is the regular placement of plant organs resulting in phyllotactic patterns. Leaf and flower primordia are initiated at the flank of the shoot leading to patterns of different whorled or spiral symmetries. Especially the spiral pattern has been of interest in many studies for hundreds of years with its connection to the golden mean and the Fibonacci sequence (Adler et al., 1997; Jean and Barabé, 1998). Mathematical analysis has shown that these patterns can naturally occur as a consequence of initiation on a ring, continuous spatial growth of the system, and a regular spacing mechanism (Douady and Couder, 1992; Mitchison, 1977; Smith et al., 2006a). Several mechanisms have been proposed for the spacing mechanism, using mechanical as well as molecular arguments. A purely mechanical argument relies on the outer layer of cells being seen as a two-dimensional continuous sheet, which can buckle in a phyllotactic pattern due to compressive stresses (Green et al., 1998; Shipman and Newell, 2005). It represents a global view where an optimal configuration results in patterning of the static shoot (or other organ). The molecular view mostly has included growth and an inhibition from earlier primordia where for example reaction–diffusion mechanisms have been proposed (Chapman and Perry, 1987; Meinhardt, 1982). Recently, also combinations of molecular and mechanical mechanisms have been investigated in a continuous model (Newell et al., 2007).

Experimental data have highlighted the importance of the plant hormone auxin in the initiation of new primordia, as its concentration peaks at the positions where new primordia form (Benkova et al., 2003; Heisler et al., 2005; Smith et al., 2006b). Reducing the auxin transport leads to failure of phyllotaxis, which pinpoints the importance of transport in the process. Especially the PINFORMED1 (PIN1) membrane protein, which mediates cellular efflux of auxin, is integral in the patterning process since its loss-of-function mutant displays no organs in the inflorescence

* Corresponding author. Tel.: +46 46 222 0663; fax: +46 46 222 9686.
E-mail address: henrik@thep.lu.se (H. Jönsson).

0022-5193/$ - see front matter © 2009 Elsevier Ltd. All rights reserved.
doi:10.1016/j.jtbi.2009.01.019

(Okada et al., 1991; Reinhardt et al., 2000). PIN1, which cycles between cytosol and membrane compartments (Geldner et al., 2001), is polarized towards sites of new primordia and away from older, and hence can transport auxin against a concentration gradient (Barbier de Ruille et al., 2006; Heisler et al., 2005; Reinhardt et al., 2003). Single mutants of auxin influx mediators have shown less phyllotactic phenotypes, and no apparent polarization is seen in the shoot cells. Recently, quadruple mutants of the AUX1/LAX influx mediators showed irregularities in the phyllotactic pattern, although the organ formation was not completely stopped (Bainbridge et al., 2008).

The underlying mechanism for creating polarized PIN1 cycling is to a large extent unknown, and it is still unsettled whether a single mechanism is acting throughout different plant tissues. Interestingly, a hypothesis with auxin itself feeding back to the PIN1 polarization can result in patterning dynamics. If auxin in neighboring cells attracts PIN1 to the cell membrane in respective direction, it can be enough for generating a pattern with a parameter dependent wavelength, i.e. one of the requirements for phyllotactic patterning (Jönsson et al., 2006; Smith et al., 2006b). In Jönsson et al. (2006), it was shown that the relative strengths of the active PIN1 mediated transport and the passive diffusion-like transport is a main determinant of the possibility of patterning and of the wavelength of the patterns. Another proposed mechanism for generating patterns in plants is that of auxin-fluxes feeding back to active efflux, which mainly have been used to describe venation, e.g. Feugier et al. (2005), Fujita and Mochizuki (2006), Mitchison (1980), and Sachs (1981).

In this work we extend the analysis of the auxin-concentration feedback model, investigating more detailed requirements for pattern formation from this regulated transport mechanism. We pursue the relation between the feedback mechanism and transport mechanisms, where also cellular influx is included. We demonstrate the mechanism's generality with dynamics very similar to reaction–diffusion models, where patterns other than peaks can be formed. We also thoroughly investigate the patterning behavior in the parameter region surrounding experimentally estimated values, and especially investigate its robustness to single and multiple parameter perturbations.

2. Materials and methods

2.1. The model

Although the model presented in this paper may be involved in various pattern mechanisms in nature, it was initially inspired by plant phyllotaxis. Hence, the model is introduced in this context, and based on experimental knowledge of auxin transport from earlier work. The main mechanisms in the model are the passive and active auxin transport, and the mechanisms for localizing transport mediators on cell–wall membranes. We also introduce generalizations and simplifications of the model used in our analysis and simulations.

2.1.1. Auxin transport

In plant phyllotaxis, auxin is assumed to act as a morphogen, directed to the sites of primordia formation (Benkova et al., 2003; Heisler et al., 2005; Reinhardt et al., 2003). The auxin transport model is based on the chemiosmotic theory (Rubery and Sheldrake, 1974; Raven, 1975) where auxin dissociation leads to an anion (a^-) and a protonated (aH) form (Fig. 1A). The fractions of auxin in its two states are assumed to be in equilibrium in each compartment, where different pH values in the cytosol and wall compartments result in the fractions $f_{a^-}^{cell}$, f_{aH}^{cell}, $f_{a^-}^{wall}$, and f_{aH}^{wall}. While the protonated form of auxin can passively cross the cell–wall membrane, the anion cannot and it is actively transported across the membrane mediated by PIN1 for cell efflux, and AUX1 for cell influx. The passive transport is assumed to be unsaturated, while the PIN1/AUX1 mediated active transport can be saturated. The auxin flux from a cell compartment (i) to a wall compartment (ij) is described by

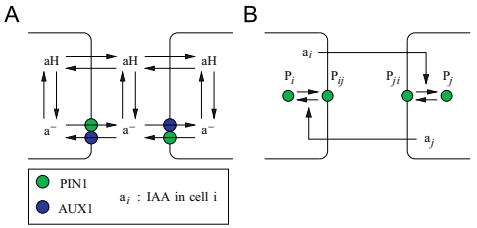

Fig. 1. Illustration of the model. (A) Transport of auxin. (B) The hypothesis that leads to pattern generating dynamics.

$$\begin{aligned} J_{a,i\to ij} = {} & p_{aH}(f_{aH}^{cell}a_i - f_{aH}^{wall}a_{ij}) \\ & + p_{PIN}W_{ij}P_{ij}\left(N(\Phi)\frac{f_{a^-}^{cell}a_i}{K_P + f_{a^-}^{cell}a_i} - N(-\Phi)\frac{f_{a^-}^{wall}a_{ij}}{K_P + f_{a^-}^{wall}a_{ij}}\right) \\ & + p_{AUX}W_{ij}A_{ij}\left(N(-\Phi)\frac{f_{a^-}^{cell}a_i}{K_A + f_{a^-}^{cell}a_i} - N(\Phi)\frac{f_{a^-}^{wall}a_{ij}}{K_A + f_{a^-}^{wall}a_{ij}}\right), \end{aligned} \quad (1)$$

where a_i is the concentration of auxin in the cytosol compartment in cell i and a_{ij} is the concentration of auxin in the wall compartment located between cells i and j (Kramer, 2004; Swarup et al., 2005; Jönsson et al., 2006; Heisler and Jönsson, 2006). P_{ij} and A_{ij} are the surface densities of PIN1 and AUX1 on the membrane compartment in cell i facing cell j. p_{aH}, p_{PIN}, and p_{AUX} are permeabilities for the three different means of transport. K_P and K_A are constants setting the levels of saturation. W_{ij} is the ratio between the area of the membrane in cell compartment i facing wall compartment ij and the volume of cell compartment i.

$N(\Phi)$ is defined as

$$N(\Phi) \equiv \frac{\Phi e^{\Phi}}{e^{\Phi} - 1} \quad \text{where } \Phi = \frac{zVF}{RT}, \quad (2)$$

and represents the electrochemical factor for transport across a membrane potential V where z is the valence of the ion, R is the gas constant, F is Faraday's constant, and T is the temperature. Since the ratio $N(\Phi)/N(-\Phi)$ is large, PIN1 (AUX1) acts as an efflux (influx) transport mediator. In addition to the cell–wall transport apoplastic (wall–wall) diffusion also occurs, although we disregard this in our model (see Section 2.2).

We will do a generalized analysis and will not restrict ourselves to Eq. (1) but rather consider a general functional form of the mediated auxin transport described by

$$\begin{aligned} J_{a,i\to ij} = {} & p_{aH}(f_{aH}^{cell}a_i - f_{aH}^{wall}a_{ij}) + p_{PIN}W_{ij}P_{ij}N(\Phi)h_A(a_i) \\ & - p_{AUX}W_{ij}A_{ij}N(\Phi)h_A(a_{ij}), \end{aligned} \quad (3)$$

where $h(a_i)$ is an auxin-dependent function for mediated efflux and $h_A(a_{ij})$ is the corresponding function for influx. Note that we disregard PIN1-mediated transport into the cells and AUX1-mediated transport out of the cells.

2.1.2. Protein cycling

In the model the proteins mediating auxin transport are assumed to cycle between cytosol and membrane compartments (Fig. 1B, Geldner et al., 2001). The influx mediator AUX1 is assumed to localize symmetrically on all membranes while the

membrane localization of the efflux mediator PIN1 is dependent on auxin in neighboring cells. In accordance with previous models (Heisler and Jönsson, 2006), cycling of PIN1 and AUX1 between the cytosol compartment i and the membrane compartment ij is described by

$$J_{A,i\to ij} = k_{A1}W_{ij}^{-1}A_i - k_{A2}A_{ij}, \tag{4}$$

$$J_{P,i\to ij} = k_{P1}W_{ij}^{-1}\left((1-c_P) + c_P\frac{a_j^n}{K_H^n + a_j^n}\right)P_i - k_{P2}P_{ij}. \tag{5}$$

A_i and P_i are the concentrations of AUX1 and PIN1 in the cytosol compartment in cell i, k_{A1}, k_{A2}, k_{P1}, and k_{P2} are AUX1 and PIN1 cycling rates, K_H and n sets the saturation of PIN1-cycling, and c_P sets the balance between symmetric and auxin-dependent cycling of PIN1. We will look at a generalized form for PIN1 cycling and define the functions f_{exo} and f_{endo} for the functional forms of the auxin dependence on exocytosis and endocytosis, respectively, leading to

$$J_{P,i\to ij} = W_{ij}^{-1}f_{exo}(a_j)P_i - f_{endo}(a_j)P_{ij}. \tag{6}$$

2.1.3. Production and degradation

This paper focuses on the regulated transport aspects of the model, and thus we use a somewhat simplistic description of production and degradation. We introduce constant homogeneous PIN1 and AUX1 concentrations and constant auxin production and degradation described by

$$\frac{da_i}{dt} = c_a - d_a a_i + \text{ transport contributions}, \tag{7}$$

for each cell i, where c_a is the constant rate of production, and d_a is the rate of degradation. It has been shown that auxin-regulated PIN1 and AUX1 production influences the stability of the patterns (Heisler and Jönsson, 2006; Merks et al., 2007), which will be discussed in Section 3.1.4.

2.2. Model simplifications

Three assumptions are made that simplify the analysis of the model and better illuminate the results. The first assumption is that PIN1- and AUX1-cycling between the cytosol and the membranes is fast compared to auxin dynamics (Jönsson et al., 2006; Heisler and Jönsson, 2006). With this assumption we get the fixed point surface densities of PIN1 (P_{ij}^*) and AUX1 (A_{ij}^*) by setting $J_{A,i\to ij}$ and $J_{P,i\to ij}$ in Eqs. (4) and (6) to zero. The fixed point surface densities of PIN1 are

$$P_{ij}^* = \mathscr{P}_{ij}W_{ij}^{-1}P_{total} \quad \text{where } \mathscr{P}_{ij} = \frac{f(a_j)}{1+\sum_{k\in\mathscr{N}_i}f(a_k)}$$

and

$$f(a_j) = \frac{f_{exo}(a_j)}{f_{endo}(a_j)} \tag{8}$$

and the fixed point surface densities of AUX1 are

$$A_{ij}^* = \mathscr{A}_{ij}W_{ij}^{-1}A_{total} \quad \text{where } \mathscr{A}_{ij} = \frac{\frac{k_{A1}}{k_{A2}}}{1+\sum_{k\in\mathscr{N}_i}\frac{k_{A1}}{k_{A2}}}. \tag{9}$$

P_{total} (A_{total}) is the total concentration of PIN1 (AUX1) in the cell compartment. The summation is done over the set of indices of neighboring cells ($\mathscr{N}_i$). The second assumption is to disregard apoplastic diffusion. Hence, the question of the importance of the apoplastic diffusion cannot be addressed. Our comparisons between the simplified model and previous efforts (Heisler and Jönsson, 2006) do not suggest that this is a problem, at least at experimentally estimated parameter values. A discussion on the importance of apoplastic diffusion in plant tissue can be found in Kramer (2006). Finally, we assume that all cells (and walls) are of equal size and have the same number of neighbors. Hence $W_{ij} = W$ and $\mathscr{A}_{ij} = \mathscr{A}$ for all i and j.

The fixed point expressions are used for the surface densities of PIN1 and AUX1 in Eq. (3). Taken together, the model equations become

$$\begin{aligned}\frac{da_i}{dt} = {} & W\sum_{k\in\mathscr{N}_i}(p_{aH}f_{aH}^{wall}a_{ij} - p_{aH}f_{aH}^{cell}a_i)\\ & - W\sum_{k\in\mathscr{N}_i}p_{PIN}N(\Phi)\mathscr{P}_{ik}P_{total}h(a_i)\\ & + W\sum_{k\in\mathscr{N}_i}p_{AUX}N(\Phi)\mathscr{A}A_{total}h_A(a_{ik}) + c_a - d_a a_i,\end{aligned} \tag{10}$$

$$\begin{aligned}\frac{da_{ij}}{dt} = {} & W\frac{V_{cell}}{V_{wall}}(p_{aH}f_{aH}^{cell}(a_i+a_j) - 2p_{aH}f_{aH}^{wall}a_{ij}\\ & + p_{PIN}N(\Phi)\mathscr{P}_{ij}P_{total}h(a_i) + p_{PIN}N(\Phi)\mathscr{P}_{ji}P_{total}h(a_j)\\ & - p_{AUX}N(\Phi)\mathscr{A}A_{total}h_A(a_{ij}) - p_{AUX}N(\Phi)\mathscr{A}A_{total}h_A(a_{ij})),\end{aligned} \tag{11}$$

which can be rewritten as

$$\begin{aligned}\frac{da_i}{d\tau} = {} & \sum_{k\in\mathscr{N}_i}(d_2 b_{ik} - Da_i) - \sum_{k\in\mathscr{N}_i}\mathscr{P}_{ik}P_{total}h(a_i)\\ & + \sum_{k\in\mathscr{N}_i}G\mathscr{A}A_{total}h_A\left(\frac{V_{cell}}{V_{wall}}b_{ik}\right) + C_a - \delta_a a_i,\end{aligned} \tag{12}$$

$$\begin{aligned}\frac{db_{ij}}{d\tau} = {} & D(a_i+a_j) - 2d_2 b_{ij} + \mathscr{P}_{ij}P_{total}h(a_i) + \mathscr{P}_{ji}P_{total}h(a_j)\\ & - G\mathscr{A}A_{total}h_A\left(\frac{V_{cell}}{V_{wall}}b_{ij}\right) - G\mathscr{A}A_{total}h_A\left(\frac{V_{cell}}{V_{wall}}b_{ij}\right),\end{aligned} \tag{13}$$

where $b_{ij} = (V_{wall}/V_{cell})a_{ij}$ is a rescaled auxin concentration in the wall and τ is a dimensionless time parameter. V_{cell} and V_{wall} are the volumes of the cell and wall compartments, respectively. Parameters D and d_2 can be interpreted as ratios between rates of passive diffusion-like transport and the active PIN1-dependent transport. G is the ratio of AUX and PIN permeabilities and C_a and δ_a are rescaled auxin production and degradation rates, respectively. The exact parameter definitions and values can be found in Table 1.

Table 1
Parameter values used for the unperturbed model.

Parameter	Value	Unit
$D = \frac{p_{aH}f_{aH}^{cell}}{p_{PIN}N(\Phi)}$	0.00035	–
$d_2 = \frac{p_{aH}f_{aH}^{wall}V_{cell}}{p_{PIN}N(\Phi)V_{wall}}$	–	–
$k_1 = \frac{k_{p_1}}{k_{p_2}}(1-c_p)$	0.20	–
$k_2 = \frac{k_{p_1}}{k_{p_2}}c_p$	1.8	–
K_H	1.0	μM
n	1.0	-
$K_M = K_P/f_{a=}^{cell}$	1.0	μM
$C_a = \frac{c_a}{p_{PIN}N(\Phi)W}$	0.0012	μM
$\delta_a = \frac{d_a}{p_{PIN}N(\Phi)W}$	0.0012	–
$G = \frac{p_{AUX}}{p_{PIN}}$	–	–
$\tau = tp_{PIN}N(\Phi)W$	–	–
W	0.2	μm^{-1}

The parameter values are estimates from experiments where available, and taken from previous models (Kramer, 2004; Swarup et al., 2005; Jönsson et al., 2006; Heisler and Jönsson, 2006). Values are not given for parameters without influence on our results.

2.3. Analysis methodology

We consider a model on a regular lattice. Each cell (i) is assumed to be located on an associated lattice point $\mathbf{x}_i$. It has an even number m of nearest neighbours. We denote by $\mathbf{e}_p$ the relative position vector to the pth neighbor cell, which has the label $j=j_{pi}$ and hence the location $\mathbf{x}_j=\mathbf{x}_i+\mathbf{e}_p$. j_{pi} represents the index j of the pth neighbor cell of cell i.

Between each neighbor pair i,j there is a wall compartment (ij) located at the mid-point $\mathbf{x}_{ij}=(\mathbf{x}_i+\mathbf{x}_j)/2=\mathbf{x}_i+\mathbf{e}_p/2=\mathbf{x}_j-\mathbf{e}_p/2$.

The dynamics is linearized by considering small deviations $(a_i,b_{ij})=(a+\varepsilon_i,b+\varepsilon_{ij})$ from the homogeneous fixed point concentrations (a,b) obtained by requiring the right-hand sides of Eqs. (12) and (13) to vanish. Linear versions of Eqs. (12) and (13) then result by neglecting terms higher than linear in the ε's, yielding

$$\frac{d\varepsilon_i}{d\tau}=-\left(\delta_a+\sum_{k\in\mathcal{N}_i}(D+E_1)\right)\varepsilon_i-E_2\sum_{k\in\mathcal{N}_i}\varepsilon_k+D_2\sum_{k\in\mathcal{N}_i}\varepsilon_{ik}, \tag{14}$$

$$\frac{d\varepsilon_{ij}}{d\tau}=(D+E_1+E_2+mE_3)(\varepsilon_i+\varepsilon_j)-E_3\left(\sum_{l\in\mathcal{N}_i}\varepsilon_l+\sum_{l\in\mathcal{N}_j}\varepsilon_l\right)-2D_2\varepsilon_{ij}, \tag{15}$$

where $D_2=d_2+G\mathscr{A}A_{\text{total}}h'_A(a)V_{\text{cell}}/V_{\text{wall}}$ and

$$E_1=\frac{f(a)P_{\text{total}}h'(a)}{(1+mf(a))},\quad E_2=\frac{f'(a)P_{\text{total}}h(a)}{(1+mf(a))^2}\quad\text{and}$$

$$E_3=\frac{f(a)f'(a)P_{\text{total}}h(a)}{(1+mf(a))^2}, \tag{16}$$

while f' and h' are the derivatives (with respect to auxin concentration) of f and h, respectively.

The analysis of the solution to the equation system in Eqs. (14) and (15) is easier performed if transformed into Fourier space. The auxin fluctuations in the cells and walls are transformed according to

$$\varepsilon_{\mathbf{k}}=\frac{1}{2\pi}\sum_i\varepsilon_i e^{-i\mathbf{k}\cdot\mathbf{x}_i}, \tag{17}$$

$$\varepsilon_{\mathbf{k},p}=\frac{1}{2\pi}\sum_i\varepsilon_{i,j_{pi}}e^{-i\mathbf{k}\cdot\mathbf{x}_{ij_{pi}}}, \tag{18}$$

leading to the system of ODEs

$$\dot{\varepsilon}_{\mathbf{k}}=-(\delta_a+m(D+E_1+E_2S(\mathbf{k})))\varepsilon_{\mathbf{k}}+2D_2\sum_{p=1}^{m/2}\cos\left(\frac{1}{2}\mathbf{k}\cdot\mathbf{e}_p\right)\varepsilon_{\mathbf{k},p}, \tag{19}$$

$$\dot{\varepsilon}_{\mathbf{k},p}=2\cos\left(\frac{1}{2}\mathbf{k}\cdot\mathbf{e}_p\right)(D+E_1+E_2+mE_3(1-S(\mathbf{k})))\varepsilon_{\mathbf{k}}-2D_2\varepsilon_{\mathbf{k},p}, \tag{20}$$

where $S(\mathbf{k})$ denotes the "lattice form factor"

$$S(\mathbf{k})=\frac{1}{m}\sum_{p=1}^{m}e^{i\mathbf{k}\cdot\mathbf{e}_p}=\frac{2}{m}\sum_{p=1}^{m/2}\cos(\mathbf{k}\cdot\mathbf{e}_p), \tag{21}$$

obeying $|S(\mathbf{k})|\leqslant 1$.

By introducing $\sigma_{\mathbf{k}}$ defined as

$$\sigma_{\mathbf{k}}\equiv\frac{2}{m}\sum_{p=1}^{m/2}\cos\left(\frac{1}{2}\mathbf{k}\cdot\mathbf{e}_p\right)\varepsilon_{\mathbf{k},p}, \tag{22}$$

the non-trivial part of Eqs. (19) and (20) simplifies to

$$\begin{bmatrix}\dot{\varepsilon}_{\mathbf{k}}\\ \dot{\sigma}_{\mathbf{k}}\end{bmatrix}=\begin{bmatrix}-(D_A+m(D+E_1+E_2S(\mathbf{k})))&mD_2\\ (S(\mathbf{k})+1)(D+E_1+E_2+mE_3(1-S(\mathbf{k})))&-2D_2\end{bmatrix}\begin{bmatrix}\varepsilon_{\mathbf{k}}\\ \sigma_{\mathbf{k}}\end{bmatrix}. \tag{23}$$

(The remaining part trivially decays as $e^{-2D_2\tau}$.) The matrix in Eq. (23) can be diagonalized to yield a pair of eigenvalues $\lambda_{\mathbf{k}1}$, $\lambda_{\mathbf{k}2}$, in addition to the trivial eigenvalue $\lambda_{\mathbf{k}0}=-2D_2$. For the perturbations of auxin concentrations in cell compartments the final solution to the linearized differential equation then becomes

$$\varepsilon_i(\tau)=\sum_{\mathbf{k}\alpha}c_{\mathbf{k}\alpha}e^{\lambda_{\mathbf{k}\alpha}\tau}\cos(\mathbf{k}\cdot\mathbf{x}_i+\delta_{\mathbf{k}\alpha}), \tag{24}$$

where $c_{\mathbf{k}\alpha}$ and $\delta_{\mathbf{k}\alpha}$ are scalar functions determined by the initial conditions. If at least one (real part of an) eigenvalue for some wave vector $\mathbf{k}$ is positive then the homogeneous fixed point is unstable and we expect patterns with a related spatial wavelength to emerge.

2.4. Numerical simulations

All simulations have been done by using in-house developed software utilizing a 5th order Runge–Kutta numerical ODE-solver (Press et al., 1992). Parameter values for the models used in different simulations and calculations are presented in Table 1. For the numerical simulations we used a model assuming fast auxin dynamics. The auxin concentrations in the wall compartments are integrated out from the equations. Fixed point expressions for the wall concentrations of auxin are substituted into Eq. (3). This assumption leads to a model for auxin concentrations in cell compartments described by a system of non-linear ordinary differential equations.

$$\frac{da_i}{d\tau}=\frac{1}{2}\sum_{k\in\mathcal{N}_i}D(a_k-a_i)+\frac{1}{2}\sum_{k\in\mathcal{N}_i}(\mathscr{P}_{ki}P_{\text{total}}h(a_k)-\mathscr{P}_{ik}P_{\text{total}}h(a_i))+C_a-\delta_a a_i, \tag{25}$$

where

$$h(a_i)=\frac{a_i}{K_M+a_i}\quad\text{and}\quad f(a_i)=k_1+k_2\frac{a_i^n}{K_H^n+a_i^n}. \tag{26}$$

The simplified cell–cell model is analyzed in Appendix A. The stability requirements are identical to those of the cell–wall based model.

3. Results

3.1. The feedback model is capable of spontaneous pattern generation with parameter dependent characteristics

The model presented in Eqs. (12) and (13) (or Eq. 25) is capable of spontaneous pattern generation. When experimental estimates for the transport parameters are used, peaks with distances of about 5–7 cells are generated (Fig. 2A). A similar behavior was also described in Heisler and Jönsson (2006) for the non-simplified model including wall compartments and apoplastic diffusion. By varying parameter values it is possible to change the wavelength of the pattern (e.g. Fig. 2B). More generally, it is of interest to see the model's capability of generating patterns other than peaks. As examples of this, additional patterns are presented in Fig. 2C and D, showing stripes and reentrant peaks, the latter being patterns with low-concentration spots. In Section 3.2 we will discuss parameter regions leading to different patterns.

By investigating the characteristic equation for the system described by Eq. (23) we extracted requirements for the model to generate patterns. The characteristic equation yields an eigenvalue with a positive real part and a non-trivial solution if and only if the inequalities

$$\frac{(D-(E_2+2mE_3-E_1))^2}{8E_3}>\delta_a \tag{27}$$

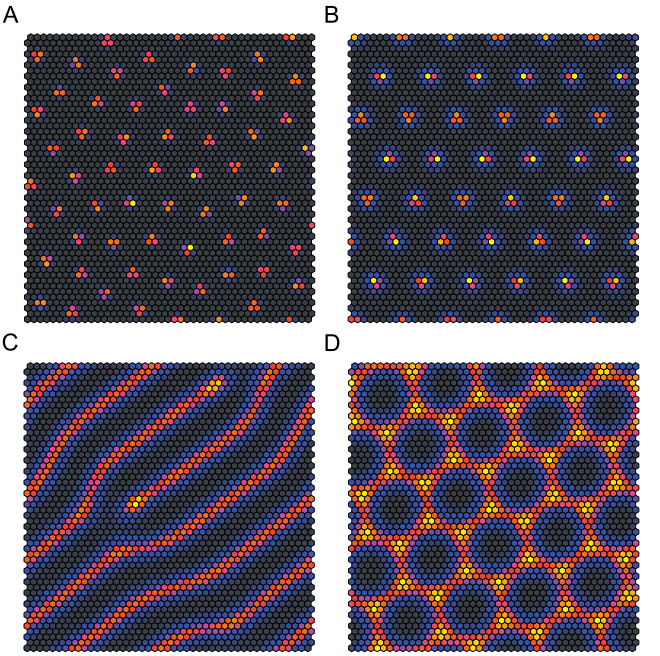

Fig. 2. Model simulations. (A) Using parameter values from experimental estimates of auxin transport the model generates peaks with a distance of around 5–7 cells. (B) Changing parameter values changes the average distance between peaks. In this case the value of k_2 has been changed to 0.90 and the average distance between peaks has increased. Other patterns than peaks can be generated by adjusting parameter values, for example (C) stripes ($K_M = 1.7$) or (D) a reentrant peak pattern ($K_H = 0.6$).

and

$$D < E_2 + 2mE_3 - E_1 \tag{28}$$

are true, which can be found by investigating the signs of the trace and the determinant from Eq. (23). We can directly see that the passive auxin transport from cell to wall as well as the auxin degradation must not be too large for patterns to form.

To further evaluate the generated patterns, we investigated how the typical distances between peaks evolve as parameter values are changed. This was done for cells located on a two-dimensional hexagonal lattice. From Eqs. (21) and (A.3) we see that for such a lattice the wave vectors $\mathbf{k} = (k_x, k_y)$ corresponding to the greatest (degenerate) eigenvalue fulfill

$$\frac{1}{3}\left[2\cos\left(\frac{k_x}{2}\right)\cos\left(\frac{\sqrt{3}k_y}{2}\right) + \cos(k_x)\right] = S^*. \tag{29}$$

Fig. 3A displays the function in Eq. (29) plotted with contour curves. For small wave numbers the hexagonal structure of the lattice has no visual effect while large wave numbers conform to the structure. Fig. 3B presents a numerical Fourier transform of a pattern generated using the parameter values from Table 1. The analytic prediction of the dominating wave vectors is marked in the figure showing a good match between the (linear) analysis and the final pattern.

3.1.1. *Mediated efflux is more important than influx for pattern capabilities*

Experimental results have indicated that efflux mediators, in particular PIN1, are more important than influx mediators, especially AUX1 (Reinhardt et al., 2003; Bainbridge et al., 2008) for organ initiation. From the model's capability to generate patterns from perturbations of the homogeneous fixed point, we can see that PIN1 enters Eqs. (27) and (28) such that higher concentration levels of PIN1 increase the possibility of pattern generation. Too low PIN1 levels will lead to no patterns. On the other hand the requirements in Eqs. (27) and (28) are independent on AUX1 concentration levels. Thus AUX1 does not contribute at all to the model's capability of generating patterns.

3.1.2. *Feedback through reduced endocytosis generates patterns*

The polarized transport models presented in previous works have focused on the hypothesis of PIN1 exocytosis (cycling rate from cytosol compartments to the wall membrane) regulated by auxin in neighboring cells. Here we look at a more general feedback model where either exocytosis or endocytosis (cycling from wall membrane to cytosol compartments) is regulated by auxin in neighboring cells. A reason for this generalization is that auxin has been shown to be able to affect PIN1 endocytosis in plant tissue (Paciorek et al., 2005). Assuming fast PIN1 cycling the equilibrium surface density of PIN1 on the membrane (P_{ij}^*) is given by Eq. (8) where the feedback on exocytosis and endocytosis is

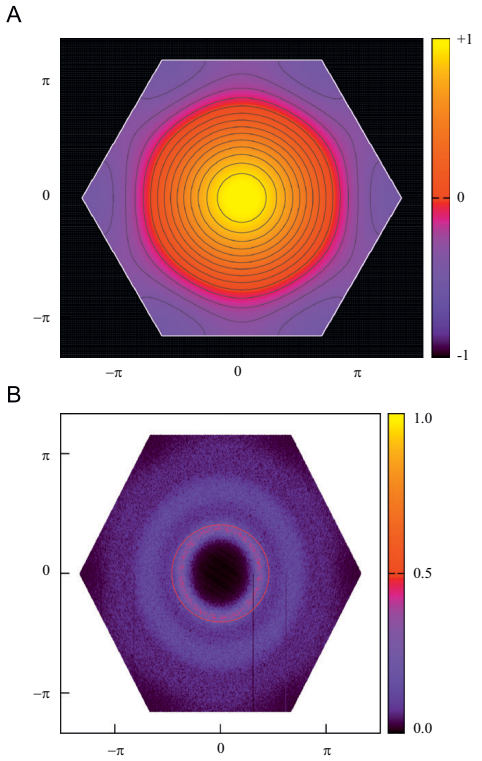

Fig. 3. Analytical prediction of dominating wavenumber. (A) Eq. (29) plotted with contour curves. (B) Numerical Fourier transform of a pattern generated using the parameter values from Table 1 on a lattice of size 465 × 536 cells. The red line marks the analytic prediction of the dominating wave vectors. (For interpretation of the references to color in this figure legend, the reader is referred to the web version of this article.)

described by f_{exo} and f_{endo}, respectively. It is trivially seen that only the ratio $f(a_j) = f_{exo}(a_j)/f_{endo}(a_j)$ is important, and the conclusion is that the model has the same behavior if endocytosis is reduced as if exocytosis is increased from a signal originating from auxin in the neighboring cell.

3.1.3. Constraint on the feedback and efflux capability

An important question is what kind of feedback functions can generate patterns. Since the feedback mechanism in plants is unknown it is important to know what the requirements are for phyllotaxis; also if the model is to be used for other biological systems these constraints on the feedback are of interest. Unexpectedly, the analysis shows that the requirement on the feedback is tightly connected to the mechanism for active efflux transport. Neglecting degradation of auxin (i.e. $\delta_a = 0$), a positive value for the parameter D with an unstable homogeneous fixed point (such that patterns are generated) is possible if and only if

$$\frac{f'(a)}{f(a)} \Big/ \frac{h'(a)}{h(a)} > \frac{mf(a)+1}{2mf(a)+1} \tag{30}$$

is fulfilled, which can be found by substituting Eq. (16) into Eq. (28). If this requirement is not fulfilled no physically meaningful parameter values can be found that yield patterns. The right-hand side of Eq. (30) is bounded by $\frac{1}{2}$ and 1.

As an illustrative example, consider a feedback function of the form $f(a) \propto a^{\alpha}$ (α measures the 'strength' or cooperativity of the feedback signal) with a linear efflux function ($h(a) \propto a$). Then the left-hand side of Eq. (30) is equal to α. Thus such a feedback function can be used for polarization in a pattern generating model only if $\alpha > \frac{1}{2}$.

The tight relation between the feedback and the efflux transport shown in Eq. (30) is quite interesting. If the efflux is assumed to be saturable and described by a Michaelis–Menten function, h'/h is equal to $K/(a(K+a))$ which is less or equal to $1/a$ corresponding to a linear h. Compared with linear efflux transport, the saturable efflux described by a Michaelis–Menten function increases the possibility for pattern generation.

To further investigate the inequalities in Eqs. (27) and (28), we performed a number of simulations using different parameter sets to generate numerical statistics for pattern generation and compare with the analytical prediction of boundaries. Following previous efforts, we used the functions from Eq. (26) to describe feedback and saturable efflux. The results from these simulations

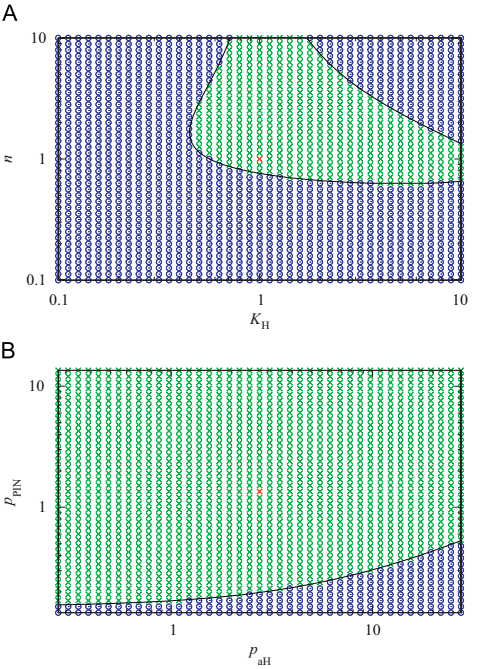

Fig. 4. Two parameters are changed within two orders of magnitude around the set of parameters given by Table 1. Green crosses/blue circles mark simulations that resulted in an unstable/stable homogeneous fixed point. The red cross indicates the parameter values in Table 1. The line marks the boundary given by Eqs. (27) and (28). (A) Parameters K_H and n are changed. (B) Parameters p_{aH} and p_{PIN} are changed. (For interpretation of the references to color in this figure legend, the reader is referred to the web version of this article.)

are presented in Fig. 4. As expected, the numerical simulations follow the analytical prediction very well.

3.1.4. Auxin-induced production of transport mediators influences the patterning capability

It has previously been shown that auxin-induced PIN1 and AUX1 production has an effect on the stability of the formed patterns (Heisler and Jönsson, 2006; Merks et al., 2007). While auxin-induced PIN1 destabilizes the inhomogeneous patterns by inducing a translation of the peaks, auxin-induced AUX1 acts oppositely and can stabilize the instabilities caused by auxin-induced PIN1. Here, we investigate how patterning capability (i.e. the instability of the homogeneous fixed point) depends on auxin-induced production of PIN1 and AUX1.

Assume the total PIN1 concentration in a cell P_{total} to be an increasing function of the auxin concentration. From Eqs. (12) and (13) we can write the product between the total concentration of PIN1 and the efflux transport function as $\hat{h}(a) = P_{\text{total}}P(a)h(a)$ where P_{total} is now a reference concentration and $P(a)$ is a dimensionless increasing function. In Eq. (30), $h'(a)/h(a)$ is replaced by

$$\frac{\hat{h}'(a)}{\hat{h}(a)} = \frac{P'(a)}{P(a)} + \frac{h'(a)}{h(a)} \geqslant \frac{h'(a)}{h(a)}, \tag{31}$$

and we can see that auxin-induced PIN1 production stabilizes the homogeneous fixed point, i.e. it has a negative effect on the patterning capability of the model. A similar investigation for auxin-induced AUX1 leads to $\hat{h}_{\text{A}}(a) = A_{\text{total}}A(a)h_{\text{A}}(a)$ where again $A(a)$ is an increasing function of a. This affects D in Eq. (14) and (15) which is replaced by

$$\hat{D} = D - G\mathscr{A}A_{\text{total}}A'(a)h_{\text{A}} \leqslant D. \tag{32}$$

From Eqs. (27) and (28) it follows that auxin-induced AUX1 destabilizes the homogeneous fixed point, i.e. it has a positive effect on the patterning capability of the model.

3.2. Robustness of the model

After investigating the pattern capability of the model, we now turn to investigate in more detail the characteristics of the patterns. We use the wavelength as a measure and also investigate which types of patterns that result.

Model robustness was first tested by calculating the local sensitivity of each parameter, defined by

$$\text{Sensitivity} = \left|\frac{\partial L}{\partial p}\frac{p}{L}\right|, \tag{33}$$

where p is a parameter and L is the predicted wavelength. L can be derived from Eq. (29). Fig. 5 presents the predicted sensitivities. It can be seen that L was very robust to perturbations of parameters related to production, degradation, and transport rates. On the contrary, the predicted wavelength is more sensitive to parameters used for defining the auxin feedback to PIN1 polarization and the saturation of efflux. Especially, the parameter c_p has a large sensitivity, which might be due to its somewhat unnatural definition as a ratio ($[0:1]$) between symmetric and polarized PIN1 cycling. The parameters k_1 and k_2 represent the actual symmetric and polarized cycling rates and the model is more robust to variations in these parameters.

We further performed a semi-global approach using series of numerical simulations to study the robustness of the final wavelength against parameter perturbations. For each series we kept all parameters except one fixed to the values stated in Table 1. The non-constant parameter was varied two orders of magnitude around the original value. Ten simulations were performed for each unique set of parameter values. We applied a Fourier transform to each resulting pattern and identified the wavenumber with the largest amplitude to estimate the typical wavelength of the pattern. The results are presented in Fig. 6 along with the linear analysis prediction. The average wavelengths extracted from simulations are close to the analytic result, and the parameter dependence of the final pattern follows the results from our sensitivity analysis. The wavelength of the final pattern is more sensitive to the feedback parameters than to other parameters. Note that the auxin degradation (δ_a) restricts the possible wavelengths available to the model by decreasing the parameter region where patterns appear (cf. Eq. (27)).

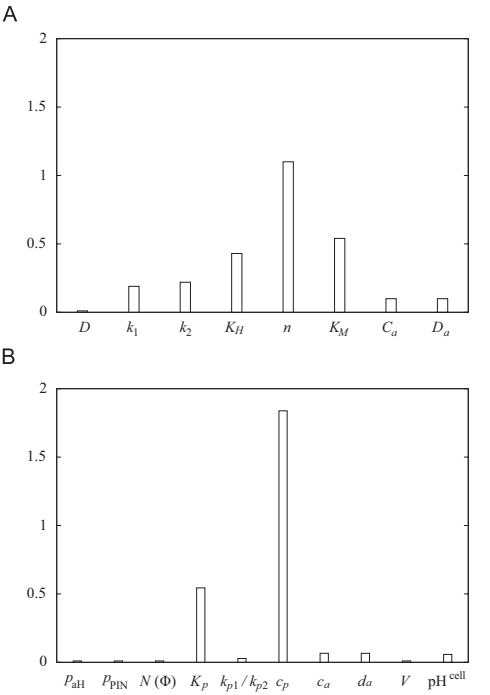

Fig. 5. Sensitivity of predicted wavelength with respect to different parameters. (A) Combined parameters used in the simulations. (B) Original parameters. Parameters p_{AUX}, $f_{\text{aH}}^{\text{cell}}$, $f_{a^-}^{\text{wall}}$, K_{A}, and $k_{\text{A1}}/k_{\text{A2}}$ are integrated out of the equations and have no effect on the predicted wavelength.

From the simulations done for Fig. 6 we noticed that the parameter space is divided into regions of different kinds of resulting patterns. We investigated more closely two regions of interest. Series of simulations for two narrow regions in the parameter space are presented in Fig. 7. The Michaelis–Menten constant for auxin transport K_{M} and the Hill constant for PIN1 cycling K_{H} are varied and we have used visual inspection to identify different types of patterns. The types of patterns are changing from peaks, to peaks and stripes, then to stripes, and finally to reentrant peaks before the homogeneous fixed point becomes stable. This clearly shows that different kinds of patterns can be formed with the regulated transport model, although the parameter space is dominated by patterns with peaks. We have

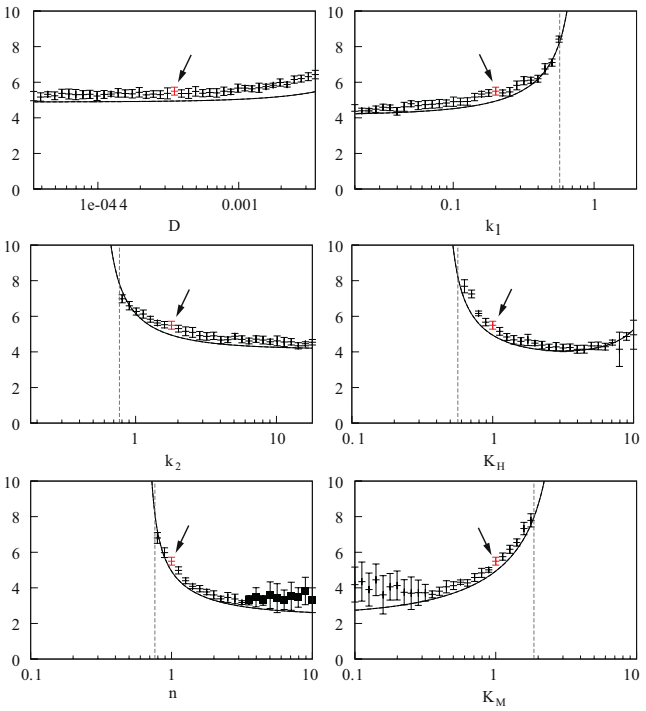

Fig. 6. Estimated wavelengths of generated patterns as functions of different parameters. The parameters D, k_1, k_2, K_H, n, and K_M are changed individually while keeping the other parameters fixed. For each unique set of parameter values 10 numerical simulations were performed, and the average and standard deviation is plotted. The solid black line gives the analytical prediction of the dominating wavelength for the system close to the homogeneous fixed point. Red data points (marked with black arrows) mark simulations with the parameter values from Table 1. Black squares mark data points for whose convergence towards a stable fixed point were extremely slow. Dashed vertical lines show the analytical boundary between regions with stable/unstable homogeneous fixed points. The boundary is given by Eqs. (27) and (28). (For interpretation of the references to color in this figure legend, the reader is referred to the web version of this article.)

not analytically identified requirements for stripe formation, although stripes have only appeared in simulations where the feedback signal is saturated. This can be compared to stripe formation in reaction–diffusion models where the stripes can appear when the self-enhancement is saturated (Meinhardt, 1995).

3.3. Model simplifications suggest parsimony of the model mechanism

3.3.1. Wall feedback is not capable of generating patterns

The proposed model suggests that the feedback from auxin to PIN1 polarization comes from neighboring cells. This means that the signal transmitting the information has to pass through the cell walls (see Supplementary Information in Jönsson et al., 2006 for a suggested mechanism). We also tested a model where the feedback comes from auxin in the walls, only separated by a thin membrane from the cytosol compartment. The analysis of such a model is presented in Appendix B. Although this model can have an unstable homogeneous fixed point, the eigenvalue distribution shows that the resulting patterns have a fixed wavelength of two cells independent of parameter values and hence the model is not suitable as a model for phyllotaxis.

3.3.2. Competition of attracting PIN1 to the membrane is important

Another important requirement for the model to be capable of creating phyllotactic patterns is the competition among intracellular wall membrane compartments for PIN1. This results from the feedback acting on the cycling rates of PIN1 (there is a competition among the membranes for a constant total amount of PIN1). A model where auxin feeds back directly on the membrane PIN1 is described in Appendix C. Although such a model is capable of generating patterns, the linear dependence on $S(\mathbf{k})$ (as in the wall feedback model) only allows for uninteresting patterns with a wavelength of two cells, independent of parameter values. A simulation of a generated pattern can be seen in Fig. 8.

The competition in the original model leads to an interaction with next-neighbor cells and provides a necessary requirement for the model to generate patterns of the desired form. Interestingly, competition is also important for models where auxin fluxes feed back on PIN1 polarization. Here the PIN1 competition is important

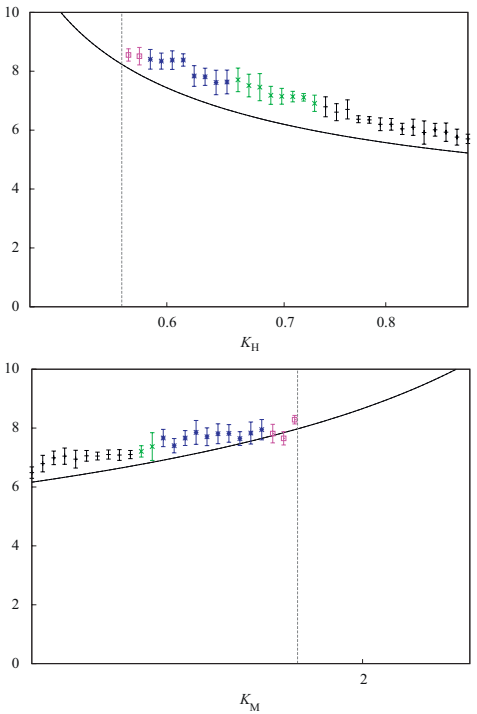

Fig. 7. A similar investigation as for Fig. 6, but for two parameters with regions of special interest. Colors indicate different pattern types: black (+)—peaks, green (×)—peaks and stripes, blue (*) —stripes, magenta (□)—reentrant peaks. (For interpretation of the references to color in this figure legend, the reader is referred to the web version of this article.)

for creating veins with high auxin concentrations (Feugier et al., 2005).

4. Discussion

We have analyzed a model based on a positive feedback on polarized transport as a mechanism capable of generating large-scale patterns from its local interactions. We have shown that the model is capable of generating different spatial patterns such as peaks, stripes and reentrant peaks that have parameter-dependent wavelengths. Our linear analysis together with numerical simulations shows that the analysis is useful for predicting the dynamics, and also the final patterns. We used this to make several predictions.

The analyzed mechanism of pattern generation is inspired from molecular data in plant shoot cells, where it is suggested as a part of the initiation of new primordia. Auxin peaks lead to differentiation of the tissue into organs and the generation of phyllotactic patterns. Although the model predictions of PIN1 polarization patterns and reversal dynamics complies with current experimental data, the proposed signal mediating the feedback from auxin to PIN1 polarization is yet to be identified. We have investigated different possibilities and restrictions for

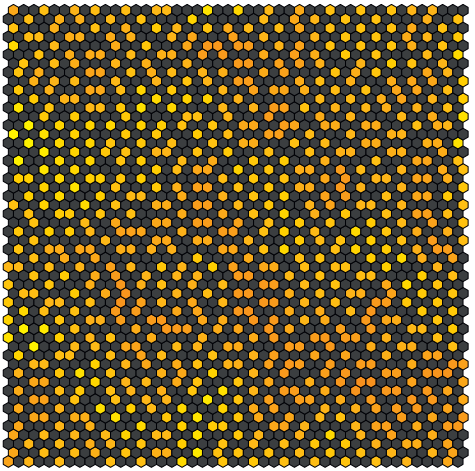

Fig. 8. Simulation of a model without PIN1 competition. The resulting pattern has a wavelength of two. Parameter values used in this simulation are the same as in Table 1 except for the Hill coefficient, where the value $n = 2$ is used for patterns to form.

such a feedback signal. We showed that the feedback works also when acting on PIN1 endocytosis (from membrane to cytosol), which is important since auxin has been shown to affect PIN1 endocytosis (Paciorek et al., 2005).

When analyzing the model using experimental estimates of parameters, we found that the patterns are very robust against parameter perturbations relating to transport rates. This is comforting since the estimates are from different plant species and tissues, but it also makes more plausible the possibility that a plant could introduce the feedback mechanism within an already working environment for auxin transport, without the need of adjusting these parameters with the risk of disrupting other functions where auxin transport is important. The patterns were shown to be more sensitive to parameter perturbations relating to the feedback mechanism, which is a result depending on using parameters from our previous study (Heisler and Jönsson, 2006). Our results suggest how to change these parameter values if higher stability is a main objective (e.g. increasing the Hill-coefficient in the feedback mechanism). This would be at the cost of a possibility to tune the wavelength of the patterns, as well as reaching diverse patterns.

To further investigate the constraints on the feedback mechanism, we introduced a general functional form describing the mechanism. This permitted us to identify feedback mechanisms that allow for the emergence of patterns from a homogeneous state. Our conclusion is that the feedback has to be sensitive enough to differences in neighboring auxin concentrations. Given that we could show that a sub-linear feedback is sensitive enough, this allows for a large variety of possible biological mechanisms. Interestingly, the constraint on the feedback mechanism is tightly coupled with the PIN1-dependent transport mechanism. This provides an example showing the importance of modeling biological mechanisms correctly. For example, the choice between a linear and a saturated transport may render fundamentally different results.

Our analysis also gives predictions for the dependence on the transport mediators PIN1 and AUX1. In agreement with experi-

ments, PIN1 is crucial for the patterning to appear, and lowering the amount of PIN1 about 10-fold from our estimated value would lead to a parameter region where the homogeneous fixed point is stable. Interestingly, AUX1 does not appear in our requirements for generating patterns in our model. This is in agreement with experiments (Bainbridge et al., 2008), where upon removing AUX/LAX proteins primordia were still initiated although the pattern was less stable (as discussed below). In the model case, this is due to the completely symmetric distribution of AUX1 at different membranes for a cell, but the fact that we have disregarded apoplastic diffusion may also be of importance. When introducing auxin-induced production of the transport mediators, the analysis showed that with induced PIN1 periodic patterns occurred over a reduced parameter range, while the parameter region was increased when inducing AUX1. Together with our previous results (Heisler and Jönsson, 2006) this suggests that auxin-induced PIN1 acts to stabilize the homogeneous fixed point while destabilizing the non-homogeneous pattern. Auxin-induced AUX1 acts in the opposite direction, and the loss of pattern stability upon removing AUX1/LAX has also been seen in experiments (Bainbridge et al., 2008).

The presented model is not the most parsimonious way to create a feedback from auxin to PIN1 localization in the membranes. We have investigated several simplifications of the model. We presented results showing a model where auxin in the wall feeds back to PIN1 polarization, and a model where auxin feeds back directly to the PIN1 in the membrane without competition of PIN1 within a cell, and both fail to generate desired patterns. Although proving that a simpler mechanism for regulated transport to be able to generate patterns is intractable, our analysis indicate that the proposed model includes the necessary features of a pattern generating model. All our attempts to simplify the model further have led to the loss of interaction from auxin in the next-neighboring cells, which is a requirement for the model to generate non-trivial patterns.

Finally, we have shown that the model is also able to generate other types of patterns than peaks. Stripes and reentrant peaks can also appear, which may have implications in other biological systems. A peak pattern seems to be natural for the proposed mechanism, and other patterns can be created in rather narrow parameter regions in-between the peaked pattern and no pattern regions. An interesting note is that this seems to be similar to flux-based models used for venation, where the venation patterns appear in a parameter region in-between a no-pattern region and a 'patch'-like pattern (Fujita and Mochizuki, 2006).

Two mechanisms have been suggested for patterning in plants where auxin feeds back to PIN polarization. As discussed before, a flux-based mechanism has been suggested mainly for canalization and vein formation, while the concentration-based model analyzed here has been proposed for phyllotaxis. Whether PIN polarization is tissue-specific is still an open question, but recent work has investigated the possibility of a unified description (Merks et al., 2007; Stoma et al., 2008).

The concentration-based model can be considered as a novel mechanism for spontaneous pattern generation in biology, and complements suggested mechanisms used in reaction–diffusion models. Its capabilities are very similar to those of reaction–diffusion models, but as it 'replaces' the need of intracellular nonlinear reactions and diffusion with a regulated active transport we do not regard it as a reaction–diffusion model. The regulated transport mechanism can be realized using a few elementary biochemical processes and hence provides a plausible mechanism for pattern formation in biology. Especially, the molecular data of phyllotaxis indicate the presence of this mechanism. Another system where moving uphill in concentration is present is chemotaxis, where e.g. bacteria move against a signal gradient and form patterns, which has been investigated in mathematical models (e.g. Keller and Segel, 1970).

The usefulness of the analyzed model will be determined by the actual use in biology, but our analysis provides distinct predictions for which biological mechanisms to search for within a given system and which requirements that need to be fulfilled in the system. This hopefully introduces some new perspectives in the field of developmental modeling.

Acknowledgments

We thank Vijay Chickarmane, Marcus Heisler, Pawel Krupinski, Pontus Melke, Elliot Meyerowitz and Eric Mjolsness for helpful discussions, and P.K. and P.M. for comments on the manuscript. This work was in part supported by the Swedish Research Council, Human Frontier Science Program, and the Royal Physiographic Society in Lund.

Appendix A. Stability analysis of model with cell compartments

The analysis is performed by means of a linearization around the homogeneous fixed point. The cells are assumed to be located on a regular lattice and all cells are assumed to have m neighbors (an even number). To analyze the stability of the homogeneous fixed point we consider a small perturbation $a_i = a + \varepsilon_i$ and neglect all terms of second order or higher. Eqs. (8) and (25) then turn into a system of ordinary linear equations

$$\frac{d\varepsilon_i}{d\tau} = \frac{1}{2}(D + E_1 - E_2 - mE_3) \sum_{k\in\mathcal{N}_i} (\varepsilon_k - \varepsilon_i) - \frac{1}{2}E_3 \sum_{k\in\mathcal{N}_i} \left(\sum_{l\in\mathcal{N}_k} \varepsilon_l - \sum_{l\in\mathcal{N}_i} \varepsilon_l \right) - \delta_a \varepsilon_i, \tag{A.1}$$

where E_1, E_2, and E_3 are defined in Eq. (16). In Fourier space Eq. (A.1) is diagonalized and corresponds to

$$\dot{\varepsilon}_{\mathbf{k}} = \left[\frac{m}{2}(D + E_1 - E_2 - mE_3)(S(\mathbf{k}) - 1) - \frac{m^2}{2}E_3 S(\mathbf{k})(S(\mathbf{k}) - 1) - \delta_a \right] \varepsilon_{\mathbf{k}} = \lambda_{\mathbf{k}} \varepsilon_{\mathbf{k}}, \tag{A.2}$$

where $S(\mathbf{k})$ is defined in Eq. (21). If at least one eigenvalue $\lambda_{\mathbf{k}}$ of the system is positive, then the homogeneous fixed point is unstable and we expect patterns to emerge. The set of wave vectors that corresponds to the maximal (typically degenerate) eigenvalue is

$$\Omega = \left\{ \mathbf{k} | S(\mathbf{k}) = S^* = \frac{D + E_1 - E_2}{2mE_3} \right\}. \tag{A.3}$$

For the perturbation of auxin concentrations in cell compartments the final solution to the linearized differential equation is analogous to Eq. (24), but with a single eigenvalue for each wave-vector $\mathbf{k}$. The requirements for a non-trivial positive eigenvalue are the same as given in Eqs. (27) and (28).

Appendix B. Stability analysis of model with feedback from neighboring wall compartments

With feedback from the wall compartments the full model with cell and wall compartments can be expressed as in Eq. (3) with the exception that

$$P^*_{ij} = \mathscr{P}_{ij} W^{-1}_{ij} P_{\text{total}} \quad \text{where } \mathscr{P}_{ij} = \frac{f(a_{ij})}{1 + \sum_{k\in\mathcal{N}_i} f(a_{ik})}$$

and

$$f(a_{ij}) = \frac{f_{\text{exo}}(a_{ij})}{f_{\text{endo}}(a_{ij})}. \tag{B.1}$$

The linearized system of ordinary differential equations is

$$\frac{d\varepsilon_i}{d\tau} = -\left(\delta_a + \sum_{k\in\mathcal{N}_i}(d_1+E_1)\right)\varepsilon_i + (D_2-E_2)\sum_{k\in\mathcal{N}_i}\varepsilon_{ik}, \tag{B.2}$$

$$\frac{d\varepsilon_{ij}}{d\tau} = (D+E_1)(\varepsilon_i+\varepsilon_j) - E_3\left(\sum_{l\in\mathcal{N}_i}\varepsilon_{il} + \sum_{l\in\mathcal{N}_j}\varepsilon_{jl}\right) + 2(-D_2+E_2+mE_3)\varepsilon_{ij}. \tag{B.3}$$

In Fourier space the system of equations is equivalent to

$$\dot{\varepsilon}_{\mathbf{k}} = -(D_A + m(D+E_1))\varepsilon_{\mathbf{k}} + 2(D_2-E_2)\sum_{p=1}^{m/2}\cos\left(\frac{1}{2}\mathbf{k}\cdot\mathbf{e}_p\right)\varepsilon_{\mathbf{k},p} \tag{B.4}$$

$$\dot{\varepsilon}_{\mathbf{k},p} = 2(D+E_1)\cos\left(\frac{1}{2}\mathbf{k}\cdot\mathbf{e}_p\right)\varepsilon_{\mathbf{k}} - 4E_3\cos\left(\frac{1}{2}\mathbf{k}\cdot\mathbf{e}_p\right)\sum_{q=1}^{m/2}\cos\left(\frac{1}{2}\mathbf{k}\cdot\mathbf{e}_q\right)\varepsilon_{\mathbf{k},q} - 2(D_2-E_2-mE_3)\varepsilon_{\mathbf{k},p}. \tag{B.5}$$

With the definition of $\sigma_{\mathbf{k}}$ in Eq. (22), Eqs. (B.4) and (B.5) can be expressed as

$$\begin{bmatrix}\dot{\varepsilon}_{\mathbf{k}}\\ \dot{\sigma}_{\mathbf{k}}\end{bmatrix} = \begin{bmatrix}-(\delta_a + m(D+E_1)) & m(D_2-E_2)\\ (S(\mathbf{k})+1)(D+E_1) & -2(D_2-E_2+E_3S(\mathbf{k}))\end{bmatrix}\begin{bmatrix}\varepsilon_{\mathbf{k}}\\ \sigma_{\mathbf{k}}\end{bmatrix}. \tag{B.6}$$

The characteristic equation for the matrix in the RHS of Eq. (B.6) can only yield trivial positive eigenvalues as the coefficients in the quadratic equation are linear in $S(\mathbf{k})$.

Appendix C. Analysis of a model without PIN1 competition

A model where auxin feeds back directly on PIN1 in the membrane can be described by

$$\frac{dP_{ij}}{dt} = f_+(a_j) - f_-(a_j)P_{ij}, \tag{C.1}$$

and represents a model without competition. The simplified auxin transport model is again described by Eqs. (12) and (13) with

$$\mathscr{P}_{ij}P_{\text{total}} = W_{ij}P^*_{ij} = Wf_{\text{p}}(a_j) \quad \text{where } f_{\text{p}}(a_j) = \frac{f_+(a_j)}{f_-(a_j)}. \tag{C.2}$$

The linearized system of ordinary differential equations is

$$\frac{d\varepsilon_i}{d\tau} = -(\delta_a + m(D+C_1))\varepsilon_i - C_2\sum_{k\in\mathcal{N}_i}\varepsilon_k + D_2\sum_{k\in\mathcal{N}_i}\varepsilon_{ik}, \tag{C.3}$$

$$\frac{d\varepsilon_{ij}}{d\tau} = (D+C_1+C_2)(\varepsilon_i+\varepsilon_j) - 2D_2\varepsilon_{ij}, \tag{C.4}$$

where $C_1 = Wf'_{\text{p}}h$ and $C_2 = Wf_{\text{p}}h'$.

In Fourier space Eqs. (C.3) and (C.4) are equivalent to

$$\dot{\varepsilon}_{\mathbf{k}} = -(\delta_a + m(D+C_1+C_2S(\mathbf{k})))\varepsilon_{\mathbf{k}} + 2D_2\sum_{p=1}^{m/2}\cos\left(\frac{1}{2}\mathbf{k}\cdot\mathbf{e}_p\right)\varepsilon_{\mathbf{k},p}, \tag{C.5}$$

$$\dot{\varepsilon}_{\mathbf{k},p} = 2(D+C_1+C_2)\cos\left(\frac{1}{2}\mathbf{k}\cdot\mathbf{e}_p\right)\varepsilon_{\mathbf{k}} - 2D_2\varepsilon_{\mathbf{k},p}. \tag{C.6}$$

Using the definition of $\sigma_{\mathbf{k}}$ in Eq. (22), Eqs. (C.5) and (C.6) can be expressed as

$$\begin{bmatrix}\dot{\varepsilon}_{\mathbf{k}}\\ \dot{\sigma}_{\mathbf{k}}\end{bmatrix} = \begin{bmatrix}-(\delta_a + m(D+C_1+C_2S(\mathbf{k}))) & mD_2\\ (D+C_1+C_2)(1+S(\mathbf{k})) & -2D_2\end{bmatrix}\begin{bmatrix}\varepsilon_{\mathbf{k}}\\ \sigma_{\mathbf{k}}\end{bmatrix}. \tag{C.7}$$

The characteristic equation for the matrix in Eq. (C.7) can only yield trivial positive eigenvalues as the coefficients in the quadratic equation are linear in $S(\mathbf{k})$.

References

Adler, I., Jean, R.V., Barabé, D., 1997. A history of the study of phyllotaxis. Ann. Bot. 80, 231–244.

Bainbridge, K., Guyomarch, S., Bayer, E., Swarup, R., Bennett, M., Mandel, T., Kuhlemeier, C., 2008. Auxin influx carriers stabilize phyllotactic patterning. Genes Dev. 22, 810–823.

Barbier de Reuille, P., Bohn-Courseau, I., Ljung, K., Morin, H., Carraro, N., Sandberg, G., Godin, C., Traas, J., 2006. Computer simulations reveal novel properties of the cell–cell signaling network at the shoot apex in Arabidopsis. Proc. Natl. Acad. Sci. USA 103, 1627–1632.

Benkova, E., Michniewicz, M., Sauer, M., Teichmann, T., Seifertova, D., Jürgens, G., Friml, J., 2003. Cell 115, 591–602.

Chapman, J.M., Perry, R., 1987. A diffusion model of phyllotaxis. Ann. Bot. London 60, 377–389.

Douady, S., Couder, Y., 1992. Phyllotaxis as a physical self-organized growth process. Phys. Rev. Lett. 68, 2098–2101.

Feugier, F.G., Mochizuki, A., Iwasa, Y., 2005. Self-organization of the vascular system in plant leaves: inter-dependent dynamics of auxin flux and carrier proteins. J. Theor. Biol. 236, 366–375.

Fujita, H., Mochizuki, A., 2006. Pattern formation of leaf veins by the positive feedback regulation between auxin flow and auxin efflux carrier. J. Theor. Biol. 241, 541–551.

Geldner, N., Friml, J., Stierhof, Y.D., Jürgens, G., Palme, K., 2001. PIN and AUX/LAX proteins: their role in auxin accumulation. Nature 413, 425–428.

Gierer, A., Meinhardt, H., 1972. A theory of biological pattern formation. Kybernetik 12, 30–39.

Green, P., Steele, C.S., Rennich, S.C., 1998. How plants produce patterns. A review and a proposal that undulating field behavior is the mechanism. In: Jean, R.V., Barabé, D. (Eds.), Symmetry in Plants. World Scientific, Singapore, pp. 359–392.

Heisler, M., Ohno, C., Das, P., Sieber, P., Long, J.A., Reddy, G.V., Meyerowitz, E.M., 2005. Patterns of auxin transport and gene expression during primordium development revealed by live imaging of the Arabidopsis inflorescence meristem. Curr. Biol. 15, 1899–1911.

Heisler, M.G., Jönsson, H., 2006. Modeling auxin transport and plant development. J. Plant Growth Regul. 25, 302–312.

Jean, R.V., Barabé, D, 1998. Symmetry in Plants. World Scientific, Singapore.

Jönsson, H., Heisler, M., Shapiro, B.E., Meyerowitz, E.M., Mjolsness, E., 2006. Proc. Natl. Acad. Sci. USA 103, 1633–1638.

Keller, E.F., Segel, L.A., 1970. Initiation of slime mold aggregation viewed as an instability. J. Theor. Biol. 26, 399–415.

Kramer, E.M., 2004. PIN and AUX/LAX proteins: their role in auxin accumulation. Trends Plant Sci. 9, 578–582.

Kramer, E.M., 2006. How far can a molecule of weak acid travel in the apoplast or xylem? Plant Physiol. 141, 1233–1236.

Meinhardt, H., 1982. Models of Biological Pattern Formation. Academic Press, London.

Meinhardt, H., 1995. Growth and patterning—dynamics of stripe formation. Nature 376, 722–723.

Merks, R.M., Van de Peer, Y., Inzé, D., Beemster, G.T., 2007. Canalization without flux sensors: a traveling-wave hypothesis. Trends Plant Sci. 12, 384–390.

Mitchison, G.J., 1977. Phyllotaxis and the Fibonacci series. Science 196, 270–275.

Mitchison, G.J., 1980. A model for vein formation in higher plants. Proc. R. Soc. London B 207, 79–109.

Newell, A.C., Shipman, P.D., Sun, Z., 2007. Phyllotaxis: cooperation and competition between mechanical and biochemical processes. J. Theor. Biol. 251, 421–439.

Okada, K., Ueda, J., Komaki, M.K., Bell, C.J., Shimura, Y., 1991. Requirement of the auxin polar transport system in early stages of Arabidopsis floral bud formation. Plant Cell 3, 677–684.

Paciorek, T., Zazímalová, E., Ruthardt, N., Petrásek, J., Stierhof, Y.D., Kleine-Vehn, J., Morris, D.A., Emans, N., Jürgens, G., Geldner, N., Friml, J., 2005. Auxin inhibits endocytosis and promotes its own efflux from cells. Nature 435, 1251–1256.

Press, W.H., Teukolsky, S.A., Vetterling, W.T., Flannery, B.P., 1992. Numerical Recipes in C The Art of Scientific Computing. Cambridge University Press, New York.

Raven, J.A., 1975. Transport of indoleacetic-acid in plant-cells in relation to pH and electrical potential gradients, and its significance for polar IAA transport. New Phytol. 74, 163–172.

Reinhardt, D., Mandel, T., Kuhlemeier, C., 2000. Auxin regulates the initiation and radial position of plant lateral organs. Plant Cell 12, 507–518.

Reinhardt, D., Pesce, E.R., Stieger, P., Mandel, T., Baltensperger, K., Bennett, M., Traas, J., Friml, J., Kuhlemeier, C., 2003. Regulation of phyllotaxis by polar auxin transport. Nature 426, 255–260.

Rubery, P.H., Sheldrake, A.R., 1974. Carrier-mediated auxin transport. Planta 118, 101–121.

Sachs, T., 1981. The control of the patterned differentiation of vascular tissues. Adv. Bot. Res. 9, 151–162.

Shipman, P.D., Newell, A.C., 2005. Polygonal planforms and phyllotaxis on plants. J. Theor. Biol. 236, 154–197.

Smith, R.S., Kuhlemeier, C., Prusinkiewicz, P., 2006a. Inhibition fields for phyllotactic pattern formation: a simulation study. Can. J. Bot. 84, 1635–1649.

Smith, R.S., Guyomarc'h, S., Mandel, T., Reinhardt, D., Kuhlemeier, C., Prusinkiewicz, P., 2006b. A plausible model for phyllotaxis. Proc. Natl. Acad. Sci. USA 103, 1301–1306.

Stoma, S., Lucas, M., Chopard, J., Schaedel, M., Traas, J., Godin, C., 2008. Flux-based transport enhancement as a plausible unifying mechanism for auxin transport in meristem development. PLoS Comput. Biol. 4, e1000207.

Swarup, R., Kramer, E.M., Perry, P., Knox, K., Leyser, H.M., Haseloff, J., Beemster, G.T., Bhalerao, R., Bennett, M.J., 2005. Root gravitropism requires lateral root cap and epidermal cells for transport and response to a mobile auxin signal. Nat. Cell Biol. 7, 1057–1065.

Turing, A.M., 1952. The chemical basis for morphogenesis. Philos. Trans. R. Soc. London B 237, 37–72.

LUND UNIVERSITY

ISBN: 978-91-628-8063-7
Printed by ***MEDIA-TRYCK***, Sweden 2010